WARLLEY HUDSON CAMPOS

TIGHT-BINDING ANALYSIS OF TOPOLOGICAL MATERIALS AND NEW DIRECTIONS IN OPTICAL TWEEZERS

Thesis submitted to the Universidade Federal de Viçosa in fulfillment of the requirements of the Graduate Program in Physics for obtainment of the degree of *Doctor Scientiae*.

Adviser: Winder Alexander de Moura Melo

Co-advisers: Jakson Miranda Fonseca
Joaquim Bonfim Santos Mendes
Afranio Rodrigues Pereira

VIÇOSA - MINAS GERAIS
2021

Ficha catalográfica elaborada pela Biblioteca Central da Universidade Federal de Viçosa - Campus Viçosa

T
C198t
2021

Campos, Warlley Hudson, 1992-
Tight-binding analysis of topological materials and new directions in optical tweezers / Warlley Hudson Campos. – Viçosa, MG, 2021.
162 f. : il. (algumas color.) ; 29 cm.

Inclui apêndices.
Orientador: Winder Alexander de Moura Melo.
Tese (doutorado) - Universidade Federal de Viçosa.
Referências bibliográficas: f. 148-162.

1. Semicondutores. 2. Pinças ópticas. 3. Isolantes topológicos. I. Universidade Federal de Viçosa. Departamento de Física. Programa de Pós-Graduação em Física Aplicada. II. Título.

CDD 22. ed. 537.622

WARLLEY HUDSON CAMPOS

TIGHT-BINDING ANALYSIS OF TOPOLOGICAL MATERIALS AND NEW DIRECTIONS IN OPTICAL TWEEZERS

Thesis submitted to the Universidade Federal de Viçosa in fulfillment of the requirements of the Graduate Program in Physics for obtainment of the degree of *Doctor Scientiae*.

APPROVED: January 27, 2021.

Assent:

Warlley Hudson Campos
Author

Winder Alexander de Moura Melo
Adviser

To all those who supported me ...

at any moment. Simply...

because they wanted to.

Acknowledgments

I will never be able to express how grateful I am to...

Bruna Rodrigues for all those years of an amazing relationship, from whom I have learned so much to become a better person. For being always there, supporting me in both my life and career.

Libor Šmejkal, Yuri Estevão and João Paulo de Almeida for helping me so much with my personal development. I owe a lot of who I am today to all of you.

Rodolfo Gontijo and Diego de Freitas, friends of a lifetime, for all the challenges we have helped each other to overcome and for all the wisdom we have acquired on our discussions about life.

Davi Rodrigues, V.K. Bharadwaj and Aileen Schütz for helping me so much with my adaptation in Germany, supporting me with work, learning and everyday life.

My father Vantuir Campos, for always being so helpful, no matter what.

My mother Amélia Campos, for always being so worried with my well-being and for always being so happy whenever I achieved one of my goals.

My brother Wallyson Campos, for being a great friend and for all the challenges we have been facing together.

My grandmother Nair Alexandrina, for being the kindest person in the world to me.

Winder Moura-Melo, for advising me over so many years, during my undergraduate, master and PhD studies, and for being always helpful when I needed.

Joaquim Mendes, for being so important to my professional development, to my career planing and for opening my eyes to the Physics community outside our department.

Márcio Rocha, for all the support during my PhD. Your professionalism is definitely an inspiration for all the students who had the honor to work with you.

Jakson Fonseca, for all the discussions about physics and for all the effort you have always put into helping me.

Jairo Sinova and Karin Everschor-Sitte, for the opportunity to work with their teams in Germany. I had never learned so much and met so many amazing people in such a short period of time.

Johannes Gutenberg Universität (JGU) and the staff, for all the support I have received from the during my stay abroad.

UFV and all the staff, for working constantly to provide all the support that is extremely important for the students.

CNPq, for the undergraduate research scholarship during my undergraduate studies and CAPES, for financing both my Masters and PhD research activities.

Overall, I am extremely grateful to everything and everyone that life has presented to me, especially the most difficult challenges, because they were exactly what ignited my will and my determination. I am definitely ready and excited for the forthcoming ones.

This study was financed in part by the Coordenação de Aperfeiçoamento de Pessoal de Nível Superior – Brazil (CAPES) – Finance Code 001.

"A man who dares to waste one hour of time
has not discovered the value of life."

Charles Darwin

Abstract

CAMPOS, Warlley Hudson, D.Sc., Universidade Federal de Viçosa, January, 2021. **Tight-binding analysis of topological materials and new directions in optical tweezers**. Adviser: Winder Alexander de Moura Melo. Co-Advisers: Jakson Miranda Fonseca, Joaquim Bonfim Santos Mendes and Afranio Rodrigues Pereira.

Optical tweezers (OT) is a powerful technique to manipulate microscopic objects using light. Dielectric particles are stably trapped, while metallic beads are usually deflected by radiometric forces. The optical trapping of semi-transparent particles have been overlooked in the literature. In this regard, we have observed that Bi_2Te_3, Bi_2Se_3 [both are topological insulators (TI's)] and germanium particles behave like optically induced oscillators under a Gaussian laser beam OT. The oscillations take place in a plane perpendicular to the optical axis of the laser beam as a result of the competition between gradient and radiometric forces. Remarkably, the oscillation direction of the germanium particles depends on the polarization of the laser beam. We propose an effective model to describe these effects, which reproduces the experimental data with good accuracy. Furthermore, we propose a generalization of the Ashkin's model for OT in the geometrical optics regime, accounting for light absorption by the trapped particle. We have also studied the interplay between topological materials and magnetic ordering. These materials exhibit very unusual properties, such as metallic surface states with "spin-momentum locking" in TI's and corner-localized states in second order TI's. Here, we show that an electrically charged wire near a semi-cylindrical cavity in a TI can be used to induce a Hall current reversion on its surface. Furthermore, preliminary investigations have indicated higher order topology on spinful ferromagnetic and antiferromagnetic variations of the 2D SSH model. Similar analysis have shown that an effect analogous to the topological metal-insulator transition for antiferromagnetic CuMnAs takes place in its ferromagnetic variation. Among the possible applications of our results, stand out the optical rheology of soft matter interfaces, dynamical force measurements in macromolecules, colloid science and biopolymers, as well as a possible experimental realization of a microscopic single-particle thermal machine. In turn, topological materials are quoted as promising candidates for near future technology, with possibilities for applications in spintronics, quantum computation and advanced low-dissipation devices.

Keywords: Topological Materials. Optical Tweezers. Semiconductors. Topological Insulators.

Resumo

CAMPOS, Warlley Hudson, D.Sc., Universidade Federal de Viçosa, janeiro de 2021. **Análise em tight-binding de materiais topológicos e novas direções em pinças ópticas**. Orientador: Winder Alexander de Moura Melo. Coorientadores: Jakson Miranda Fonseca, Joaquim Bonfim Santos Mendes e Afranio Rodrigues Pereira.

A pinça óptica (PO) é uma técnica poderosa para manipular objetos microscópicos usando luz. Partículas dielétricas são aprisionadas de forma estável, enquanto que partículas metálicas geralmente são repelidas por forças radiométricas. O aprisionamento óptico de partículas semitransparentes tem sido negligenciado na literatura. Nesse sentido, observamos que partículas de Bi_2Te_3, Bi_2Se_3 [ambos são isolantes topológicos (IT's)] e germânio se comportam como osciladores induzidos opticamente sob uma PO de feixe de laser gaussiano. As oscilações ocorrem num plano perpendicular ao eixo óptico do laser como resultado da competição entre forças gradientes e radiométricas. Notavelmente, a direção de oscilação das partículas de germânio depende da polarização do laser. Nós propomos um modelo efetivo descrevendo esses efeitos, que reproduz os dados experimentais com boa precisão. Além disso, propomos uma generalização do modelo de Ashkin para PO's no regime de óptica geométrica, contabilizando a absorção de luz pela partícula aprisionada. Nós também estudamos a combinação de materiais topológicos com ordenamento magnético. Esses materiais exibem propriedades muito incomuns, como estados metálicos de superfície com "spin-momentum locking" em IT's e estados localizados em cantos nos IT's de segunda ordem. Aqui, mostramos que um fio eletricamente carregado perto de uma cavidade semicilíndrica de um IT pode ser usado para induzir uma reversão da corrente Hall na sua superfície. Além disso, investigações preliminares indicaram topologia de ordem superior em variações ferromagnéticas e antiferromagnéticas do modelo SSH em 2D. Análises semelhantes mostraram que um efeito análogo à transição topológica metal-isolante no CuMnAs antiferromagnético acontece na sua variação ferromagnética. Entre as possíveis aplicações dos nossos resultados, se destacam a reologia óptica de interfaces de matéria mole, medidas dinâmicas de força em macromoléculas, ciência de colóides e biopolímeros, bem como uma possível realização experimental de uma máquina térmica microscópica de partícula única. Por sua vez, materiais topológicos são citados como candidatos promissores para tecnologia em um futuro próximo, com possibilidades de aplicações em spintrônica, computação quântica e dispositivos avançados de baixa dissipação.

Palavras-chave: Materiais Topológicos. Pinças Ópticas. Semicondutores. Isolantes Topológicos.

Summary

1 Introduction **12**

1.1 Optical tweezers . . . 14

1.1.1 Geometrical optics regime . . . 17

1.1.2 The Rayleigh regime . . . 22

1.1.3 Mie regime . . . 23

1.1.4 Metallic particles in OT . . . 25

1.1.5 Absorption of light by the particle . . . 27

1.1.6 The Stokes force and the Brownian motion . . . 28

1.2 Topological matter . . . 29

1.2.1 The quantum Hall effect and the TKNN invariant . . . 30

1.2.2 Topological insulators . . . 33

1.2.3 Topological crystalline insulators . . . 44

1.2.4 Higher order topological insulators . . . 47

1.2.5 Topological antiferromagnetic spintronics . . . 51

PART I **57**

2 Topological insulator particles as optically induced oscillators **58**

2.1 Objectives . . . 60

2.2 Materials and methods . . . 60

2.2.1 Experimental setup . . . 61

2.2.2 Experimental procedure used to obtain the forces . . . 61

2.2.3 Preparation of the samples . . . 63

2.2.4 Characterization of the Bi_2Te_3 and Bi_2Se_3 crystals . . . 64

2.3 Results and discussion . . . 65

2.3.1 Effective model . . . 66

2.3.2 Experimental results and comparison with theoretical model . . . 68

2.4 Conclusions . . . 73

3 Extending the Ashkin's model to light-absorbing particles 75

3.1 Objectives . . . 76

3.2 Methods . . . 77

3.3 The model: spherical absorbing particle . . . 77

3.4 Results and Discussion . . . 80

3.5 Conclusions . . . 87

Appendix A . . . 88

Appendix B . . . 89

4 Germanium microparticles as optically induced oscillators 93

4.1 Objectives . . . 95

4.2 Materials and methods . . . 96

4.2.1 Synthesis and characterization of the Ge microparticles . . . 96

4.2.2 Optical tweezers setup . . . 97

4.2.3 Experimental procedures and data analysis to obtain the forces . . . 97

4.3 Results and discussions . . . 99

4.3.1 Theoretical model . . . 99

4.3.2 Comparison between theory and experiments . . . 102

4.3.3 Single particle thermal machine . . . 106

4.4 Conclusions . . . 107

PART II 109

5 Geometrically induced reversion of Hall current in a topological insulator cavity 110

5.1 The semispherical geometry and the monopole reversion . . . 112

5.2 Magnetic monopole picture . . . 116

5.3 Conclusions and Prospects . . . 119

6 Higher order topology analysis of electronic band structures in (anti) ferromagnetic systems 122

6.1 Objectives . . . 123

6.2 Methods . . . 123

6.3 Spinful quantized electric quadrupole moment in the (anti)ferromagnetic 2D SSH model 126
6.4 Tetragonal Copper Manganese Arsenide (CuMnAs) 135
6.5 Conclusions and prospects 141

7 Final conclusions and prospects **144**

References **148**

Chapter 1

Introduction

In this thesis we present the results of our theoretical and experimental investigations regarding the application of semi-transparent microparticles in optical tweezers (OT). First, we have reported that Bi_2Te_3 and Bi_2Se_3 topological insulator (TI) particles present an unusual behavior whenever subjected to a Gaussian laser beam OT [1] [W. H. Campos et. al., *ACS Photonics* **5**, 741 (2018)]. In fact, we have seen that these particles oscillate toward the optical axis of the laser beam in a quasi-periodic motion. We analyze the dynamic quantities such as amplitude and frequency of oscillations, as well as their dependencies on the size of the particle and power of the laser beam. An effective model is also proposed to describe the optical and radiometric forces exerted on the particles. It is worth mentioning that, to our best knowledge, this effect was not previously reported in the literature. We also discuss the absorption of light by semi-transparent particles, which contributes to the generation of radiation pressure and heating of the system. A microscopic model for the optical trapping of light-absorbing particles requires a clear distinction between the radiative and radiometric forces. Unfortunately, most theoretical models available in literature usually neglect such effects [2–6]. In this regard, we propose a generalization of the Ashkin's model for the radiative force exerted by a light ray on a spherical bead, including the contribution due to absorption/attenuation of light by the particle [7] [W. H. Campos et. al., *Appl. Opt.* **57**, 7216 (2018)]. Finally, we present our results regarding the optical trapping of germanium particles in an OT setup [8] [W. H. Campos et. al., *Phys. Rev. Research* **1**, 033119 (2019)]. We have observed that these particles also exhibit quasi-periodic oscillations, with the novelty that the direction of oscillation highly depends on the polarization of the laser beam. We also propose a

modification in our model for the inclusion of such a new feature.

In addition to the works mentioned above, this thesis is also devoted to our works on topological states of matter. More specifically, during my Masters studies (concluded in 2016) we have started with the investigation of the topological magneto-electric effect in TI's, for which we showed that the position of a point-like electric charge near the magnetically caped semi-spherical surface of a TI can be used to reverse the sign of the induced image magnetic monopole inside its bulk. During the first semester of my PhD, we have extended this investigation to a semi-cylindrical TI surface. For the sake of completeness, here we discuss both results, which are very similar and were published together in Ref. [9] [W. H. Campos et. al., *Phys. Lett. A* **381**, 417 (2017)]. We also present our preliminary results on the higher order topology analysis of electronic band structures in models with magnetic ordering. More specifically, we have investigated spinful (anti)ferromagnetic variations of a second order TI and the topological antiferromagnetic (AF) material CuMnAs, as well as its ferromagnetic (FM) variation. These last studies were started during my PhD "Sandwich" scholarship in Germany, in the groups of Prof. Jairo Sinova and Dr. Karin Everschor-Sitte. Since our investigations are still in progress, the results are not published yet.

This thesis is structured as follows: Chapter 1 provides an introduction about both themes of the thesis, in which Section 1.1 is devoted to OT and Section 1.2 is devoted to topological states of matter. Thereafter, the thesis is divided into two parts. Part I includes three chapters discussing our investigations in OT, while in Part II has two chapters discussing our investigations with topological matter. Finally, in Chapter 7 we present our final conclusions and prospects for future research.

Before we proceed to Sections 1.1 and 1.2 of the Introduction, an important note is in order. Most chapters of this thesis discuss works that have already been published in scientific journals, having me as their first author. In the absence of specific/clear policies regarding the inclusion of published material in thesis and dissertations of the Federal University of Viçosa (UFV), and in mutual agreement with the advisor, both text and figures from these papers were used in the corresponding chapters. The published contents were used in their entirety, with some changes for pedagogical and formatting purposes. For example, parts of the texts were modified and used in short introductions at the beginning of each chapter and figures were renumbered for better referencing along

the document. In our understanding, such use by the authors is covered by the copyright policies available on each publisher's website. When such information was not available, written permission was obtained from the publisher (via email). Some publishers adopt the RightsLink system, from which automatic permissions were obtained. The appropriate citations and copyright credit lines are included in the beginning of each chapter containing published material, along with direct links to the webpages of the works.

1.1 Optical tweezers

The idea of optical trapping and manipulation of micrometer-sized objects was conceived by A. Ashkin and collaborators and disclosed in their early 70's seminal papers [2, 10, 11]. Their work gave rise to the rapidly growing field of optical tweezers (OT) and Ashkin himself applied the technique for the remote manipulation of viruses and bacterias in aqueous solution [12]. His invention of OT and their application to biological systems granted A. Ashkin half of 2018's Nobel Prize "for groundbreaking inventions in the field of laser physics", with the other half being split between G. Mourou and D. Strickland [13].

Several variations of the experimental setup initially proposed by Ashkin can be found in the literature [14–16]. Although much modern apparatus such as holographic tweezers [16, 17] are becoming popular nowadays, it is still more frequent to come across OT whose laser intensity has a Gaussian profile [18–20]. Besides being simple and accessible, Gaussian laser beam OT can be equipped with phase contrast masks to bring about interesting variations, such as annular profile beams [21]. In this thesis we work exclusively with Gaussian laser beam OT, in which an objective lens of high numerical aperture is used to focus the beam, producing the optical trap [18].

When subject to a highly focused Gaussian light beam, dielectric particles are known to yield stable trapping in three dimensions. There are three main theoretical descriptions for OT, in which the applicability of each one of them is based on the comparison between the particle radius, l, and the laser wavelength, λ. A theoretical description in the *geometrical optics regime* can be applied whenever $\lambda << l$ and was developed by R. Gauthier, S. Wallace and A. Ashkin [2, 3]. This description uses the Snell's law of refraction in order to calculate the optical forces. In turn, J. Gordon provided a description for OT in the *Rayleigh regime* [4], which treats the spherical particle as a dipole moment and

can be applied whenever $\lambda >> l$. Finally, P. Maia Neto, H. M. Nussenzveig and coworkers developed a formalism based on the Mie-Debye spherical aberration theory which is valid for an arbitrary particle radius. However, due to high computational cost it is often more appropriate to be used in the *Mie regime*, *i.e.* when $\lambda \sim l$ [5, 6]. In order to introduce the basic ideas and a first qualitative analysis of OT, we focus on the geometrical optics regime, for it is much more intuitive and also leads to very good results when compared with experiments. A detailed qualitative description of the optical forces in the geometrical optics regime is given in Subsection 1.1.1. In Subsections 1.1.2 and 1.1.3, we briefly discuss the Rayleigh and Mie regimes, respectively.

In the usual form, OT work based on linear momentum transfer from a highly focused laser beam to a particle with refractive index greater than that of the surrounding medium, $n_p > n_m$ (deionized water have $n_m \approx 1.33$, being used in the majority of the experiments). The gradient force comes about by refraction of the light rays reaching the surface of the particle, being responsible for its trapping near the focus of the objective lens. Fig. 1.1 (left panel) depicts a spherical particle under a Gaussian laser beam OT, with two rays being refracted by the particle surface. The beam intensity at the objective entrance decays with the radial distance from its center, ρ, and can be written as:

$$I(\rho) = I_0 \exp\left(\frac{-2\rho^2}{\sigma^2}\right), \tag{1.1}$$

where I_0 is the intensity at $\rho = 0$. The beam waist, σ, is obtained by fitting Eq. (1.1) with experimental data. Usual techniques consist of analyzing a digital image of the laser beam with a ruler calibration or measuring the intensity profile from the laser power going through a diaphragm as a function of its radius [18, 22, 23]. The ray with wave vector $\vec{k}_1$ coming from the central portion of the beam generates a force $\vec{F}_1$ on the sphere when refracted by its surface. As $\vec{F}_1$ points toward the focus of the beam, it favors the trapping of the particle. On the other hand, a ray with wave vector $\vec{k}_2$ coming from the farthest portion of the beam generates a force $\vec{F}_2$ that opposes the trapping. However, as the intensity profile has a Gaussian shape, $|\vec{F}_1| > |\vec{F}_2|$, and the resulting force points toward the laser focus. Fig. 1.1 (right panel) shows a different situation, in which the particle is above the objective focus. Notice that even in this situation the resultant force happens to point toward the laser focus. The reader can easily convince himself that, regardless the relative position of the particle, the total gradient force resulting from all the rays

reaching the particle points towards the focus of the laser beam [18].

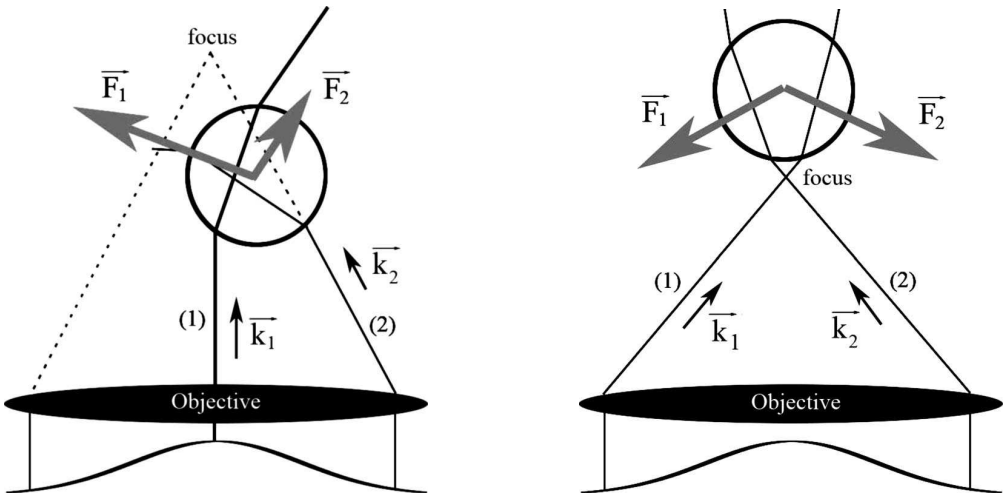

Figure 1.1: Sketch of a spherical bead under a Gaussian laser beam optical tweezers. If the refractive index of the particle is greater than that of the surrounding medium, refraction of the light rays at the particle surface generates a gradient force that pulls it toward the focus of the laser beam. Adapted from Ref. [18].

The optical force is a result from the competition between the gradient force, generated by refraction related linear momentum transfer, and radiation pressure, for which both reflection and absorption of light are responsible. The former is usually attractive, while the latter tends to drive the particle away from the focus region. Besides radiation pressure, the absorption of light from the laser beam generates inhomogeneous heating of the particle and the surrounding medium due to energy transfer. The resulting temperature gradient generates a radiometric force pointing toward the coldest region in the vicinity of the particle (Fig. 1.2). Since the laser intensity increases as we approach the optical axis, there is a component of the radiometric force toward the opposite direction, hindering the trapping. In other words, radiation pressure and radiometric forces tend to

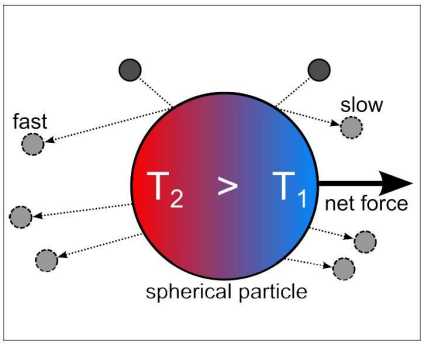

Figure 1.2: Generation of the radiometric force by inhomogeneous heating of a spherical particle and its surrounding medium. The unbalance between the kinetic energy of the water molecules in regions with temperatures T_1 and T_2 results in net force towards the region of smaller temperature. Adapted from Ref. [24].

push the object away from the laser focus, while gradient forces compose the attractive counterpart. Successful optical trapping takes place whenever the gradient force overcome the repulsive ones [2, 10, 25, 26]. Therefore, dielectric transparent particles are adopted in most experiments with optical tweezers, in order to avoid heating effects and improve the trapping efficiency.

Nowadays, OT represent an important tool in many interdisciplinary areas between physics, chemistry and biology. Some examples are the study of biological cells, macromolecular systems, single biopolymers, interface and colloid science, microfluidics, material sciences, solution-phase chemistry and others, allowing mechanical studies of small soft matter systems [12, 16, 17, 27–45]. More recently, optical tractor beams have been used for microscopic transport of airborne particles [46], contributing to studies in aerosol science [47–54]. The OT technique has also been applied to probe Casimir interactions at the micro and nanometer scale [55, 56]. Broad review articles and a step-by-step guide to the realization of OT can be found in Refs. [14–17, 57].

1.1.1 Geometrical optics regime

Here we show how to obtain the optical forces exerted by a single light ray on a spherical bead in the geometrical optics regime. In addition, we exemplify how the result can be applied to calculate the total radiative force on a particle under a Gaussian laser beam OT.

The theory for OTs in the geometrical optics regime was developed by R. Gauthier, S. Wallace and A. Ashkin [2, 3], so here we follow the main ideas of Ref. [2] to obtain the optical forces. In their model, the authors obtain the radiative force by computing the variation of the linear momentum of light, as a result of the interaction with the particle surface. They do not consider absorption of light by the particle, so that only reflection or refraction by the surface change the linear momentum of the light ray.

Consider a single ray of power dP interacting with a spherical bead (Fig. 1.3). When the ray reaches the bead surface, a fraction R of the incoming power is reflected and a fraction $T_{surface} = 1-R$ is transmitted through the interface (i.e. R is the reflectivity and $T_{surface}$ is the transmissivity at the surface). It is worth emphasizing that in many papers and textbooks the transmissivity concerns the fraction of the power remaining after crossing the entire length of the material in the direction of light propagation. However,

in Ashkin's model only the transmissivity at the surface is taken into account. This is not important for their model because the particle is considered to be fully transparent in the bulk, that is, all light that penetrates the surface will reach the opposite side of the particle. However, in Chapter 3 we will see that changes have to be made in the model if one deals with light-absorbing materials.

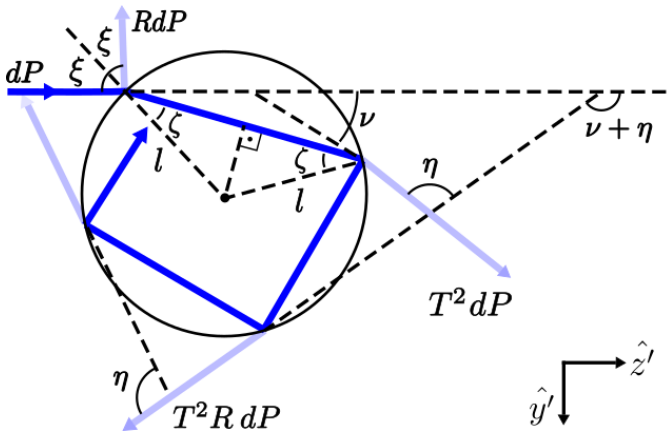

Figure 1.3: Light ray interacting with a transparent particle. Once the light ray is reflected and refracted by the external surface of the particle, its refracted portion splits again every time it reaches the inside surface. Linear momentum is transferred from the light ray to the particle, contributing to its trapping. ξ and ζ are the incidence and refraction angles, respectively, and l is the sphere radius. Adapted from Ref. [7].

An expression for R can be obtained by considering a linearly polarized light ray and taking the average over the two laser polarizations, TE and TM. Assuming no preferential polarization, the reflectivity can be written as [18, 58]:

$$R(\xi,\zeta) = \frac{1}{2}\left[\frac{\sin(\xi-\zeta)}{\sin(\xi+\zeta)}\right]^2 + \frac{1}{2}\left[\frac{\tan(\xi-\zeta)}{\tan(\xi+\zeta)}\right]^2. \tag{1.2}$$

The refraction angle reads $\zeta(\xi) = \arcsin\left[\frac{n_m}{n_p}\sin\xi\right]$ (Snell's law), where ξ is the angle of incidence, n_m is the refractive index of the surrounding medium and n_p is the refractive index of the particle.

As a result of the reflection and refraction, linear momentum is transferred from the light ray to the bead, exerting a force whose magnitude and direction depends on the angle of incidence, ξ. Let us choose the z'-axis to be in the direction of the incident ray, and the y'-axis to be in the plane of incidence, which contains both the light ray and the center of the particle (Fig. 1.3). Details on the calculations are provided below, but the

final force exerted on the bead can be written as [2, 18]:

$$d\vec{F} = \frac{n_m}{c}[\mathrm{Re}(Q_t)\hat{z}' + \mathrm{Im}(Q_t)\hat{y}']dP, \tag{1.3}$$

where c is the speed of light, and

$$Q_t = 1 + R\exp(2i\xi) - T^2\frac{\exp[2i(\xi-\zeta)]}{1+Re^{-2i\zeta}} \tag{1.4}$$

is the dimensionless force efficiency (also known as the dimensionless vector efficiency factor).

In order to obtain Eq. (1.3), we notice that once the incident light ray penetrates the interface, there will be new reflections/refractions every time it interacts with the inside surface (Fig. 1.3). In each interaction, a fraction T^2R^n of the initial power leaves the particle in a different direction than that of the incident ray (n accounts for the number of times the ray was reflected before leaving the particle), i.e., there is also a transfer of linear momentum from the ray to the particle due to multiple reflections/refractions. The change in the linear momentum of the sphere is obtained by summing the infinite series of ray-surface interactions, with $d\vec{p}_{particle} = -d\vec{p}_{ray}$.

From Fig. 1.3, it can be seen that the component of the radiative force along z'-axis is given by [2]:

$$dF_{z'} = \frac{n_m}{c}\Big\{1 + R\cos(2\xi) - T^2\sum_{n=0}^{+\infty} R^n\cos(\nu + n\eta)\Big\}dP, \tag{1.5}$$

where $n = 0, 1, 2, 3...$ is an integer number, and the angles ξ, ζ, ν, η are indicated in Fig. 1.3. This can be easily shown to be

$$dF_{z'} = \frac{n_m}{c}\mathrm{Re}\Big\{1 + Re^{2i\xi} - T^2\frac{e^{i\nu}}{1-Re^{i\eta}}\Big\}dP. \tag{1.6}$$

Using the geometric relations $\nu = 2\xi - 2\zeta$ and $\eta = \pi - 2\zeta$, one obtains

$$dF_{z'} = \frac{n_m}{c}\mathrm{Re}\Big\{1 + Re^{2i\xi} - T^2\frac{e^{2i(\xi-\zeta)}}{1+Re^{-2i\zeta}}\Big\}dP. \tag{1.7}$$

In turn, along y'-axis, we have that:

$$dF_{y'} = \frac{n_m}{c}\Big\{R\sin(2\xi) - T^2\sum_{n=0}^{+\infty} R^n \sin\left(\nu + n\eta\right)\Big\}dP. \tag{1.8}$$

Proceeding in an analogous way, one gets:

$$dF_{y'} = \frac{n_m}{c}\mathrm{Im}\Big\{Re^{2i\xi} - T^2\frac{e^{2i(\xi-\zeta)}}{1+Re^{-2i\zeta}}\Big\}dP. \tag{1.9}$$

Note that the compact expression (1.3) is equivalent to Eqs. (1.7) and (1.9).

Now, consider a Gaussian laser beam OT, whose intensity profile at the objective entrance is given by Eq. (1.1). The power element of a particular incident ray labeled by the cylindrical coordinates ρ and φ (the azimuthal angle) can be obtained using $dP = I(\rho)dA$, where $I(\rho)$ is given by Eq. (1.1) and $dA = \rho d\rho d\varphi$ is an area element of the objective. Therefore,

$$dP = I_0 \exp\left(\frac{-2\rho^2}{\sigma^2}\right)\rho d\rho d\varphi. \tag{1.10}$$

If we calculate the total beam power before the coverslip,

$$P_t = \int_0^{2\pi}\int_0^{\infty} I_0 \exp\left(\frac{-2\rho^2}{\sigma^2}\right)\rho d\rho d\varphi = \frac{\pi\sigma^2}{2}I_0, \tag{1.11}$$

then Eq. (1.10) can be written as

$$dP = \frac{2P_t}{\pi\sigma^2}\exp\left(\frac{-2\rho^2}{\sigma^2}\right)\rho d\rho d\varphi. \tag{1.12}$$

After the objective, however, it is more convenient to label the ray by the angle θ between the ray and the optical axis. Let the z-axis be placed along the optical axis, pointing toward the objective lens [Fig. 1.4 (left panel)], and choose the origin of the coordinate system to be at the laser focus. Now, we use the Abbe sine condition for microscope objectives [18],

$$\rho = f\sin\theta, \tag{1.13}$$

where $f = n_g R_0/\mathrm{NA}$ is the focal length of the objective. n_g is the glass refractive index, R_0 is the maximum value of ρ and NA is the numerical aperture of the objective. Applying the Abbe sine condition to Eq. (1.12), the power increment dP of a single light ray can be written as

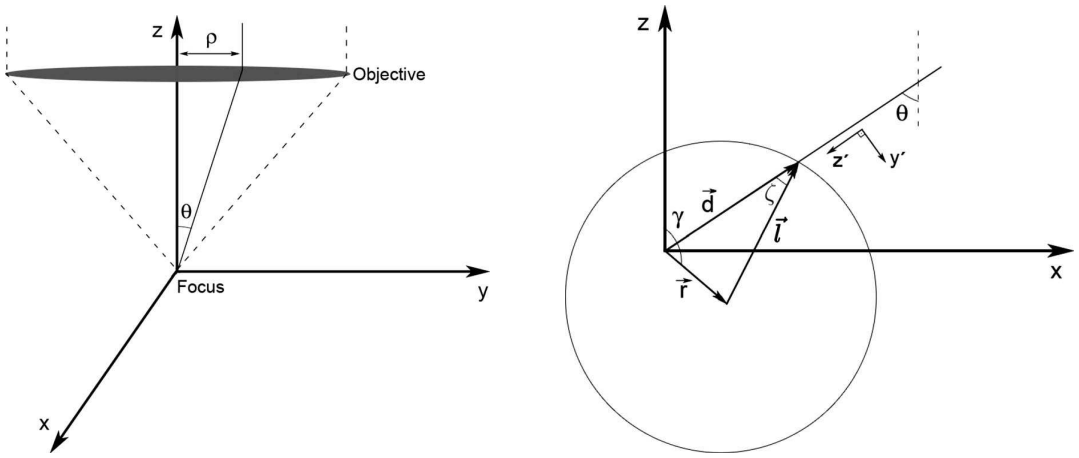

Figure 1.4: (*Left panel*) Reference coordinate frame for a single light ray being focused by the objective lens. ρ and θ are the radial distance and the angle between the optical axis and the point where the ray leaves the objective, respectively. The origin of the coordinate frame is chosen to be at the objective focus. (*Right panel*) Spherical particle in an arbitrary position near the focus of the objective lens. $\vec{r}$ labels the particle position relative to the objective focus. γ is the angle between $\vec{r}$ and the z-axis. $\vec{l}$ and $\vec{d} = \vec{r} + \vec{l}$ are the vectors connecting the center of the particle and the origin of the coordinate frame to the point where the incident ray intersects the particle surface, respectively. Adapted from Ref. [18].

$$dP = \frac{2P_t}{\pi\sigma^2} \exp\left(\frac{-2f^2 \sin^2\theta}{\sigma^2}\right) f^2 \sin\theta \cos\theta d\theta d\phi. \tag{1.14}$$

With Eqs. (1.3) and (1.14) in hands, we can proceed to the calculation of the total optical force with

$$\vec{F} = \int_0^{2\pi} \int_0^{\theta_0} d\vec{F}. \tag{1.15}$$

Notice that not all the rays of the beam will actually reach the particle. As the rays go through the objective, they undergo refraction at the glass-medium interface. It is easy to see that θ_0 depends on the distance h from the center of the particle to the coverslip surface. Due to spherical aberration, fewer rays reach the particle as h increases [18]. If we consider the particle to be nearly touching the coverslip surface, than all rays that pass through the coverslip surface will reach the particle and θ_0 is the critical angle for total internal reflection. For an interface of glass with deionized water used in most experiments, we have $\theta_0 = 63.55°$ for the critical angle [18].

In order to actually calculate the total force exerted on the particle, we need to write Eq. (1.3) as a function of θ and φ. For this, notice that Q_t depends on the angles

ξ and ζ. Therefore, all we have to do is to write these angles as functions of θ and φ.

Fig. 1.4 (right panel) shows the particle in an arbitrary position near the focus of the objective lens. The position of the particle is given by the vector $\vec{r}$, where the origin of the coordinate frame is taken as the objective focus and γ is the angle between $\vec{r}$ and the z-axis. Let $\vec{l}$ be the vector connecting the center of the particle to the surface point where the incident ray intersects the particle and $\vec{d} = \vec{r} + \vec{l}$ the vector connecting the origin of the coordinate frame to the same surface point. From Fig. 1.4 (right panel), one can see that

$$\xi = \arccos\left[\frac{d^2 + l^2 - r^2}{2ld}\right], \tag{1.16}$$

with

$$d = \sqrt{l^2 - r^2 + r^2(\sin\gamma\sin\theta\cos\varphi + \cos\gamma\cos\theta)^2} + r(\sin\gamma\sin\theta\cos\varphi + \cos\gamma\cos\theta). \tag{1.17}$$

The ζ angle is given by the Snell's law, $\zeta = \arcsin\left[\frac{n_m}{n_p}\sin\xi\right]$, while the unitary vectors are given by

$$\hat{z}' = (-\sin\theta\cos\varphi, -\sin\theta\sin\varphi, -\cos\theta) \tag{1.18}$$

and

$$\hat{y}' = \frac{\hat{z}' \times (\vec{r} \times \hat{z}')}{\hat{z}' \times (\vec{r} \times \hat{z}')}. \tag{1.19}$$

Now that all variables are written in terms of θ and φ, one can calculate the force exerted on the particle by numerical evaluation of Eq. (1.15).

1.1.2 The Rayleigh regime

The theory for OT in the Rayleigh regime was proposed by J. Gordon [4], being applicable whenever the radius of the particle is much smaller than the light wavelength ($l << \lambda$). Actually, the Rayleigh scattering is valid in situations in which the beam phase shift is small when refracted by the particle, so that $2kl(n_r - 1) << 1$ [18], where k is the wave vector in the surrounding medium, l is the particle radius and $n_r = n_p/n_m$ is the relative refractive index. As in most experimental setups of OT the surrounding medium is deionized water ($n_r > 1$), the previous condition can be usually simplified to $l << \lambda$, since $k = 2\pi n_m/\lambda$.

In this approach, the small particle is considered to be an electric dipole induced by the electric field of the laser beam, which in turn is taken as approximately uniform around the dipole. The dipole moment of a dielectric sphere located in an uniform electric field, $\vec{E}$, is solved in many textbooks on electromagnetic theory and is given by [58, 59]

$$\vec{p} = 4\pi\epsilon_m \frac{\epsilon_r - 1}{\epsilon_r + 2} l^3 \vec{E}, \tag{1.20}$$

where $\epsilon_r = \epsilon_p/\epsilon_m$ is the relative permittivity, ϵ_p and ϵ_m are the particle and medium electric permittivities, respectively.

In turn, the force exerted on the dipole reads

$$\vec{F} = -(\vec{p} \cdot \vec{\nabla})\vec{E}. \tag{1.21}$$

By substituting Eq. (1.20) into (1.21) and using the relation

$$\vec{\nabla}\vec{E}^2 = 2(\vec{E} \cdot \vec{\nabla})\vec{E} + 2\vec{E} \times (\vec{\nabla} \times \vec{E}), \tag{1.22}$$

along with $\vec{\nabla} \times \vec{E} = 0$, we obtain the gradient force exerted on a spherical particle in the Rayleigh regime:

$$\vec{F}_g = \frac{1}{2}\alpha\vec{\nabla}E^2, \tag{1.23}$$

where

$$\alpha = 4\pi\epsilon_m \frac{\epsilon_r - 1}{\epsilon_r + 2} l^3 \tag{1.24}$$

is the particle polarizability [60, 61].

1.1.3 Mie regime

In many applications of OT, the size of the trapped object is comparable to the laser wavelength, so that neither a geometrical optics nor Rayleigh scattering description is appropriate. Therefore, it was necessary the development of a first-principles theory that allows for absolute calibration even in these situations. The theory accounts for the spherical aberration at the glass-medium interface and is based on an optical (electromagnetic) representation of the highly focused laser beam produced by the objective [62]. The

Mie-Debye spherical aberration (MDSA) theory is valid for an arbitrary value of the particle radius, and the calculations were performed by P. Maia Neto, H. M. Nussenzveig and coworkers [5, 6]. Although more complicated, this theory involves no adjustable parameters, so that an absolute comparison between theory and experiments can be achieved [18].

A detailed description of the MDSA theory is beyond the scope of this thesis. Therefore, we only briefly discuss the results for the transverse trap stiffness and their comparison with experimental data. For this, we consider a highly focused laser beam represented in cylindrical coordinates and define the dimensionless efficiency factor, $\vec{Q} = (Q_\rho, Q_\phi, Q_z)$, as

$$\vec{Q} = \frac{c\vec{F}}{n_m P}, \tag{1.25}$$

where c is the velocity of light in vacuum, $\vec{F}$ is the total force exerted on the particle and P is the power of the incident laser beam. In turn, the transverse stiffness reads [62]

$$\kappa_\rho = -\frac{n_m P}{c}\left(\frac{\partial Q_\rho}{\partial \rho}\right)_{z=z_{eq}}. \tag{1.26}$$

where z_{eq} is the equilibrium position at the z-axis, *i.e.* the point in the optical axis at which $\vec{Q} = 0$.

Historically, there were two major steps on the development of the MDSA theory. Fist, the electromagnetic generalization of Debye's scalar theory for a strongly focused beam was combined with the Mie scattering theory for a dielectric sphere, so that spherical aberration produced at the interface between the glass coverslip and the medium is taken into account [23, 63]. The results reproduced very well the experimental data for large particle sizes. However, for particle radius smaller then the laser wavelength the MDSA theory highly overestimates the trapping stiffness [22]. The second step concerns the implementation of optical setup aberrations to the model, which finally led to very good agreement with experiments for all particle sizes [6].

Fig. 1.5 shows the results for the transverse trap stiffness for either Mie-Debye spherical aberration theory (MDSA) and its extension with inclusion of optical aberration effects (MDSA+), for a spherical particle of radius ℓ, ranging from Rayleigh to geometrical optics regimes. Experimental results for four different particle sizes are also included for comparison. Notice that optical setup aberration effects, specially astigmatism, are

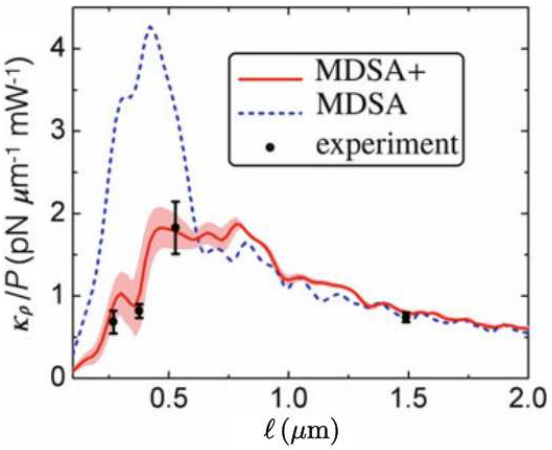

Figure 1.5: Transverse trap stiffness per unit power, κ_ρ/P, versus particle radius, ℓ, for experimental measurements (black dots), MDSA (dashed) and MDSA+ (red line) theories from Rayleigh ($\kappa \propto \ell^3$) to geometrical optics ($\kappa \propto 1/\ell$) regimes. Adapted from Ref. [62].

extremely important for the Rayleigh and Mie regimes. Remarkably, the theoretical results for MDSA+ theory agree with experimental data within error bars, with absolutely no fitting procedure.

Although calculations based on MDSA scattering theory leads to very accurate results, for spheres of radius ℓ larger than the light wavelength, λ, the Mie series converges slowly and intricate computational techniques are necessary to overcome this inconvenience [64, 65]. In such regime, the geometrical optics approach leads to simpler results with considerably good accuracy, being very practical and efficient for comparison with experimental observations [7].

1.1.4 Metallic particles in OT

In order to trap small particles in optical tweezers, one has to consider the optical properties of the material from which they are made, since they are decisive for the action of the final forces on the object. As explained before, the optical trapping of dielectric particles is based on the competition between radiation pressure and the gradient force. The former occurs whenever light is reflected or absorbed by the particles, while the latter comes about from light refraction. In general, stable trapping occurs whenever gradient force dominates, in such a way that the particle is kept around the laser beam focus [18]. The absorbed part of the ray also generates the so-called radiometric force, related to thermal effects. If the particle is transparent, this force is smaller than the gradient force, and it is expected that fully transparent particles should be trapped in

optical tweezers, while metallic particles should not. In fact, when subjected to a highly focused Gaussian light beam, dielectric particles are known to yield stable trapping in three dimensions, since gradient forces overcome both radiation pressure and radiometric forces [1, 18, 34, 66]. On the other hand, metallic particles are usually pushed away, since light is mostly reflected and/or absorbed by the material. In fact, the stable optical trapping of metallic particles only occurs under very special conditions [66–69].

In the Rayleigh regime, in which particles are very small, the gradient force is proportional to the polarizability of the material [Eq. (1.23)] and metallic particles can be trapped in three dimensions more efficiently than dielectric ones. For the ratio of the gradient by the scattering force in the Rayleigh regime, we have $F_g^{(m)}/F_{scat}^{(m)} \propto l^{-3}$ [66]. It is important to say that in this regime the trapping force is very small, regardless if the particle is dielectric or metallic. Also, heating of the system by absorption of light, and therefore the radiometric force, are known to be negligible for Rayleigh particles. In the Mie and geometrical optics regimes, the optical trapping of metallic particles is more complicated. A possible way is to implement an inverted "doughnut" laser beam to levitate the bead using the radiometric force [See Fig. 1.6 (left panel)] [70]. Another

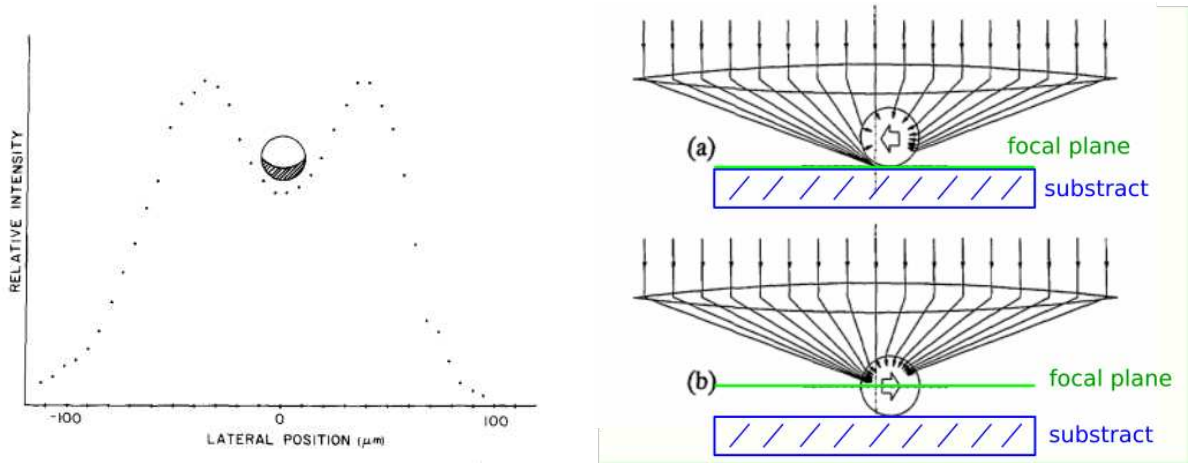

Figure 1.6: (*Left panel*) Metallic particle trapped in an inverted "doughnut" laser beam. The radiometric force exerted by the light on the particle balances its weight and prevents its escaping sideways. Adapted from Ref. [70]. (*Right panel*) Metallic spherical particle trapped against a substrate (blue) by radiation pressure. (a) If the bead is between the focal plane (green) and the objective lens, stable trapping can be achieved. (b) Otherwise, the particle is scattered by the light beam. Adapted from Ref. [71].

option is to hold the particle against a substrate [See Fig. 1.6 (right panel)], in which the radiation pressure itself can be used to yield the trapping [71]. Notice that in this case the stability of the optical trapping is bi-dimensional, and highly depends on the height

of the particle relative to the focal plane. If the metallic bead is between the objective lens and the focal plane, radiation pressure can trap the particle. On the other hand, a bead below the focal plane is scattered by the radiation pressure. Due to this delicate dependence on the radiation pressure, trapping in this configuration is only possible when it overcomes the radiometric force.

In Ref. [72], the authors provide a theoretical description for the trapping of metallic particles in the geometrical optics regime, considering that all the incoming light is reflected by the surface. The scattering and gradient forces exerted by a single light ray reads

$$\begin{aligned} dF_s =& \frac{n_m}{c}(1 + R\cos 2\theta) \\ dF_g =& \frac{n_m}{c}\sin 2\theta, \end{aligned} \tag{1.27}$$

where θ is the angle of incidence at the particle surface.

1.1.5 Absorption of light by the particle

Absorption of light by trapped particles in OT is usually neglected in theoretical models and avoided in experiments, for it results in the generation of radiometric forces (also called photophoretic forces, when caused by light [10, 73]) [70, 72]. However, radiometric effects have become not only important, but also useful in optical control and manipulation of microparticles. For example, inhomogeneous heating of the medium was recently reported as an efficient method for the optothermal trapping of particles in a hollow-core photonic crystal fiber [74, 75]. In usual Gaussian beam setups, the photophoretic forces tend to scatter the particles from the optical region, but they are exactly the same forces responsible to levitate metallic particles in a "doughnut" laser beam [70]. In Ref. [76], the authors propose a method for measuring the incident laser power using the absorption of light by a small mercury bead that jumps when it reaches the boiling temperature of water. Although for metallic materials the radiometric forces highly overcomes the radiative forces, if the particle is semi-transparent they can compete, eventually yielding to quasi-periodic oscillations, as recently observed for TI (Bi_2Te_3 and Bi_2Se_3) particles in aqueous solution (see Chapter 2) [9]. Additionally, similar effects were also

observed to occur for germanium (Ge) [8] and silicon (Si) [77] microparticles under OT with Gaussian intensity profiles.

The optical trapping and manipulation of light-absorbing particles have been studied experimentally in different configurations [46, 47, 49, 51, 54]. It has been also studied analytically in Rayleigh regime [66], and by finite-difference time-domain simulations for particles in Lorentz-Mie regime [78]. However, to our best knowledge, an analytical expression for the radiative force exerted on an absorbing particle in the geometrical optics regime is still lacking. In Chapter 3, we propose a generalization of the Ashkin's model in order to account for absorption/attenuation of light in the bulk of the particle, contributing to fill this gap in the literature [7].

1.1.6 The Stokes force and the Brownian motion

Any object moving in a viscous medium, such as air or water, experiences a drag force that opposes to its movement. If the object is a small spherical particle, this force is also known as the Stokes force, and plays a very important role in OT experiments. In fact, it is a key ingredient for the classic calibration of OT [18]. As the name suggests, an expression for the Stokes force was derived by G. Stokes in 1851 [79], being written as

$$\vec{F}_S = -6\pi\eta l\vec{v}, \tag{1.28}$$

where η is the viscosity of the medium, l is the radius of the particle and $\vec{v} = d\vec{r}/dt$ is its instantaneous velocity. All experiments in this thesis were conducted in deionized water, for which $\eta = 8.9 \times 10^{-4}$ Pa.s at $25\,^o$C.

For usual optical traps, in which displacements are small, the particle-trap interaction is approximately that of a harmonic potential [18, 80]. The "spring constant" in this case is called *trap stiffness*, being usually represented by the Greek letter κ. It is also important to mention that the trapped particles suffer position fluctuations due to thermal excitation, the well-known Brownian motion [81, 82]. As long as these fluctuations are within the confining harmonic potential, the particle remains trapped in the optical region. Many other forces can be in place, such as adhesion forces between particles, electrostatic forces, magnetic forces and more [83]. Therefore, the overall dynamics is very complicated, and its full understating is still an ongoing effort. In the works of

this theses we are concerned either with the optical forces or with dynamics regimes in which Brownian motion is negligible. For this reason, it is not taken into account in our calculations and experiments.

1.2 Topological matter

Topology has been one of the most remarkable and important concepts in condensed matter physics in the last decade [84–95]. Although the discovery of the TI's in 2006 was definitely responsible for the large increase of interest in this area, the idea of topological order appeared in the early 70's with the Berezinskii-Kosterlitz-Thouless transition [96, 97] and topological states of matter such as quantum Hall systems and superfluid helium are known since the early 1980's [98–102]. Mathematicians formalized the idea of topology to classify three-dimensional objects based on properties that are preserved under continuous (or smooth) transformations, such as stretching or twisting, but not under drastic transformations, such as tearing or gluing. Consider, for example, objects with simple surfaces, such as billiard balls or light bulbs. The surfaces of these objects can be classified as *topologically trivial*, as opposed to the surfaces of objects such as coffee mugs or "doughnuts", which have single holes in their surfaces, making them *topologically nontrivial*. Naturally, the classification can be extended if we include more complex objects, such as pretzels with 3 holes, and so forth. Different objects falling into the same class can be smoothly deformed into each other and are said to be *topologically equivalent* [92]. Nowadays, topology is used in many areas of physics, but an essential feature is that each topological class is characterized by a robust quantity, called *topological invariant*. Such quantity plays a very important role in any topological classification, since it does not change as an object is smoothly deformed into a topologically equivalent one.

The topology of the objects in the example above can be analyzed using the "Gauss-Bonnet theorem", which relates the integral of the Gaussian curvature over the surface with its "genus", that is, the number of holes on the object [103]. Therefore, the genus is a topological invariant, since it does not change as the object is continuously deformed. In condensed matter physics, the "object" to be classified is the Hamiltonian of the system. In order to define a "smooth" transformation in this context, we consider an energy gap

separating the occupied states from the empty ones. A transformation in this Hamiltonian carried out so that its parameters change slowly (adiabatic interpolation) is said to be smooth if it does not close such energy gap. In what follows, we discuss these ideas with a little more detail, starting with the TKNN topological invariant for the quantum Hall effect, followed by 2D and 3D TI's. Along with these examples, we also introduce other topological phases of matter that are relevant to us, such as topological crystalline insulators (TCI's) and higher order topological insulators (HOTI's). Finally, we briefly discuss a very recent subarea at the interface between topology and spintronics, the "topological antiferromagnetic spintronics".

1.2.1 The quantum Hall effect and the TKNN invariant

The discovery of the classical Hall effect in 1879 by Edwin Hall [104] was of great importance to material physics. Due to the Lorentz force acting on the free electrons, a magnetic field applied perpendicularly to a sheet of metal induces an electric voltage across a region in a direction perpendicular to that of the applied charge current. The Hall effect provides a simple means of determining the sign of the charge carriers in metals and semiconductors. In a two-dimensional electron gas at a very low temperature and subjected to a strong perpendicular magnetic field, quantum effects play an important role. The Hall conductance becomes quantized in units of e^2/h (e is the electronic charge and h is the Planck constant), while longitudinal resistance drops to zero [105]. In fact, in 1980 K. von Klitzing reported the experimental observation of the quantum Hall effect (QHE) [98]. This discovery was as important as its classical counterpart, because it has encouraged researchers to expand our understanding of condensed matter systems. Until then, all known states of matter could be described by the formalism proposed by Landau, in which a phase transition is always related to the breaking of an intrinsic symmetry of the system.

Topology is at the heart of the QHE, which was the first topologically non-trivial state of matter to be observed. All previously known states are topologically trivial, whose response functions are well-behaved except at critical points. Phases with topological order, on the other hand, have at least one response function which is a topological invariant, that is, that do not change smoothly with continuous deformations in the Hamiltonian. In fact, they are very robust to perturbations, except at special points

where they change abruptly. In the quantum Hall effect, such response function happens to be the Hall conductivity. The QHE can be easily understood within a semi-classical picture. Let a 2D electron gas be subjected to a perpendicular magnetic field. Due to the Lorentz force, electrons in the bulk develop cyclotron orbits, so that they do not contribute to the electronic transport and the bulk band structure is similar to that of a normal insulator (see Fig. 1.7). On the other hand, electrons at the boundaries cannot perform a closed orbit, so they propagate along the edges ("skipping orbits") and constitute one-dimensional channels [106, 107]. In other words, the electronic band structure of the QHE presents a robust "chiral" (that propagates in only one direction) edge-state connecting the bulk valence and conduction bands. If the Fermi level lies within the bulk band gap, the edge-state electrons propagate along the boundaries, while bulk electrons do not contribute to the conductivity [105].

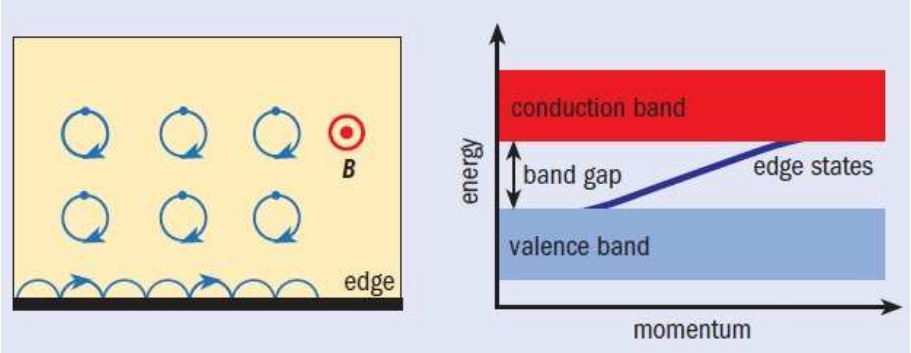

Figure 1.7: Representation of the quantum Hall effect. Electrons in the bulk of the material perform cyclotron orbits, yielding an energy band structure similar to the insulating state of matter. However, electrons are allowed to propagate along the edges of bi-dimensional material, forming a chiral channel in one dimension. Adapted from Ref. [108].

The theoretical investigation of the QHE on topological grounds was first performed by David Thouless and collaborators [99], constituting a milestone in the history of topological matter. In fact, D. Thouless shared the 2016 Nobel Prize with F. Haldane and J. Kosterlitz "for theoretical discoveries of topological phase transitions and topological phases of matter". The analytical expression for the quantized Hall conductivity is derived using the fundamental Kubo formula, whose result for a crystal lattice with periodic potential can be written as

$$\sigma_{Hall} = i\frac{e^2}{2\pi h}\sum_{n}^{occ}\int_{BZ} d^2k \left[\left\langle \frac{\partial u_{\vec{k},n}}{\partial k^y} \mid \frac{\partial u_{\vec{k},n}}{\partial k^x}\right\rangle - \left\langle \frac{\partial u_{\vec{k},n}}{\partial k^x} \mid \frac{\partial u_{\vec{k},n}}{\partial k^y}\right\rangle\right], \tag{1.29}$$

where n labels the occupied electronic bands below the Fermi level and $|u_{\vec{k},n}\rangle$ is the Bloch state for crystal momentum $\vec{k}$ and band index n. It turns out that each term of Eq. (1.29) is nothing but the Berry phase for the band n computed over the Brillouin zone (BZ), multiplied by the factor $e^2/2\pi h$ [92, 105]. Considering the Berry connection

$$\vec{\mathcal{A}}_n(\vec{k}) = i\langle u_{\vec{k},n}|\vec{\nabla}_{\vec{k}}|u_{\vec{k},n}\rangle, \tag{1.30}$$

we define the Berry curvature as

$$\mathcal{F}_n(\vec{k}) = \partial_{k_x}\mathcal{A}_y - \partial_{k_y}\mathcal{A}_x = i\left\langle \frac{\partial u_{\vec{k},n}}{\partial k^y} \mid \frac{\partial u_{\vec{k},n}}{\partial k^x} \right\rangle - i\left\langle \frac{\partial u_{\vec{k},n}}{\partial k^x} \mid \frac{\partial u_{\vec{k},n}}{\partial k^y} \right\rangle, \tag{1.31}$$

so that the Hall conductivity reads

$$\sigma_{Hall} = \frac{e^2}{2\pi h}\sum_n^{occ}\int_{BZ} d^2k\mathcal{F}_n(\vec{k}). \tag{1.32}$$

Due to the periodicity of the BZ in both x and y directions, it can be unequivocally mapped onto the closed surface of a 3D torus. As shown in detail in Ref. [109] by cutting the surface of the torus and integrating the Berry connection along the boundaries of the BZ, the single valuedness of the Bloch wave function implies that the total Berry curvature must be an integer multiple of 2π [92, 109]. Therefore, Eq. (1.29) can be written as

$$\sigma_{Hall} = \frac{e^2}{h}C, \tag{1.33}$$

where C is an integer number, known as the total Chern number. C is in fact obtained by summing the Chern numbers associated to each individual band, $C = \sum_n^{occ} C_n$, where $C_n = 1/(2\pi)\int_{BZ} d^2k\mathcal{F}_n(\vec{k})$. It is a remarkable fact that a complicated property such as the electric conductivity depends only on fundamental constants. This relationship between the Hall conductivity and the Chern number is the so-called TKNN invariant (after Thouless, Kohomoto, Nightingale and den Nijs), that is, the topological invariant associated to the QHE.

1.2.2 Topological insulators

The quantum spin Hall effect and 2D topological insulators

The discovery of the QHE gave rise to the search for new states of matter presenting topological order. In 2005, an intriguing topological phenomena known as the quantum spin Hall effect (QSHE) was predicted by C. Kane and E. Mele to take place in graphene [110]. The QSHE resembles its precursor, but have a distinct physical origin. While the QHE requires breaking of time reversal symmetry (TRS) to be realized (implemented by the application of an external magnetic field), the QSHE arises naturally from the spin-orbit coupling (SOC) in the bulk of the material. The SOC manifests in such a way that electrons experience an "effective Lorentz force", and therefore, it is often said in the literature that the SOC plays the role of the magnetic field. Interestingly, the direction of this force depends on the spin of the electron, so that electrons with opposite spins propagate in opposite directions along one-dimensional edge channels at the boundaries of the material [111] (Fig. 1.8). This remarkable property is known as "spin-momentum locking", i.e., the linear momentum direction of an electron is coupled to the direction of its spin. Due to this correlation between spin and crystal momentum, these edge-states are often referred to as *helical* edge-states [107]. Roughly speaking, the QSHE is the sum of two independent quantum Hall insulators of opposite chirality, so that the system is invariant under TRS. As a result, the total Hall conductance is zero, but the spin Hall conductance is finite and quantized as $2\frac{e}{4\pi}$ [111].

The QSHE could not be experimentally observed in graphene, because it has a very weak spin-orbit coupling, which is essential for this topological phase to occur [112, 113]. However, in 2006 Bernevig and collaborators predicted that such effect could be observed in HgTe quantum wells [114], which was in fact confirmed experimentally by König et. al. in the following year [115]. It is important to stress that the metallic edge-states arise as a consequence of the bulk band topology, which is known as *bulk-boundary correspondence*. In their paper, Bernevig et. al. used $\vec{k}\cdot\vec{p}$ perturbation theory to derive an effective model Hamiltonian for the bulk, which is known as the BHZ (after Bernevig, Hughes and Zhang) model:

$$\mathcal{H} = \begin{pmatrix} h(\vec{k}) & 0 \\ 0 & h^*(-\vec{k}) \end{pmatrix}, \tag{1.34}$$

where $h(\vec{k}) = \epsilon(\vec{k})\mathbb{I}_{2\times2} + \sum_{a=1}^{3} d_a(\vec{k})\sigma^a$, $\mathbb{I}_{2\times2}$ is the 2×2 identity matrix and

$$\begin{aligned} \epsilon(\vec{k}) &= C - D\left(k_x^2 + k_y^2\right) \\ d_a(\vec{k}) &= \left(Ak_x, -Ak_y, M(\vec{k})\right) \\ M(\vec{k}) &= M - B\left(k_x^2 + k_y^2\right), \end{aligned} \tag{1.35}$$

where A, B, C, D and M are material parameters that depend on the geometry of the quantum well. σ^a $(a = 1, 2, 3)$ are the Pauli matrices representing pseudospin degrees of freedom. It is important to point out that the real spin is not a good quantum number, since the BHZ model preserves TRS. As discussed in Ref. [116], not every basis state of the BHZ Hamiltonian [Eq. (1.34)] is purely spin up or down. However, explicit calculation of the expectation value of $\hbar\sigma_z/2$ yields $\approx \pm\hbar/2$, and therefore, the basis states can be considered as approximately spin-polarized [116].

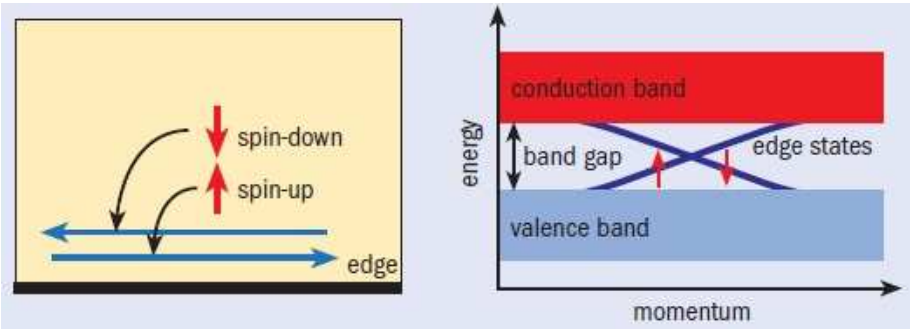

Figure 1.8: Representation of the quantum spin Hall effect and its band diagram. Electrons in the bulk of the material are localized and do not contribute to the electric current. The boundaries support two counter-propagating edge-states with spin-momentum locking, i.e. electrons propagating in opposite directions have opposite spins. These edge-states lie in the gap separating the bulk valence and conduction bands and can be described by an effective one-dimensional Dirac Hamiltonian. Adapted from Ref. [108].

Projecting Eq. (1.34) onto the edge-states leads to the following effective Dirac Hamiltonian [106]

$$H_{edge} = \hbar v_D k_y \sigma^z, \tag{1.36}$$

where v_D is the Dirac velocity of the edge-states. The eigenvalues of this Hamiltonian constitute the Dirac cone (or an "X", as the edge is one-dimensional) for the edge-states appearing in the band gap between the valence and conduction bands of the bulk (Fig. 1.8). This is the manifestation of the aforementioned *bulk-boundary* correspondence, i.e.,

the appearance of metallic edge-states as a consequence of the topological properties (more details on the topological aspects are given below) of the bulk. Note that crystal momentum is directly coupled to the electron spin ($H_{edge} \propto k_y \sigma^z$), leading to the so-called spin-momentum locking. As a result, the counter-propagating edge-states[1] have opposite spin-polarizations.

An important consequence of the spin-momentum locking in the QSHE is that backscattering between counter-propagating edge-states is forbidden. To understand this, consider the scattering of forward-moving electrons with spin up by a non-magnetic impurity (i.e., TRS is preserved). In the scattering, the electron can perform either a clockwise or a counterclockwise turn around the impurity. Since only spin-down electrons can move backwards, the spin of the incident electron must undergo either either a π or a $-\pi$ rotation in the process. These two paths have the same probability to occur and differ by a spin rotation of 2π. It is well-known that a rotation of 2π renders a negative sign to the wave function of a spin-½ particle. As a result, the two paths interfere destructively, and no backscattering can take place between the counterpropagating edge-states [106].

We have seen that an important quantity that characterizes the topology of the QHE is the TKNN invariant. However, the Hall conductivity is odd under TRS, so it is not a good indicator of topology for the QSHE, which is a time-reversal invariant system. In fact, if one calculates the TKNN invariant for the QSHE, it is found that $\sigma_{Hall} = 0$. In order to define the topological invariant for the QSHE, we examine the role of TRS for spin-½ particles [107]. The TRS can be represented by the antiunitary operator $\Theta = \exp(i\pi S_y/\hbar)K$, where S_y is the y component of the spin operator and K represents complex conjugation. For a time-reversal invariant system in a periodic lattice, the Bloch Hamiltonian[2] $\mathcal{H}(\vec{k})$ satisfies

$$\Theta \mathcal{H}(\vec{k}) \Theta^{-1} = \mathcal{H}(-\vec{k}). \tag{1.37}$$

This, and the fact that $\Theta^2 = -1$ for spin-½ electrons, results in the celebrated Kramers' theorem: for each eigenstate of the Bloch Hamiltonian at momentum $\vec{k}$, there is an orthogonal eigenstate at momentum $-\vec{k}$ with the same energy eigenvalue.

[1] Remember that the electron group velocity is given by $(v_g)_i = (1/\hbar)\partial_{k_i} E_n(k_i)$.

[2] The Bloch theorem states that the eigenfunctions of a Hamiltonian $\mathcal{H}(\vec{r})$ periodic in $\vec{r}$ can be written as $\psi_{n,\vec{k}}(\vec{r}) = e^{i\vec{k}\cdot\vec{r}} u_{n,\vec{k}}(\vec{r})$, where $u_{n,\vec{k}}(\vec{r})$ are functions (called cell-periodic Bloch states) with the same periodicity of $\mathcal{H}(\vec{r})$. It can be easily shown that the $\vec{k}$-dependent energy bands $E_n(\vec{k})$ are obtained from

The time-reversal invariant momentum (TRIM) points $\vec{\Gamma}_i$ of the BZ are defined as those $\vec{k}$ points in which $\vec{k} = -\vec{k} + \vec{G}$, where $\vec{G}$ is a reciprocal lattice vector. A well-known property of Bloch Hamiltonians is that $\mathcal{H}(\vec{k}) = \mathcal{H}(\vec{k} + \vec{G})$, and therefore, at the TRIM points Eq. (1.37) becomes

$$\Theta\mathcal{H}(\vec{\Gamma}_i)\Theta^{-1} = \mathcal{H}(\vec{\Gamma}_i). \tag{1.38}$$

This means that at these points the eigenstates of a time-reversal invariant Hamiltonian are at least two-fold degenerate.

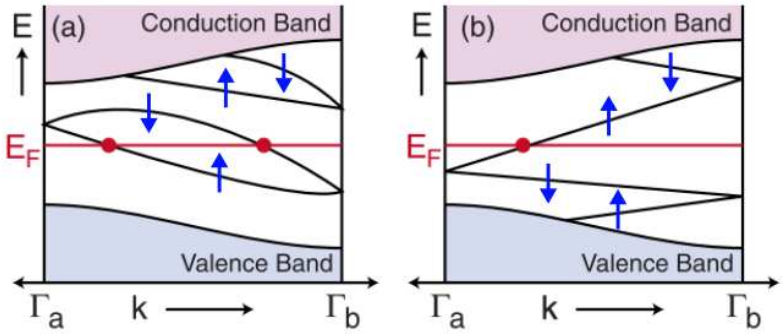

Figure 1.9: The two possible configurations of edge-states in a 2D time-reversal invariant Hamiltonian. At each degenerate point, the two crossing bands are related by the Kramer's theorem, and therefore, have opposite spin orientations (blue arrows). (a) The degenerate end states connect pairwise and the edge-states intersect the Fermi level an even number of times. In this case they are not robust and can be displaced out of the bulk band gap by an adiabatic deformation on the energy spectrum [106, 107]. (b) The degenerate end states "switch partners", so that the edge-states intersect the Fermi level an odd number of times. In this case the edge-states are robust and protected by TRS, constituting a TI. Adapted from Ref. [107].

The existence or nonexistence of states bound to the edge depends on details of the Hamiltonian. If they are present, however, there are two possibles scenarios in which they can appear. Consider a projection of the band structure onto the k_x direction. As a result of the Kramers' theorem, any edge-states must come in pairs, which in turn must be degenerate at $k_x = \Gamma_a$ and $k_x = \Gamma_b$ (the only two TRIM in this projected BZ). Since the two crossing bands are related by the Kramers' theorem, they necessarily have opposite spin orientations. Fig. 1.9 shows the two possible ways in which the states at $k_x = \Gamma_a$ and $k_x = \Gamma_b$ can connect. In Fig. 1.9(a), they connect pairwise, so that the bands intersect

$\mathcal{H}(\vec{k})u_{n,\vec{k}}(\vec{r}) = E_n(\vec{k})u_{n,\vec{k}}(\vec{r})$, where $\mathcal{H}(\vec{k}) = e^{-i\vec{k}\cdot\vec{r}}\mathcal{H}(\vec{r})e^{i\vec{k}\cdot\vec{r}}$ is sometimes called the "Bloch Hamiltonian" [117, 118].

the Fermi level necessarily an even number of times. In this case, the edge-states can be pushed out of the bulk energy gap even by an adiabatic transformation on the energy spectrum [106, 107]. If the Fermi level does not cross any energy level, the edges become insulating and electron transport cannot take place in the material. Another possible way for these states to connect is to "switch partners" at the time-reversal invariant momentum points, as shown in Fig. 1.9(b). In this case, the bands intersect the Fermi level an odd number of times, and the edge-states cannot be eliminated unless the bulk band gap is closed somehow [107]. Therefore, the edge-states in the topological phase are said to be protected by TRS.

Overall, the bulk is insulating in the QSHE but the boundaries of the material behave as a conductor. These counter-propagating metallic states present spin-momentum locking, are protected by time reversal symmetry and cannot be easily destroyed by perturbations in the material, neither by mechanical deformation nor addition of non-magnetic impurities [106–108]. Fig. 1.9(b) illustrates the spin-momentum locking feature, where bands with positive or negative slopes have opposite spin orientations. Due to this intrinsic topological protection, QSHE systems were named (2D) topological insulators (TI's).

The topological invariant for the 2D TI can be defined in several different ways. One approach is to define the unitary matrix element of the time reversal operator between states with time-reversal conjugate momenta $\vec{k}$ and $-\vec{k}$ [106, 107, 119]

$$w_{mn}(\vec{k}) = \left\langle u_m(\vec{k})|\Theta|u_n(-\vec{k})\right\rangle . \tag{1.39}$$

Notice that at the TRIM, $w(\vec{k} = \vec{\Gamma}_i)$ is antisymmetric, which allow us to define the following quantity

$$\delta_i = \frac{\sqrt{\det\left[w\left(\vec{\Gamma}_i\right)\right]}}{\mathrm{Pf}\left[w\left(\vec{\Gamma}_i\right)\right]}, \tag{1.40}$$

where Pf stands for the Pfaffian of an antisymmetric matrix. As $\mathrm{Pf}\left[w\left(\vec{\Gamma}_i\right)\right]^2 = \det\left[w\left(\vec{\Gamma}_i\right)\right]$, we have $\delta_i = \pm 1$. Considering the four TRIM in the 2D bulk BZ, a $\mathbb{Z}_2$ topological invariant ν_{2D} can be defined by [119]

$$(-1)^{\nu_{2D}} = \prod_{i=1}^{4} \delta_i, \tag{1.41}$$

where $i = 1, 2, 3, 4$ labels the TRIMs. The index ν_{2D} determines in which way the Kramers' pairs of edge-states are connected, as discussed before. If $(-1)^{\nu_{2D}} = +1$, the system is a trivial insulator. On the other hand, $(-1)^{\nu_{2D}} = -1$ implies that the Kramers' pairs switch partners at the TRIM, and the system is a TI. It is evident that the topological invariant is only defined modulo 2. Therefore,

$$\nu_{2D} = 0, 1 \bmod 2, \tag{1.42}$$

with 0 for trivial insulators and 1 for TI's.

3D topological insulators

A natural question that arose with the discovery of the QSHE is if there could be a generalization of the TI phase from two to three dimensions. The answer to this question came in 2006, from three independent research groups [107]. L. Fu et. al. [120], J. Moore and L. Balents (which coined the term "topological insulator") [121] and R. Roy [122] found out that the strong spin-orbit interaction in some three-dimensional materials can result in topological order, as a natural generalization of the QSHE [107]. The electronic structure of 3D TI's features very similar characteristics to those of their 2D analogues. The bulk band structure is characterized by an energy gap separating the valence and conduction bands, while the strong SOC brings about metallic surface states described by a single gapless Dirac cone [107, 123]. Just as the helical states in 2D TI's, the gapless surface states in 3D TI's are also protected by TRS and exhibit the remarkable spin-momentum locking. In this case, however, electrons are free to move in any direction along the surface, as long as spin and momentum are perpendicular and both lies tangent to the surface (Fig. 1.10) [106–108, 120, 123–126]. Another important distinction between 2D and 3D TI's is that, although the spin-momentum locking in 3D TI's also prevents against backscattering between states with $\vec{k}$ and $-\vec{k}$, the existence of pairs of states with non-collinear momenta allows for small angle scattering in the TI metallic surface [127, 128].

In 2007, several specific materials were predicted to be 3D TI's, including the $Bi_{1-x}Sb_x$ alloy, as well as α-Sn and HgTe under uniaxial strain [130]. The first experimental realization was accomplished with $Bi_{1-x}Sb_x$ in the following year [124]. In 2009, Bi_2Te_3, Sb_2Te_3 [131] and Bi_2Se_3 [131, 132] were also predicted to be TI's. Shortly after,

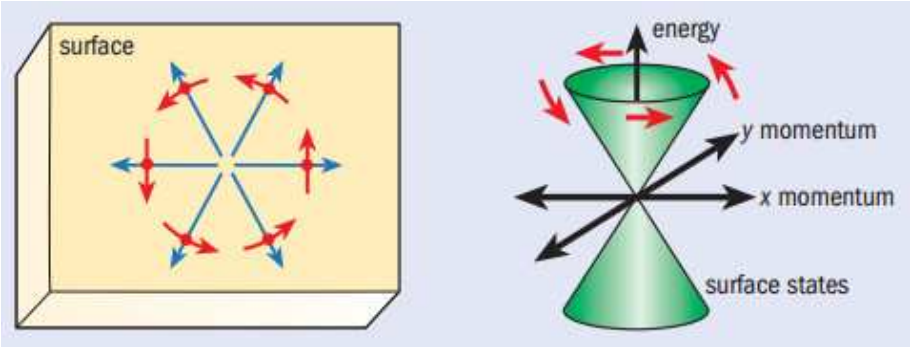

Figure 1.10: Illustration of electrons propagating in the surface of a 3D TI. Due to spin-momentum locking, the spin and momentum of the electrons are necessarily perpendicular to each other. The helicity of each band is given by the spin texture of the surface states, being left-handed for a clockwise rotation around the Dirac point and right-handed if the rotation is counter-clockwise (as the conduction band in this figure) [108, 129]. Adapted from Ref. [108].

angle-resolved photoemission spectroscopy (ARPES) measurements ensured their experimental confirmation, along with the observation of their surface states in the shape of a single Dirac cone (Fig. 1.11) [85, 132, 133]. Broad reviews with many other features of both 2D and 3D TI's can be found in Refs. [106, 107, 125, 126].

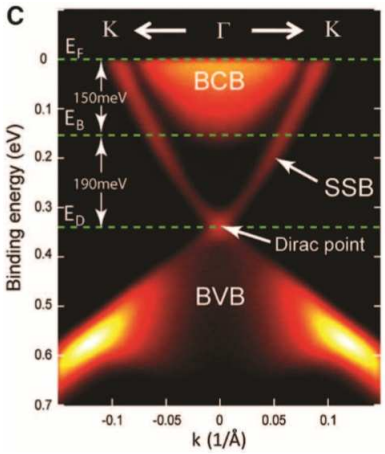

Figure 1.11: Angle-resolved photoemission spectroscopy (ARPES) measurements for Bi_2Se_3, evidencing the Dirac cone describing the surface states between the conduction and valence bands of the bulk. Adapted from Ref. [134].

A low-energy effective Hamiltonian for 3D TI's can be obtained from $\vec{k} \cdot \vec{p}$ perturbation theory by considering the symmetries of the material. Bi_2Se_3, Bi_2Te_3 and Sb_2Te_3 [131], for example, share the same rhombohedral crystal structure with five atoms per unit cell. For these materials, the important symmetries are TRS, three-fold rotation symmetry about the z axis and inversion symmetry. By requiring these symmetries and keeping

only the terms up to quadratic order in $\vec{k}$, one obtains the generic four-bands Hamiltonian valid near the Γ point of the BZ (known as the 3D BHZ model) [106, 129, 131, 135]:

$$H(\vec{k}) = \epsilon_0(\vec{k})I_{4\times4} + \begin{bmatrix} \mathcal{M}(\vec{k}) & A_1k_z & 0 & A_2k_- \\ A_1k_x & -\mathcal{M}(\vec{k}) & A_2k_- & 0 \\ 0 & A_2k_+ & \mathcal{M}(\vec{k}) & -A_1k_z \\ A_2k_+ & 0 & -A_1k_z & -\mathcal{M}(\vec{k}) \end{bmatrix}, \tag{1.43}$$

where $k_\pm = k_x \pm ik_y$, $\epsilon_0(\vec{k}) = C + D_1k_z^2 + D_2k_\perp^2$, $\mathcal{M}(\vec{k}) = M - B_1k_z^2 - B_2k_\perp^2$ and $k^2 = k_x^2 + k_y^2$. The parameters can be obtained by fitting the energy spectrum of the effective Hamiltonian with that of *ab-initio* calculations, for each specific compound [129, 131].

In analogy to 2D TI's, projecting the bulk Hamiltonian [Eq. (1.43)] onto the surface states leads to the surface effective Dirac model [106, 129, 131, 135]:

$$H_D = \pm\hbar v_F \hat{z} \cdot (\vec{k} \times \vec{\sigma}), \tag{1.44}$$

where the Pauli matrix, $\vec{\sigma} = (\sigma_x, \sigma_y, \sigma_z)$, is proportional to the physical spin. The helicity of the spin-texture ($+/-$ sign; see Fig. 1.10) depends on material properties such as the atomic SOC, and is determined by the sign of the parameter A_1/B_1 [106, 129].

The BZ of a system with simple cubic lattice has eight distinct TRIM points, which can be expressed in terms of the primitive reciprocal lattice vectors as $\Gamma_{i=(n_1n_2n_3)} = \left(n_1\vec{b}_1 + n_2\vec{b}_2 + n_3\vec{b}_3\right)/2$, with $n_j = 0, 1$. The 2D BZ of a surface perpendicular to a reciprocal lattice vector, $\vec{G}$, has four TRIM which are projections of bulk TRIM pairs differing by $\vec{G}/2$. The energy spectrum of such surface BZ is characterized by 2D Dirac points at these TRIM. The surface band structure along any path connecting two distinct Dirac points resembles one of the situations in Fig. 1.9, intersecting the Fermi level an odd or even number of times depending on the Kramers' pairs "switching partners" or being connected pairwise, respectively [120].

It turns out that, for the eight TRIM in 3D insulators there are 16 invariant configurations for the quantity δ_i in Eq. (1.40), which can be distinguished by 4 $\mathbb{Z}_2$ indices: $\nu_0; (\nu_1\nu_2\nu_3)$, defined by [120]

$$(-1)^{\nu_0} = \prod_{n_j=0,1} \delta_{n_1n_2n_3}, \tag{1.45}$$

$$(-1)^{\nu_{i=1,2,3}} = \prod_{n_{j\neq i}=0,1;n_i=1} \delta_{n_1 n_2 n_3} \tag{1.46}$$

There are two classes of phases depending on the parity of the topological indices defined above. For $\nu_0 = 0$, the phases can be trivial, if $\nu_i = 0$ for $i = 1, 2, 3$, or "weak TI's", if $\nu_i = 1$ for at least one of the other indices. The weak TI phase can be interpreted as a stack of 2D QSH state layers, so that surfaces perpendicular to the stacking direction are insulating, but the remaining ones are metallic. An important feature of the surface states in weak TI's is that they require translational symmetry to be topologically robust. In fact, if the associated translational symmetry is broken, even a small perturbation can open a gap in these surface states, making the system topologically equivalent to a trivial insulator [107, 120]. The $\nu_0 = 1$ phases are more robust, and all of them fall into the classification of "strong TI's". In this case the surface states are described by a single Dirac cone [Eq. (1.44)], defining a two-dimensional "topological metal". The Kramers' theorem requires that states at momenta $\vec{k}$ and $-\vec{k}$ have opposite spin. Therefore, the spin rotates by 2π as $\vec{k}$ circles around a Dirac point (Fig. 1.10), so that the electron acquires a non-trivial Berry phase of π [107, 120]. As the surface states of a strong TI are topologically protected by TRS, their stability is very robust to non-magnetic perturbations, such as mechanical deformations or chemical doping. In fact, the surface states cannot be localized even for strong disorder, as long as it does not close the bulk energy gap [107, 136].

The physics of the surface states becomes very interesting if one breaks the TRS protecting their topology. This can be achieved by coating the TI surface with a thin FM layer of magnetization perpendicular to the surface, for example. Such a perturbation opens a gap in the Dirac cone describing the energy spectrum of the surface states, leading to the topological magneto-electric effect (TMEE) [106, 107]. Once the TMEE is in order, an external electric (magnetic) field induces both polarization (magnetization) and magnetization (polarization) on the TI. This effect can be exploited to induce and control electric polarization in a conical TI, which highly depends on its geometry. In fact, wider or narrower aperture angles of the cone lead to opposite polarizations [137]. Other consequences of the TMEE are the topological Faraday and Kerr effects, in which light rays reflected and refracted by the surface experience a rotation of the light polarization, respectively [106,107,125,126]. It has been predicted that the topological Kerr effect gives rise to a residual force perpendicular to the incident plane whenever a light ray interacts

with the surface of a magnetically capped spherical TI bead [138].

Opening a gap in the energy spectrum of the surface states by breaking TRS also leads to the surface half-integer quantum Hall effect, with Hall conductivity given by $\sigma_{xy} = (m_z/|m_z|)e^2/2h$. m_z is the mass term determined by the magnetization of the coating FM layer, in which $m_z > 0$ if the magnetization points outwards and $m_z < 0$ if it points inwards [106, 107]. The Hall conductivity can be calculated with the Kubo Formula from linear-response theory, with the use of current-operator matrix elements between momentum-dependent ground $|0\rangle$ and excited $|n\rangle$ states [139]:

$$\sigma_{xy} = \frac{\hbar}{2\pi^2}\int_{DP} d^2k \sum_{n\neq 0} \frac{\mathrm{Im}(\langle 0|j_x|n\rangle\langle n|j_y|0\rangle)}{(E_n - E_0)^2/\hbar^2}. \tag{1.47}$$

In the absence of interactions or disorder, Eq. (1.47) reduces to:

$$\sigma_{xy} = -\frac{\hbar}{2\pi^2}\int_{DP} d^2k \frac{\mathrm{Im}(\langle 0|j_x|1\rangle\langle 1|j_y|0\rangle)}{(E_1 - E_0)^2/\hbar^2}, \tag{1.48}$$

where $|0\rangle$ and $|1\rangle$ represents the valence and conduction bands of the single-particle state, respectively. Performing the integration, one obtains the Hall conductivity of the half-integer quantum Hall effect for each surface:

$$\sigma_{xy} = \mathrm{sgn}(\mathcal{V})\frac{m_z}{|m_z|}\frac{e^2}{2h} \tag{1.49}$$

where $\mathcal{V}$ represents the sense of the vorticity of the momentum-space valence-band-spinor texture [139].

A very interesting manifestation of the surface quantum Hall effect described above is the possibility of inducing an image magnetic monopole inside a TI. In fact, Qi et. al. [123] have shown that if an electric charge is placed near the surface of a TI hosting the TMEE, the magnetic field generated by the surface Hall current is exactly that produced by a magnetic monopole located inside the TI. Such a magnetic monopole can be seen as a mirror image of the electric charge, with the TI surface acting as the mirror plane (see Fig. 1.12). Furthermore, in Ref. [9] [W. H. Campos et al., *Phys. Lett. A* **381**, 417 (2017)], we have shown that the charge of this magnetic monopole can be reversed by exploiting the geometry of the TI surface, namely, under a semi-spherical cavity. Also in Ref. [9], we have proposed a setup to produce anti-parallel Hall currents of reversible flow on the surface of a semi-cylindrical cavity in a TI. In Chapter 5 we discuss these results

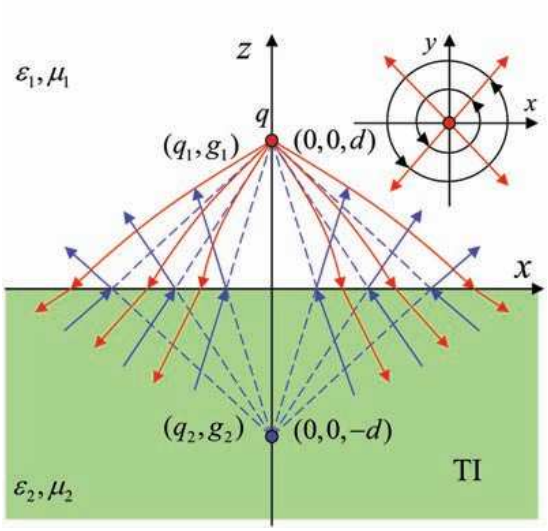

Figure 1.12: Induction of an image magnetic monopole inside the bulk of a TI. Whenever an electric charge is placed near the surface of a TI hosting the TMEE, the magnetic field generated by the Hall current is the same as that produced by an image magnetic monopole located inside the TI. Adapted from Ref. [123].

in more detail.

It is worth mentioning that the discovery of TI's attracted much attention from the condensed matter community and motivated an intense search for new topological phases of matter. Nowadays TI's belong to a very active area of condensed matter physics that studies a wide range of topological phenomena, such as topological superconductors with localized Majorana states [140–142], Weyl and Dirac semimetals [143] and even analogues in photonics [144–146] and acoustic [147, 148] physics. These materials have several intriguing properties closed related to the geometric Berry phase of the electron states. Due to spin-momentum locking, TI's constitute an excellent platform for the realization spin Hall effect (SHE), which is among the most important mechanisms in spintronics. The SHE enforces electrons with opposite spin configurations to flow in opposite directions, allowing for the conversion of spin current into electric current (spin-to-charge conversion) and vice-versa [149]. Therefore, TI's are quoted as both spin current generators and detectors for spintronics applications. Such conversion mechanisms are very important, because spin currents cannot be detected directly and need to be converted into charge currents to be measured experimentally [150].

1.2.3 Topological crystalline insulators

We have seen that TI's have insulating bulk that host metallic boundary states. A more precise definition of an insulating topological phase of matter asserts that the many-body ground state of its Hamiltonian cannot be adiabatically connected to the atomic limit corresponding to a trivial insulator, i.e. with vanishing hopping between the sites of the lattice. This definition can be further extended by requiring that a certain symmetry must be preserved during the adiabatic interpolation. An insulating topological phase in the latter sense is said to be protected by the corresponding symmetry, so that a perturbation which respects such symmetry cannot destroy the topological phase [151]. In TI's, TRS is the responsible for such protection, which makes them robust against non-magnetic perturbations [106, 107]. It turns out that time reversal is not the only symmetry capable of protecting insulating topological states of matter with bulk-boundary correspondence. In fact, it has recently been proposed a number of systems in which topology is protected by non-local spatial symmetries, like mirror and rotation, or even the combination of spatial and time reversal symmetries (for a more detailed discussion and definition of non-local symmetries in this context, see Ref. [152]). These "topological crystalline insulators" (TCI's) present gapped bulk band structure and gapless modes at the boundaries that respect the corresponding symmetries. Furthermore, their band structures are characterized by new topological invariants, which remain unchanged as long as the bulk energy gap does not close [151, 153, 154].

As crystal symmetries can be broken by boundaries (unlike TRS), depending on the termination, often the very same TCI sample has some topologically protected metallic surfaces coexisting with insulating or topologically fragile surfaces oriented in different directions. Consider, for example, a 3D crystal structure with tetragonal lattice and unit cell of two inequivalent atoms A and B [Fig. 1.13(a)]. This system is invariant under both TRS ($\mathcal{T}$) and four-fold rotation (C_{4z}) around the z-axis (but not around the x and y axes). A minimal model Hamiltonian neglecting spin-orbit interactions is developed in Ref. [153]. Here, we are interested in the symmetry-related topological properties of the system, which do not require the explicit form of the Hamiltonian to be discussed. The authors have shown that this system has a gapped bulk band structure [see Fig. 1.14(a)], but only top and bottom surfaces hosting topologically protected gapless states. The reason for this is that, as discussed below, the topology is protected by the combination

of $\mathcal{T}$ and C_{4z} symmetries. The latter is preserved for surfaces perpendicular to the z-axis, but broken by surfaces oriented in other directions.

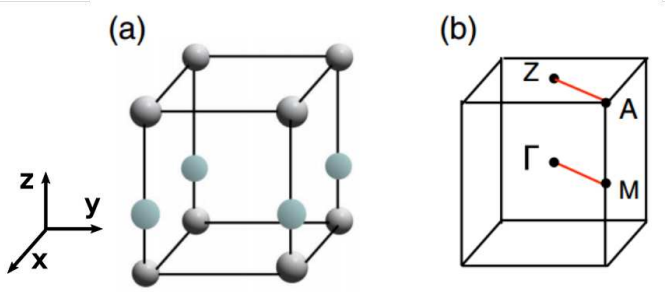

Figure 1.13: Topological crystalline insulator protected by C_{4z} and $\mathcal{T}$ symmetries. (a) Tetragonal crystal structure with two inequivalent atoms in its unit cell. (b) 3D BZ of the model, emphasizing straight lines connecting two adjacent high symmetry points Γ, M, A and Z. Adapted from Ref. [153].

To understand how the topological protection is achieved, notice that the Bloch Hamiltonian of the system, $\mathcal{H}(\vec{k})$, satisfies [153]

$$\begin{aligned} \Theta\mathcal{H}(k_x,k_y,k_z)\Theta^{-1} &= \mathcal{H}(-k_x,-k_y,-k_z) \\ C_{4z}\mathcal{H}(k_x,k_y,k_z)C_{4z}^{-1} &= \mathcal{H}(-k_y,k_x,k_z), \end{aligned} \tag{1.50}$$

where $\vec{k}$ is the crystal momentum, Θ is the time reversal operator for spinless electrons ($\Theta^2 = 1$) and C_{4z} is the operator of four-fold rotations around the z-axis. There are four high symmetry points, $\vec{k}_i = \{\Gamma = (0,0,0), M = (\pi,\pi,0), A = (\pi,\pi,\pi), Z = (0,0,\pi)\}$ [Fig. 1.13(b)], in which $[\mathcal{H}(\vec{k}_i), C_{4z}] = 0$, so that the energy bands are eigenstates of C_{4z} with possible eigenvalues 1, -1, i and $-i$. At these points, it can be shown that energy bands with $\pm i$ eigenvalues are guaranteed to be degenerate.

Considering a slab geometry with periodic boundary conditions along x and y, one can solve the Hamiltonian of this system to obtain the energy spectrum of the states localized along the (001) surface [Fig. 1.14(b)]. These surface states are double degenerate at the $\overline{\Gamma} = (0,0)$ and $\overline{M} = (\pi,\pi)$ high symmetry points of the surface BZ. Just as for TI's, there are two different possibilities for connecting these two degenerate end states. If the states "switch partners" at the high symmetry points, there is an odd number of band crossings at the Fermi energy (considered to be inside the bulk band gap) and the surface states are topologically protected. If there is an even number of band crossings, any possible surface state is fragile, so that changing the surface potential can push them

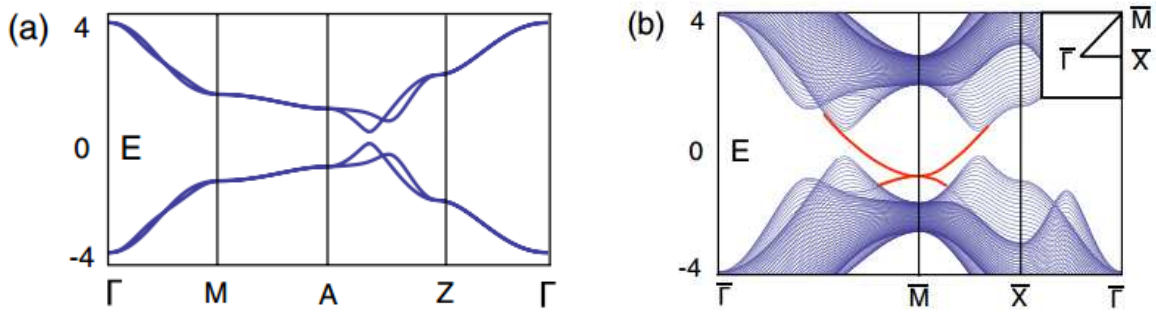

Figure 1.14: (a) Bulk band structure of the TCI protected by C_{4z} and $\mathcal{T}$ symmetries. (b) Energy band structure of the TCI in a slab geometry with periodic boundary conditions along x and y, evidencing the gapless boundary states localized along the (001) surface (red curves). Adapted from Ref. [153].

out. For the above example, a new $\mathbb{Z}_2$ topological invariant, ν_0, that reflects the band connectivity can be defined in order to characterize the system's topology [153]:

$$(-1)^{\nu_0} = (-1)^{\nu_{\Gamma M}}(-1)^{\nu_{AZ}}, \tag{1.51}$$

$$(-1)^{\nu_{\vec{k}_1\vec{k}_2}} = \exp\left(i\int_{\vec{k}_1}^{\vec{k}_2}\vec{\mathcal{A}}(\vec{k})\cdot d\vec{k}\right)\frac{\mathrm{Pf}\left[w\left(\vec{k}_2\right)\right]}{\mathrm{Pf}\left[w\left(\vec{k}_1\right)\right]}, \tag{1.52}$$

where $\vec{\mathcal{A}}(\vec{k}) \equiv -i\sum_j \left\langle u_j(\vec{k})\left|\vec{\nabla}_{\vec{k}}\right|u_j(\vec{k})\right\rangle$ is the Berry connection. The elements of the matrix w are defined by $w_{mn}\left(\vec{k}_i\right) \equiv \left\langle u_m\left(\vec{k}_i\right)|C_{4z}\Theta|u_n\left(\vec{k}_i\right)\right\rangle$. It can be shown that w is antisymmetric as a result of the relations $\left[H\left(\vec{k}_i\right), C_{4z}\Theta\right] = 0$ and $(C_{4z}\Theta)^2 = -1$. Pf stands for the Pfaffian. The integral in Eq. (1.52) can be calculated along any arbitrary line connecting $\vec{k}_1$ and $\vec{k}_2$, as long as it lies in the 2D plane perpendicular to the z axis and which contains both $\vec{k}_1$ and $\vec{k}_2$ [153].

The $\mathbb{Z}_2$ topological invariant defined above characterizes the band structure of the system: $\nu_0 = 0$ corresponds to a trivial phase adiabatically connected to an atomic insulator and $\nu_0 = 1$ corresponds to a TCI with gapless surface states on the (001) surface. This TCI does not have gapless surface states in other surface terminations which break C_{4z} symmetry. Naturally, perturbations that break either C_{4z} or $\mathcal{T}$ can open up an energy gap and destroy the protected surface states, while moderate perturbations that preserve the symmetries protecting a TCI cannot destroy its topological phase [151].

Its is worth emphasizing that TCI's do not require spin-orbit interactions to exist, allowing for surface states with quadratic energy dispersion [see Fig. 1.14(b)], in contrast to the Dirac materials with linear dispersion originating from strong SOC [153]. In 2012,

the semicondutor SnTe was the first material predicted [155] and experimentally confirmed [156] to be a TCI, which was shown to have topologically protected metallic surface states with an even number of Dirac cones on the {001}, {110} and {111} high-symmetry crystal surfaces. Shortly after, both $Pb_{1-x}Sn_xSe$ and $Pb_{1-x}Sn_xTe$ were also observed to assume TCI phases [157, 158].

1.2.4 Higher order topological insulators

The concept of TCI's can be extended to include a recently discovered class of materials known as higher order topological insulators (HOTI's) [159–161]. These materials also have metallic boundary states with at least one spatial symmetry involved on the topological protection. The main difference dwell on the dimension of these boundary states when compared to the dimension of the system. Usual topological materials in 2D present metallic boundaries in 1D, like the QHE and the QSHE. 3D TI's host metallic surfaces, that is, topological states in a 2D boundary. The HOTI's represent an interesting generalization of the "bulk-boundary" correspondence. The order of a HOTI is given by the codimension of the boundary state in a given system, which is defined as the difference between the dimension of the system and the dimension of the metallic boundary. A 2D *second order* TI, for example, does not have gapless metallic edge-states, but "corner states" at the vertices of the sample, since they have codimension 2. In 3D, a *second order* TI host "hinge states" (codimension 2), while a *third order* TI present "corner states" (codimension 3) [160, 162–167].

Although the discovery of these materials is very recent, they have attracted a tremendous attention from the condensed matter community and the literature on the subject is rapidly growing. Different combinations of spatial symmetries, along with TRS, can be responsible for the protection of higher order topology. A few examples are reflection-symmetric second order TI's (SOTI's) [168], chiral and helical SOTI's protected by the combination of time-reversal with four-fold rotation symmetry and time-reversal plus mirror symmetries, respectively [160]. Furthermore, inversion-protected HOTI's [169], hexagonal SOTI's with $\mathbb{Z}_3$ topological index protected by inversion time-reversal symmetry ($I\mathcal{T}$) and rotoinversion symmetry (IC_6) [170] have also been proposed. In Ref. [171], it was shown that an external magnetic field can be used to induce a topological switch between SOTI's and TCI's, where both phases are protected by mirror and inversion

symmetries.

Real materials predicted to be HOTI's include phosphorene in the rhombus structure [164], Sm-doped Bi_2Se_3 [172] and even the prominent twisted bilayer graphene with large angles [173]. Ref. [161] also present some material candidates in 2D systems with significant spin-orbit coupling. Experimental observations have confirmed that bismuth, contrary to the former belief of trivial topology, is a HOTI with hinge modes protected by TRS, three-fold rotation and inversion symmetry [174].

Charged modes at the boundaries of a finite system are usually associated with the polarization of electric dipole moment in the bulk. In Ref. [159], Benalcazar et. al. have suggested two and three-dimensional generalizations of the Su-Schrieffer-Heeger (SSH) model and have shown that they lead to HOTI phases with gapless, topological corner excitations corresponding to quantized higher electric multipole moments. The topologically protected quadrupole moment in 2D and octupole moment in 3D, along with edge polarizations, are all boundary manifestations of the bulk, reinforcing the generalization of bulk-boundary correspondence for HOTI's (see Figure 1.15). The energy spectrum of surfaces and hinges are gapped, but the corner states carry fractional charges that are quantized to be $\pm e/2$ in the presence of certain symmetries, exhibiting fractionalization at the boundary of the boundary.

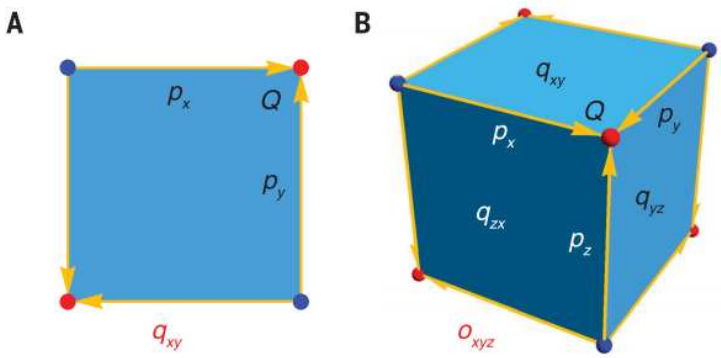

Figure 1.15: Illustration of the corner states (Q), along with edge polarizations ($\vec{p} = (p_x, p_y, p_z)$), for the (a) 2D electric quadrupole insulator and (b) 3D electric octupole insulator. $q_{x,y}$ and o_{xyz} represent the quadrupole and octupole moments, respectively. Adapted from Ref. [159].

A toy-model for the electric quadrupole insulator describes spinless electrons on a square lattice with four orbitals per unit cell. The 4-band Bloch Hamiltonian, $\mathcal{H}(\vec{k})$, reads [see tight-binding model representation in Figure 1.16(a)] [159]

$$\mathcal{H}(\vec{k}) = [\gamma + \lambda\cos(k_x)]\,\Gamma_4 + \lambda\sin(k_x)\,\Gamma_3 + [\gamma + \lambda\cos(k_y)]\,\Gamma_2 + \lambda\sin(k_y)\,\Gamma_1, \qquad (1.53)$$

where $\Gamma_0 = \tau_3\omega_0$, $\Gamma_l = -\tau_2\omega_l$ and $\Gamma_4 = \tau_1\omega_0$ for $l = 1, 2$ and 3. Here, τ and ω are Pauli matrices representing pseudospin degrees of freedom within a unit cell. γ and λ are the strengths of the hopping terms between neighboring atoms within a unit cell and between adjacent unit cells, respectively. Furthermore, the model has bond dimerization in both x and y directions, as shown in Fig. 1.16(a).

Consider a finite system with open boundary conditions along both x and y directions. Solving the eigenvalue problem for such a system with the Hamiltonian defined in Eq. (1.53) gives the energy spectrum for the corner states. Figure 1.16(b) shows the energy spectrum of this system with mid-gap corner states highlighted in red. For $|\gamma/\lambda| > 1$, the whole system is insulating and it has trivial topology. A topological phase transition occurs for $|\gamma/\lambda| = 1$, in which the bulk energy gap closes and corner states appear at the vertices of the sample. The corner states remain robust for all points in the range $|\gamma/\lambda| < 1$, constituting the quantized electric quadrupole phase. Figure 1.16(c) shows a plot of the electronic charge density in the nontrivial phase.

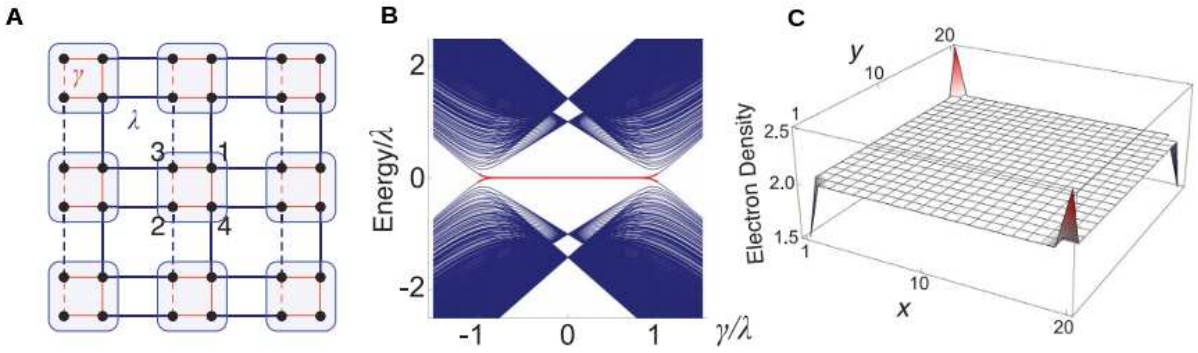

Figure 1.16: Electronic properties of the quantized electric quadrupole insulator. (a) Tight binding representation of [Eq. (1.53)], in which solid (dashed) lines represent positive (negative) hopping terms, with blue (red) color for the λ (γ) parameter. (b) Quantized energy spectrum of the finite system with square geometry as a function of the hopping parameters. The energy eigenvalues of the corner-localized states are highlighted in red. (c) Electron density for a mid-gap state. Adapted from Ref. [159].

There are three spatial symmetries relevant to the topological protection of the quantized electric multipole moment. Inversion symmetry, $\mathcal{I} : (x, y) \to (-x, -y)$, ensures

the locking of the vanishing bulk polarization, while mirror symmetries along x, $M_x : x \to -x$, and y, $M_y : y \to -y$, ensure the quantization of edge polarizations, and consequently, the quantization of the electric quadrupole moment [159]. Clearly, the only high-symmetry points of the BZ invariant under the three symmetries above are $\Gamma = (0, 0)$ and $M = (\pi, \pi)$, which reflects the localization of the metallic states at the corners.

A topological invariant for this system can be obtained via the "nested" Wilson loops, which resembles a "Berry phase of a Berry phase". More specifically, let us define

$$[F_{x,k}]^{mn} = \langle u^m_{k+\Delta k_x} | u^n_k \rangle, \tag{1.54}$$

where k_x is the crystal momentum along x, $\Delta k_x = (2\pi/N_x, 0)$ (N_x is the number of lattice sites along x) and $|u^n_k\rangle$ is the Bloch state for the n occupied energy band. The Wilson loop along x direction can be defined by

$$\mathcal{W}_{x,k} \equiv F_{x,k+N_x\Delta k_x} ... F_{x,k+\Delta k_x} F_{x,k}. \tag{1.55}$$

With full periodic boundary conditions, the Wilson loop for the model above with two occupied energy bands diagonalizes as

$$\mathcal{W}_{x,k} = \sum_{j=\pm} \left|\nu^j_{x,k}\right\rangle e^{2\pi i \nu^j_x(k_y)} \left\langle \nu^j_{x,k}\right|, \tag{1.56}$$

where the eigenstates $\left|\nu^j_{x,k}\right\rangle$ have components $[\nu^j_{x,k}]^n$, $n = 1, 2$. The spectra $\nu^\pm_x(k_y)$ are named Wannier bands, which are used to define the Wannier band subspaces

$$\left|w^\pm_{x,k}\right\rangle = \sum_{n=1,2} |u^n_k\rangle \left[\nu^\pm_{x,k}\right]^n. \tag{1.57}$$

In the thermodynamic limit, the polarization of the Wannier band is given by

$$p_y^{\nu^\pm_x} = -\frac{1}{(2\pi)^2} \int_{BZ} \tilde{\mathcal{A}}^\pm_{y,k} d^2k = \begin{cases} 0 & \frac{|\gamma|}{|\lambda|} > 1 \\ 1/2 & \frac{|\gamma|}{|\lambda|} < 1 \end{cases}, \tag{1.58}$$

where

$$\tilde{\mathcal{A}}^\pm_{y,k} = -i \left\langle w^\pm_{x,k} \left| \partial_{k_y} \right| w^\pm_{x,k} \right\rangle \tag{1.59}$$

is the Berry potential over the Wannier band $\nu^\pm_x$.

Finally, the quadrupole invariant q_{xy} can be defined as [159]

$$q_{xy} = 2ep_x^{\nu_y^{\pm}} p_y^{\nu_x^{\pm}} = 0 \text{ or } e/2. \tag{1.60}$$

In analogy to the previously discussed topological phases, perturbations preserving the $\mathcal{I}$, M_x and M_y symmetries cannot eliminate the corner states present in this system. An interesting feature of the Benalcazar's model is that a transition from the quadrupole phase to a phase with vanishing quadrupole moment, but quantized edge polarizations, is not signaled by a closing of the 2D bulk energy gap. Instead, the transition is characterized by a gap closing in the energy spectrum of the 1D Hamiltonian describing the edge-states of the system.

As it is recurrent in topological physics, analogues of the quantized electric multipole insulator have been observed in very different areas of research, such as the phononic quadrupole insulator in a mechanical metamaterial [175], the topological corner modes in a topolectrical-circuit [176] and the quantized microwave quadrupole insulator with topologically protected corner states [177]

In Section 6.3, we discuss our preliminary results in a project initiated in collaboration with Dr. Libor Šmejkal and Prof. Jairo Sinova (Johannes Gutenberg Universität Mainz, Germany) during my Ph.D. "Sandwich" scholarship abroad. We have been working on an extension of the model described above, in which we add spin degrees of freedom and consider both FM and AF configurations for the underlying lattice.

1.2.5 Topological antiferromagnetic spintronics

The term "spintronics" refers to the area of condensed matter physics devoted to study the properties and active manipulation of spin (or magnetic, in general) degrees of freedom in order to process and store information. Magnetic devices are considered as a viable alternative to the usual charge-based ones, for they are robust against charge perturbations such as ionizing radiation, which can lead to data loss. It has led to valuable insights, both for technological applications and fundamental physics, having already started to be implemented in modern technologies [149, 150, 178–182]. The products of spintronics play an important role when it comes to the storage of information. The tunneling magnetoresistance (TMR), giant magnetoresistance (GMR) and electrical spin injection allowed for the development of modern hard drives [150]. Furthermore,

a brand new generation of magnetic random access memory (MRAM) devices utilizing spin-transfer torques (STT) is already in production routes [149, 183, 184]. The mechanism of spin-orbit torque (SOT) will lead to even more efficient non-volatile MRAM's, for they require less electric current to operate and would generate even less heat in the process [149,183]. Besides applications in magnetic storage and MRAM's, there have been several proposals for using spin degrees of freedom in magneto-logic gates [150, 185–188].

It is evident that for spintronics it is necessary to explore materials with strong magnetic properties. Most studies consider FM materials, for they are easier to manipulate and their properties better understood. However, FM materials are sensitive to external magnetic perturbations or even internal fields within the circuitry. This can lead to undesired reorientation of the magnetic moments carrying information. In this regard, AF materials have attracted much attention lately. There are several advantages of using AF materials for magnetic devices. Due to the zero net magnetization resulting from opposite orientation of adjacent magnet moments, these materials experience vanishing torques generated by external magnetic fields, making them robust against both charge and magnetic perturbations. For the same reason, AF's also keep the stored data safe against external magnetic probes, since they do not produce external magnetic fields. Besides that, they allow for ultrafast spin dynamics, and there is a broad range of known materials with AF order at room temperature [189].

Obviously, in order to store and manipulate information in AF's it is necessary some mechanism capable of controlling their magnetic ordering. Several types of materials have been considered as promising for AF spintronics, but probably the most intriguing of them are the Dirac materials. They are termed like this because their low-energy physics is described by the massless Dirac equation, which leads to a linear energy-momentum spectrum. In these materials, the relativistic spin-orbit coupling (SOC) plays an important role, and crystal momentum can be coupled to pseud-spin or spin degrees of freedom, as occurs for graphene [190] and for the surface states of TI's, respectively [150, 180]. Graphene constitutes a sheet of carbon atoms arranged in a 2D hexagonal lattice, having two Dirac cones in its energy spectrum. In turn, 3D TI's are materials with gapped bulk band structure and 2D topological metallic surfaces with a single Dirac cone protected by TRS (see Subsection 1.2.2). Some AF materials with SOC present Fermi surfaces whose chirality of the helical spin texture associated to each sublattice are opposite to each other.

A unidirectional electric current is capable of generating spin accumulations of opposite orientations in each sublattice, exerting staggered internal fields whose sign alternates with the periodicity of the AF lattice. As a result, the Néel vector tend to align perpendicularly to the applied current (Fig. 1.17) [189]. In other words, the current-induced torque on each of the magnetic moments adds up instead of canceling each other. These fields couple strongly to the AF order, allowing for electrical switching of the Néel vector direction between different stable configurations [189, 191].

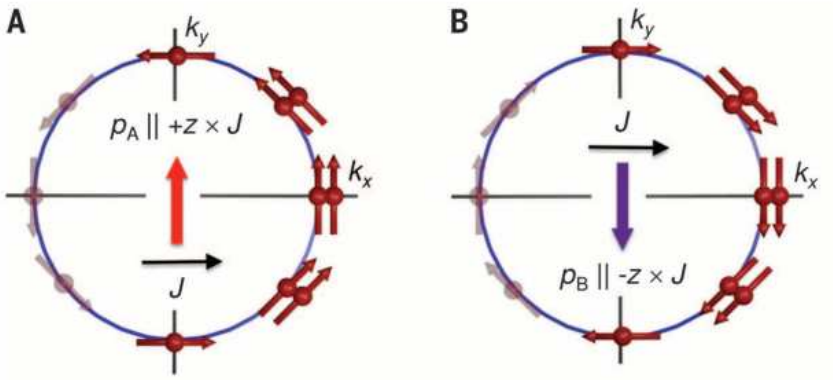

Figure 1.17: Staggered current-induced field in AF CuMnAs. The helical spin texture of the Fermi surface associated to each sublattice (labeled by A and B in the figure) have opposite chirality. The nonequilibrium redistribution of charge carriers under an applied electric current $\vec{J}$ (black arrow) induces an staggered in-plane spin polarization (thick red and purple arrows), allowing for reorientation of the Néel vector. Adapted from Ref. [189].

The manipulation of the Néel vector by electric currents mentioned above was predicted and experimentally confirmed to take place in the tetragonal phase of the AF CuMnAs [189], which can be stabilized by molecular beam epitaxial growth, as recently shown in Ref. [191]. Furthermore, V. Hill et. al. [192] investigated the phase transition from paramagnetic to AF order in this material using neutron diffraction and electrical transport measurements (Fig. 1.18). The observed Néel temperature was considerably high ($T_N = 480$K), making CuMnAs a very promising candidate for room temperature applications in magnetic devices. Besides current-induced torques, AF order can be efficiently manipulated by optical mechanisms such as inertia-driven spin switching, least dissipative impulsive excitation of spins, among others [182, 193]. The possibility of manipulating the Néel vector by light or electric currents is among the main reasons why AF materials have been considered as very suitable candidates for memory applications [192, 194, 195].

Besides the intense research on AF and Dirac materials in spintronics, there is

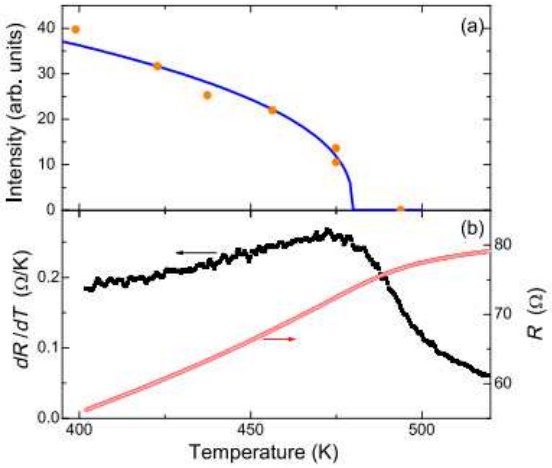

Figure 1.18: Phase transition from paramagnetic to AF order in tetragonal CuMnAs from neutron diffraction and electric transport measurements. (a) Experimental data (orange dots) for the intensity of the magnetic neutron diffraction peak, which is sensitive to the AF order, vs. temperature fitted to a $(T_N - T)^{2\beta}$ power law, leading to a Néel temperature of $T_N = 480$K. (b) Resistivity and its temperature derivative vs. temperature, whose peak signals an increase in the carrier scattering rate due to spin fluctuations near the critical temperature. Adapted from Ref. [192].

an emerging area that explores the interplay between AF spintronics and topological materials in order to achieve even more sophisticated mechanisms. The "topological antiferromagnetic spintronics" is devoted to study new types of phenomena taking place in materials that present both AF and topological order, providing a promising platform for high-performance spintronics. This is a new and very exciting area of research in an early stage, in which many ideas where only addressed theoretically so far. A particularly interesting effect discovered in this context is the topological metal-insulator transition in 3D AF Dirac semimetals. Here, current-induced spin-orbit torques can be used in order to achieve a topological phase transition [196, 197]. The effect is intermediated by reorientation of the Néel vector by the electric current, so that the symmetries necessary for protection of the band crossing can be switched on and off, allowing for easy external control of the topological phase. Fig. 1.19 shows this effect taking place in the tetragonal AF CuMnAs. A generic minimal model can be written considering only the Mn atoms forming a stack of crinkled[3]quasi-2D square lattices, whose Bloch Hamiltonian reads [196, 197]

[3]The term crinkled (used by the authors in Ref. [196]) refers to the appearance of the unit cell constructed over two stacked sublattices connected by the combination of half-primitive cell translations along all the [100], [010] and [001] directions. Such construction gives a "crinkled" aspect to the unit cell, as can be seen in Fig. 1.19(b).

$$H(\vec{k}) = -2t\tau_x \cos\frac{k_x}{2}\cos\frac{k_y}{2} - t'(\cos k_x + \cos k_y) + \\ + \lambda\tau_z(\sigma_y \sin k_x - \sigma_x \sin k_y) + \tau_z J_n \sigma \cdot \vec{n}, \tag{1.61}$$

where t is the first nearest-neighbor hopping (inter-sublattice hopping), t' is the second nearest-neighbor hopping (intrasublattice hopping), λ is the second-neighbor SOC, and J_n is the AF exchange coupling [see Fig. 1.19(b)]. $\vec{k}$ is the crystal momentum, $\vec{n}$ is the Néel vector, and $\vec{\tau}$ and $\vec{\sigma}$ are Pauli matrices describing the crystal sublattice and the spins degrees of freedom, respectively.

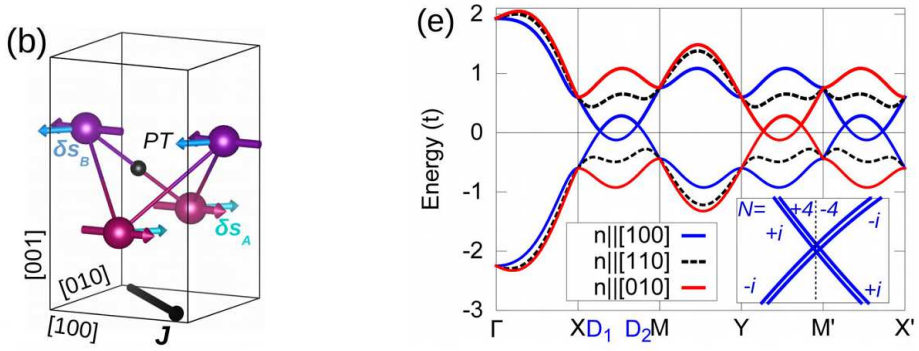

Figure 1.19: Illustration of the topological metal-insulator transition in tetragonal AF CuMnAs. (b) Minimal model with nonsymmorphic glide mirror plane symmetry extracted from CuMnAs. $\delta\vec{s}_{A,B}$ represent the staggered nonequilibrium spin polarizations induced by an electric current $\vec{J}$ to manipulate the Néel vector. (e) Band dispersion for three distinct orientations of the Néel vector, $\vec{n} \parallel [100]$ (solid blue line), $\vec{n} \parallel [110]$ (dashed black line) and $\vec{n} \parallel [010]$ (solid red line). When glide mirror plane symmetry along x or y directions is preserved, the system is a topological AF Dirac semimetal. Breaking such symmetry opens a gap on the entire spectrum, inducing a topological phase transition to a trivial insulator. Adapted from Ref. [196].

Fig. 1.19(e) shows the band dispersion obtained from Eq. (1.61), for three distinct orientations of the Néel vector. When $\vec{n}$ is along the [100] axis, the system is invariant under nonsymmorphic glide mirror plane symmetry along x, $\mathcal{G}_x = \{M_x|\frac{1}{2}00\}$ (combination of mirror symmetry M_x along the (100) plane with the half-primitive cell translation along the [100] axis), and the material is a topological AF Dirac semimetal protected by this symmetry. On the other hand, for $\vec{n}$ along the [110] axis this symmetry is no longer preserved and the entire spectrum is gapped, constituting a trivial insulator. Finally, reorientation of the Néel vector along the [010] axis recovers the glide mirror plane symmetry, now along y, and the system is again a topological AF Dirac semimetal [196]. In Section 6.4 we discuss our preliminary results (also in collaboration with Dr. Libor

Šmejkal and Prof. Jairo Sinova) on a modified version of the model described above, in which we have been investigating the possible existence of edge and/or corner states on ribbon and rectangular finite samples.

In conclusion, the fields of spintronics, topological materials and magnetism constitute very active and exciting areas of research, with many perspectives for near future applications. The new and rapidly growing research in topological AF spintronics combine these three different fields of condensed matter physics and has just started to be appropriately explored. Further examples of topological AF spintronics include the existence of Weyl fermions in antiferromagnets, the anomalous Hall effect in non-collinear antiferromagnets, the topological Hall effect in antiferromagnets and others that can be reviewed in Ref. [197]. New topological materials have been discovered in an unbelievable pace and it is important to examine how their unique properties can be employed to instigate novel technological advances.

PART I

Chapter 2

Topological insulator particles as optically induced oscillators

In this chapter we provide a detailed analysis of the findings described in Ref. [1] [Adapted with permission from (W. H. Campos, J. M. Fonseca, V. E. de Carvalho et. al., "Topological Insulator Particles As Optically Induced Oscillators: Toward Dynamical Force Measurements and Optical Rheology," *ACS Photonics* **5**(3), 741-745 (2018)). Copyright © (2018) American Chemical Society.[1] `http://pubs.acs.org/articlesonrequest/AOR-xSCxJBnD3IYfIgpcicMn`], where we report the first experimental study upon the optical trapping and manipulation of topological insulator (TI) microparticles. We have observed that, by virtue of their unique properties, such particles present a peculiar behavior whenever subjected to a single Gaussian laser beam optical tweezers (OTs): they oscillate in a plane perpendicular to the direction of the laser propagation. In other words, TI particles behave as optically induced oscillators, allowing dynamical measurements with unprecedented simplicity and purely optical control. As discussed in Section 1.1, transparent dielectric particles present low reflection and absorption of light. Therefore, radiometric effects can be neglected and the trapping efficiency is usually high. Metallic particles, otherwise, undergo rapid heating due to light absorption, so that they are scattered almost instantaneously by radiometric forces [66–69]. In this case, the gradient force is small and can be safely neglected. In our experiments, we have observed that the TI particles do not fit in any of these two categories. In fact, they seem to behave like

[1]Copyright credit line obtained along with permission via RightsLink system (link available in the article's website under "Rights and Permissions"; click here to be redirected to the corresponding page).

semi-transparent beads whenever illuminated by light of wavelength $\lambda \sim 1064\,\text{nm}$. As a result, both the gradient and radiometric forces significantly contribute to their dynamics. The former attracts the particles toward the optical axis, while the latter repels them from the optical region. Since the seminal papers by Ashkin and collaborators [10,12], the optical trapping and manipulation of micrometer-sized particles have found applications in many areas, from interface and colloid science to single molecule biophysics [16,34,35]. In addition, improvements have been achieved regarding the use of optical tweezers as a tool for materials science [36–39], and more recently, in the study of solution-phase chemistry [40].

In turn, topological insulators (TI's) are materials with unique properties, whose robust stability is topologically protected by time reversal symmetry. They are known to have insulating (dielectric) bulk, but conducting surface states that support charges flowing without dissipation. In addition, the electromagnetic response of TI's is such that an external electric (and/or magnetic) field induces both magnetization and polarization, the so-called topological magnetoelectric effect. As a direct consequence, whenever light comes onto a TI, reflected and refracted rays experience topological Faraday and Kerr rotations, respectively [106, 107, 125, 126]. Furthermore, it has been recently predicted that the topological Kerr effect gives rise to a residual force perpendicular to the incident plane whenever light is shed onto a magnetically capped spherical topological insulator bead [138]. Such a topological-like force goes around some dozens of femtoNewtons, about the Casimir force scale [55]. Thus, whenever subjected to a highly focused light beam, like those used in optical tweezers, it is expected that a TI particle should experience competing effects coming from the interaction of light with its conducting surface and insulating bulk. We should wonder about the resulting effect of such an interaction to the TI-particle dynamics.

In this work, we conduct an experimental study regarding the optical trapping and manipulation of TI particles. We have observed that these particles present a quite unusual dynamics under a highly focused light beam: they oscillate perpendicularly to the direction of laser propagation. In other words, they behave as optically induced oscillators, making them unique candidates to open an avenue for novel applications of optical manipulation techniques, allowing dynamical measurements with unprecedented simplicity. Actually, rheology of soft matter interfaces and biological membranes, dynam-

ical force measurements in macromolecules and biopolymers may be quoted as some of feasible achievements by using TI-beads as optical oscillators.

2.1 Objectives

Even though our present investigation was initially motivated by the prediction reported in Ref. [138], we did not expect to carry out a direct observation of such a topological-like force, mainly for we have used TI-particles without any magnetic cap, whose field would open an energy gap at the surface states, making topological Kerr effect possible. Therefore, the results reported in this chapter do not confirm such a theoretical prediction (nor do rule it out).

We devote ourselves to evidence and systematically study the behavior of TI microparticles under OTs by conducting a quantitative analysis of their dynamics. Investigating how the position of the particles evolves in time, we are able to obtain their instantaneous velocities and accelerations, which can be used to calculate the forces exerted on the particle during the experiment. We also aim to explain the observed oscillations by referring to present effects previously discussed in the literature, along with the development a comprehensive effective model for the forces involved. Comparison of our model with experimental data is an important component of this work in order to verify its validity and applicability. Additionally, we investigate the dynamic properties of the system, such as the amplitude and period of oscillations, and how they depend on controllable parameters , such as the power of the laser beam, and the particle size. We suggest how the observed oscillations can be useful in practical applications and discuss further improvements to be considered in future investigations.

2.2 Materials and methods

The Bi_2Te_3 and Bi_2Se_3 particles are TI's at room temperature and have been obtained from single crystals by the laser ablation technique. Measurements were made for both composites and they present the same general behavior. However, it is important to say that not all TI particles obtained by laser ablation are satisfactorily spherical. Actually, most of them present an irregular shape. The concentration of nearly spherical particles in deionized water available for our experiments is much higher for Bi_2Te_3 than

for Bi_2Se_3. Consequently, they have presented much better results, with smaller error bars and better defined frequencies of oscillation. In order to be more succinct, in this thesis we present only the results for Bi_2Te_3, even though the oscillatory behavior have been observed for all beads.

2.2.1 Experimental setup

For the optical experiment, we have selected only those particles with a nearly spherical shape, and average diameter between 3 μm and 7 μm. Later, they have been suspended in deionized water and placed in the sample chamber, which consists of an *o-ring* glued in a microscope coverslip. In fact, we have observed that the beads remain suspended around 4 μm above the coverslip surface, before and during the laser incidence. The optical tweezers consist of a 1064 nm ytterbium-doped fiber laser (IPG Photonics) operating in the TEM_{00} mode, mounted on a Nikon Ti-S inverted microscope with a 100× NA 1.4 objective (Fig. 2.1). In all experiments we have used a laser power of 25 mW measured at the objective entrance. The only exception is the one used to obtain the data of Fig. 2.7, in which we investigate the dependence of period and amplitude of oscillation with the laser power.

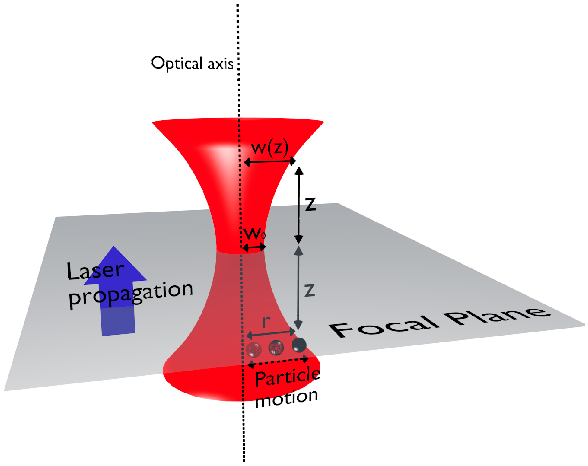

Figure 2.1: Experimental setup yielding the oscillatory dynamics and definition of the coordinate system, along with the relevant parameters. A TI particle is located around $z \sim 10$ μm below the focal plane and it oscillates perpendicularly to the optical axis direction. Adapted from Ref. [1].

2.2.2 Experimental procedure used to obtain the forces

For each TI particle investigated, we film its motion for various oscillating cycles using videomicroscopy. A CCD camera (JAI BM-500GE) was used, allowing us to obtain movies with 15 frames per second and with a resolution of 29 pixels/μm. Some

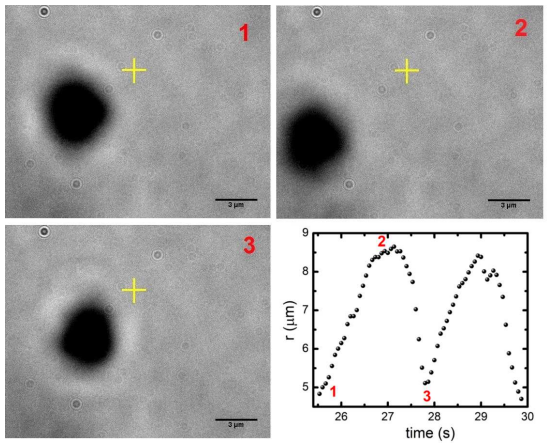

h

Figure 2.2: Successive video frames showing the displacement of a Bi_2Te_3 particle moving away from the optical axis (yellow cross mark) and then moving back towards the focus. The graph shows the distance of the particle from the optical axis over time. Frame 1 was taken at time $t_1 = 25.74\,\mathrm{s}$, frame 2 at $t_2 = 26.87\,\mathrm{s}$ and frame 3 at $t_3 = 27.80\,\mathrm{s}$. This experiment was performed with a Bi_2Te_3 spherical-like bead with average diameter $\sim 4.6\,\mu\mathrm{m}$. The bead have been placed at $z \sim 10\,\mu\mathrm{m}$. The motion presents a well-defined frequency for the oscillations, with period $T \sim 2\,\mathrm{s}$. The uncertainty in the measurement of position is $0.017\,\mu\mathrm{m}$. Adapted from Ref. [1].

exemplifying movies can be found on the web as supplementary files of Ref. [1]. They show in real time the standard behavior of TI microparticles at our optical tweezers setup (see **Video-1**, **Video-2** and Fig. 2.2). The Bi_2Te_3 beads are nearly-spherical, but oscillating movement was also observed for irregular shapes. The light beam is inciding perpendicular to the plane of the video, with optical axis being represented by a yellow cross mark. Variations in the shape of the shadow indicate rotations of the TI particle. At **Video-3**, we purposely used a dielectric particle in order to show its trapping, while the surrounding TI particles oscillate towards the optical axis. The mean value of the dielectric particle position after trapping was set as the optical axis position. The typical dynamics $r(\mu m) \times time(s)$ of a TI-particle (for a period of the oscillation) associated with frames of **Video-2** can be seen in Fig. 2.2.

The ImageJ software [198] was used to determine the coordinates $(x,\ y)$ of the centroid of the TI particles for each frame. Such procedure allowed us to obtain the particle position $r = \sqrt{x^2 + y^2}$ as a function of time. The TI particles oscillate in a xy-plane (parallel to the focal plane and perpendicular to the optical axis - see Fig. 2.1). Knowing the bead position as a function of time, the instantaneous velocities and accelerations can be promptly calculated using the method of *finite differences*. For a set of data points $\{t_i, r_i\}$, the derivative of the function $r(t_i)$ at point t_i can be obtained by

the *centered difference approximation*, i.e. the average of the line segment slopes between (t_i, r_i) and the neighboring points:

$$r'(t_i) = \frac{1}{2}\left(\frac{r_{i+1} - r_i}{t_{i+1} - t_i} + \frac{r_i - r_{i-1}}{t_i - t_{i-1}}\right). \tag{2.1}$$

The Stokes force F_s on the particle is then calculated as

$$F_s = 6\pi\eta a v, \tag{2.2}$$

where $\eta = 8.9\times10^{-4}$ Pa.s is the water viscosity at 25^{o}C, a is the particle mean radius, and $v = dr/dt$ is the particle velocity. The mean radius of the TI particles were obtained directly from the movies using the measurement tools of the ImageJ software.

On the other hand, the resulting force F_{res} acting on the particle can be calculated as

$$F_{res} = \frac{4}{3}\pi a^3 \rho \frac{d^2 r}{dt^2}, \tag{2.3}$$

where ρ is the density of the TI particle. For Bi_2Te_3 particles, $\rho = 7.85\times10^3$ kg/m^3.

The resulting force has three components, the optical force, the radiometric force, and the Stokes force. As will be seen in Section 2.3, our model gives an expression for the two first components (optical + radiometric forces), which we call F. Therefore

$$\vec{F}_{res} = \vec{F} + \vec{F}_s. \tag{2.4}$$

2.2.3 Preparation of the samples

In this Subsection we discuss the procedures for growing the crystals of topological insulators, as well as the preparation of micrometer-sized particles of these materials. The crystals of Bi_2Te_3 and Bi_2Se_3 were grown by the Bridgman-Stockbarger method in a vertical arrangement. From these crystals, we prepared TI particles with the use of laser ablation synthesis in liquid solution.

Growth of the topological insulators crystals: Bi_2Te_3 and Bi_2Se_3

Both crystals (Bi_2Te_3 and Bi_2Se_3) were grown by the Bridgman-Stockbarger method in a vertical arrangement. Pure starting materials, Bismuth (99.999%), Selenium (99.99%)

and Tellurium (%99.99), supplied by Aldrich Chem. Co., were used. The crystals growth took place in two steps. First, the stoichiometric compounds were synthesized by heating the pure elements (Bi and Te (Se)) in an ampoule at about 300^0C (for Bi_2Te_3) and 120^0C (for Bi_2Se_3) in a hydrogen environment to eliminate oxidized species. On suite, the ampoules were evacuated at room temperature and for Bi_2Te_3, it was heated to 200^0C for 24 hours and then up to 587^0C at a rate of 0.50^0C/min and left there for three hours. The system was then, cooled down at 0.20^0C/min in 72 hours. In the case of Bi_2Se_3 the ampoule was heated up to 750^0C at a rate of 0.50^0C/min and left there for 24 hours. After that the system was cooled down at a rate of 1.00^0C/min. At this point, the obtained products were inspected by x-ray diffraction and the synthesis of the compound was confirmed. In a second step, the single crystals were grown by heating the obtained compounds inside an evacuated and sealed quartz ampoule. In the case of Bi_2Te_3, the temperature was increased up to 271^0C, at a rate of 0.50^0C/min, and kept at this value, for two hours and then it was increased again, up to 587^0C, at a rate of 2^0C/min and left at this point for 24 hours. For Bi_2Se_3 the temperature was increased up to 750^0C, at a rate of 20^0C/min, and stayed at this value for 24 hours. After that both systems were then cooled down to room temperature at 0.10^0C/min.

Synthesis of TI-particles by laser ablation technique in liquid solution

The particles of Bi_2Te_3 and Bi_2Se_3 were synthesized by laser ablation technique in liquid solution. The experimental setup used to synthesize the particles of Bi_2Te_3 (and Bi_2Se_3) compound consists of using TI-crystals as a target material dispersed in a beaker, which is filled with $10cm^3$ of H_2O solution. The target was irradiated for 10 min under magnet stirring with the second harmonic of a pulsed Nd:YAG laser ($\lambda = 532$ nm; Quantel, model Brilliant B), operating at 10 Hz with 5 ns of pulse width, which was focused on the target with a spot size of about 1 mm in diameter using a lens with a focal length of 50 mm. The experiments were conducted at room temperature (~ 295 K).

2.2.4 Characterization of the Bi_2Te_3 and Bi_2Se_3 crystals

First, the obtained single crystals were characterized by X-ray (Laue) diffraction in order to probe their crystallinities. Then, the impurity levels were measured by XPS

and Auger electron spectroscopies, resulting in values below the detection limit of each technique. For the Bi_2Te_3 the Seebeck coefficient was also measured and its value (191.6μ V/K) was found to be in good agreement with published results for high-quality Bi_2Te_3 crystals [199]. Also, ARPES measurements have clearly shown the presence of a single, nondegenerated Dirac point at the center of the Brillouin zone (Γ point) in the band gap, which is a characteristic of strong topological insulators. The experimental value of the bulk band gap for this compound has been found to be on the range from 130 to 170 meV (about 6 times larger than the energy scale of room temperature, $K_BT \sim 26$ meV, therefore not allowing thermal excitations of electrons from the valence to the conduction band). Recent band structure calculations have confirmed an indirect gap about of 120 meV [200]. For the Bi_2Se_3 single crystal a detailed XPS and EELS study of the valence band have identified only features characteristic of the compound. Also, by comparison of the energies of the Bi*5d5* and Bi*5d3* interband transitions, as measured by the two techniques, it was possible to determine the position of the bottom of the conduction band of the compound to be 1.2 eV above the Fermi level [201]. Although the Bi_2Se_3 samples used in this work has not been examined by ARPES measurements, it is expected that - as well discussed in the literature [87] - it has a single nondegenerated Dirac cone on the energy band similar to Bi_2Te_3 and has spin-momentum locking as predicted for strong topological insulators. Crystals of Bi_2Te_3 have quintuple atomic layers structure as fundamental building blocks with height $c \sim 30,49$ Å [202]. Therefore, the micrometer-sized particles used in our experiments have about 1400 quintuple atomic layers and are expected to behave as bulk topological insulators, like the sample that was characterized.

2.3 Results and discussion

Fig. 2.1 shows our experimental setup along with the relevant parameters. TI particles located $z \sim 10$ μm below the focal plane have been observed to oscillate perpendicularly to the optical axis direction, say, parallel to the focal plane. On the other hand, if the particle is close enough to the focal plane ($z \lesssim 3.5$ μm), then the resultant repulsive force becomes high enough to drift it away, like occurs to typical metallic particles.

2.3.1 Effective model

Here, we propose a simple model that takes into account the competition between gradient force and the resulting repulsive force that act on the TI particle. Such repulsive force is mainly due to the radiometric effect that plays a role when the particles considerably absorb light from the laser beam (radiometric force). Our model allows one to predict the resultant force on the particle yielding its oscillatory dynamics. Let r be the radial distance from the optical axis and z be the vertical distance from the focal plane. For a Gaussian beam profile, the laser intensity at an arbitrary position (r, z), normalized by the corresponding intensity at the optical axis ($r = 0$, z), can be written appropriately by:

$$I_N = \exp\left(\frac{-2r^2}{w(z)^2}\right), \tag{2.5}$$

where $w(z)$ is the beam waist at a height z from the focal plane; it is related to the beam waist at the focal plane, $w(z = 0) \equiv w_0$, as below:

$$w(z) = w_0\sqrt{1 + \left(\frac{z}{z_R}\right)^2}, \qquad z_R = \frac{\pi w_0^2}{\lambda}. \tag{2.6}$$

Whenever we focus our attention at a height where the particle has no dynamics along the laser beam direction, we are only left with a non-vanishing force in the plane perpendicular to the optical axis. As the intensity profile presents azimuthal symmetry, the forces should depend only on the radial distance from the optical axis, r. Therefore, we are left with the problem of determining the net force dictating the particle dynamics along r, as it follows.

The effective resulting radiometric force acting on the particle is proportional to the laser intensity reaching it [72]. Therefore we write

$$F_r = \mathcal{F}_r \exp\left(\frac{-2r^2}{w(z)^2}\right), \tag{2.7}$$

where $\mathcal{F}_r$ accounts for the maximum magnitude of this force, at $r = 0$. Observe that equation (2.7) also implicitly includes the resulting effect of radiation pressure on the particle, since this force is also proportional to the laser intensity.

In turn, the gradient force, is given by:

$$F_g = -\frac{4rA}{w(z)^2}\exp\left(\frac{-2r^2}{w(z)^2}\right), \tag{2.8}$$

since F_g is proportional to the negative derivative of the beam intensity. The constant A is proportional to the maximum magnitude of the gradient force, $\mathcal{F}_g$, which occurs at $r = (1/2)w(z)$, by:

$$A = \frac{1}{2}\mathcal{F}_g w(z)\exp(1/2). \tag{2.9}$$

Finally, the resultant force $F = F_r + F_g$ can be written as:

$$F = \left(\mathcal{F}_r - \frac{2r\mathcal{F}_g\exp(1/2)}{w(z)}\right)\exp\left(\frac{-2r^2}{w(z)^2}\right). \tag{2.10}$$

In Fig. 2.3 it is shown how such forces behave as r varies. For that, we have taken: $w(z) = 5\,\mu$m, $\mathcal{F}_r = 4\,$pN and $A = 10\,$pN.μm, corresponding to $\mathcal{F}_g \sim 2.43\,$pN. For these parameters the resultant force is repulsive for $r < 2.5\,\mu$m and attractive for $r > 2.5\,\mu$m. Indeed, the value of r where the crossover between repulsive and attractive regimes occurs is given by $r_c = \mathcal{F}_r w(z)/2\mathcal{F}_g\exp(1/2)$. In addition, as long as $\mathcal{F}_r/2\mathcal{F}_g\exp(1/2) > 1$, then $r_c > w(z)$, yielding the repulsive regime, say, radiometric force dominates over gradient force and no oscillatory motion takes place. A more precise description of this dynamics would involve a number of other parameters such as the absorption coefficient of the particle, the relative refractive index, aberration effects and so forth. Although such effects could be taken into account, the agreement between the ex-

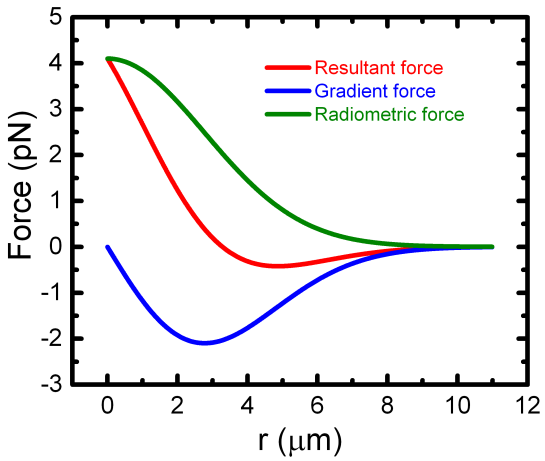

Figure 2.3: Typical theoretical behavior of the radiometric, gradient and resultant forces as functions of the TI-particle position, r. The radiometric (gradient) force is always positive (negative), while the resultant force is positive near the optical axis and negative otherwise. Here, we have used the parameters $w(z) = 5\ \mu$m, $\mathcal{F}_r = 4$ pN, and $A = 10$ pN.μm, corresponding to $\mathcal{F}_g \sim 2.43$ pN. Adapted from Ref. [1].

perimental data and our proposed model,
clearly indicates that such further effects are relatively less important and they could only bring minor quantitative corrections to those already accounted by the current model. At this point, it should be stressed that metallic beads experiences only the repulsive regime, once the radiometric forces (and also radiation pressure) are much higher than gradient force. Conversely, whenever ordinary dielectric particles are in order, gradient force largely dominates, yielding the usually observed trapping around the optical focus. Our findings regarding TI microsized beads open a new possibility, once they behave like light induced oscillators, whose quasiperiodic motion may be used to probe important properties in a number of experiments concerning optical tweezers, namely dynamical force measurements and microrheology studies.

2.3.2 Experimental results and comparison with theoretical model

The procedure used to obtain the forces in the experiments is detailed in Subsection 2.2.2. Essentially, the bead position is recorded using videomicroscopy, from which other dynamical variables, like velocity and acceleration are readily obtained, as well as, the net force acting on the bead. Such a force comes from three independent contributions: the optical, the radiometric, and the viscous (Stokes) force. Actually, in order to obtain the resultant force for comparison with the theoretical model described above, equation (2.10), one needs to subtract the contribution coming from the viscous force, which was calculated using the instantaneous velocity of the particle. [Three movies showing the motion of Bi_2Te_3 TI-particles can also be found in Ref. [1] as a Supplementary Material].

In Fig. 2.4 it is shown the typical dynamics of the TI-particles, where its position relative to the optical axis, r, is plotted as function of the time, t. Such results have been obtained for a Bi_2Te_3 spherical-like bead with diameter ~ 4.2 μm centered at $z \sim 10$ μm. The oscillations are well-defined in time with period $T \approx 3$ s. Their amplitudes vary between ~ 7 μm $- 9$ μm, with closest approximation to the optical axis observed to be ~ 3.2 μm. In addition, the variation in the amplitudes comes from the fact that $r(t)$ only computes the motion parallel to the focal plane, whereas the particle position sometimes presents small fluctuations along z direction. Besides, once the TI particles are not perfect spheres, some deviations in the amplitude could be also associated to their shape.

With the data from the first oscillatory cycle in Fig. 2.4, we have calculated the instantaneous velocity and acceleration of the particle at each instant of time. Knowing the density of Bi_2Te_3 ($\rho \approx 7.85 \cdot 10^3\,\mathrm{kg/m^3}$), the viscosity of the medium ($\eta = 8.9 \times 10^{-4}$ for deionized water) and calculating the Stokes force from Eq. (1.28), we have obtained the resultant force (gradient force + radiometric force) exerted on the bead from Eq. (2.4).

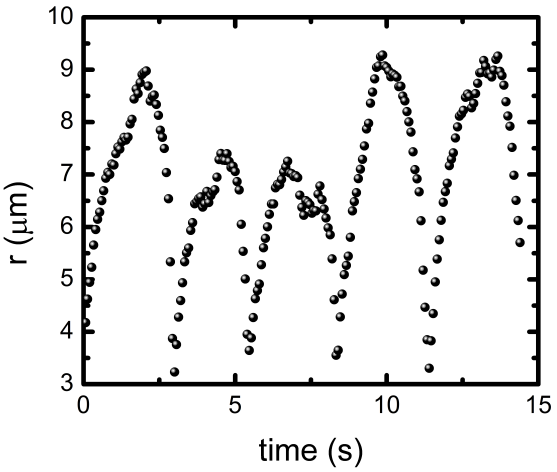

Figure 2.4: Typical dynamics of the TI-particles, $r(t) \times t$. The particle position $r(t)$ is measured relative to the optical axis, at $r = 0$. These experimental data have been obtained for a single Bi_2Te_3 spherical-like bead with average diameter ~ 4.2 μm. The bead have been placed at $z \sim 10$ μm. The motion presents a well-defined frequency for the oscillations, with period $T \approx 3$ s. The uncertainty in the measurement of position $r(t)$ is 0.017 μm. Adapted from Ref. [1].

During a complete oscillating cycle of a TI particle, gradient force is dominant in the attractive motion, in which the particle approaches the optical axis. Radiometric force, on the other hand, is dominant in the repulsive motion, in which the particle moves away from the optical axis. The dynamics of the two motion regimes (attractive and repulsive) are quite distinct. Such a difference is not evident if one restricts to the results of the particle position, shown in Fig. 2.4, but it becomes clearer whenever one looks at the forces. Indeed, in Fig. 2.5 it is shown the resultant force (radiometric + gradient force) as function of particle position, r, for both attractive (particle approaching the optical axis) and repulsive (particle moving away from the optical axis) motion regimes, obtained from the data of Fig. 2.4.

Note the difference in the behavior of the forces between attractive and repulsive regimes. Observe that in the attractive regime, the gradient force is dominant, and the resultant force is negative. As the particle approaches the optical axis, however, heating of the system generates a strong radiometric force that overcomes the gradient force and dominates the repulsive regime, so that the resultant force is positive. It is evident that in

the attractive regime the resultant force presents the characteristic behavior predicted by the effective model, being more appropriate for the fitting. In addition, it is noteworthy that our model fits the experimental data accurately, with the following values for the physical parameters: $w(z) = (5.55 \pm 0.15)\,\mu$m, $\mathcal{F}_r = (4.1 \pm 0.6)$ pN and $\mathcal{F}_g = (2.1 \pm 0.2)$ pN. For the other oscillatory cycles, the variations in the oscillation amplitude impart on the values of the forces $\mathcal{F}_r$ and $\mathcal{F}_g$, making them to vary from one cycle to the other, namely whenever very distinct amplitude cycles are considered. On the other hand, it is worthy to mention that the parameter $w(z)$ is very robust against amplitude variation, what is expected since $w(z)$ is a characteristic of the laser beam. Its average value, found considering different particle motions, reads $w(z) = (5.7 \pm 0.3)\,\mu$m. Taking $z \sim 10\,\mu$m to equation (2.6), yields $w_{0_{exp}} = (0.45 \pm 0.02)\ \mu$m, which is in good agreement to the predicted value of $2\lambda/\pi\text{NA} \sim 0.36\,\mu$m [203].

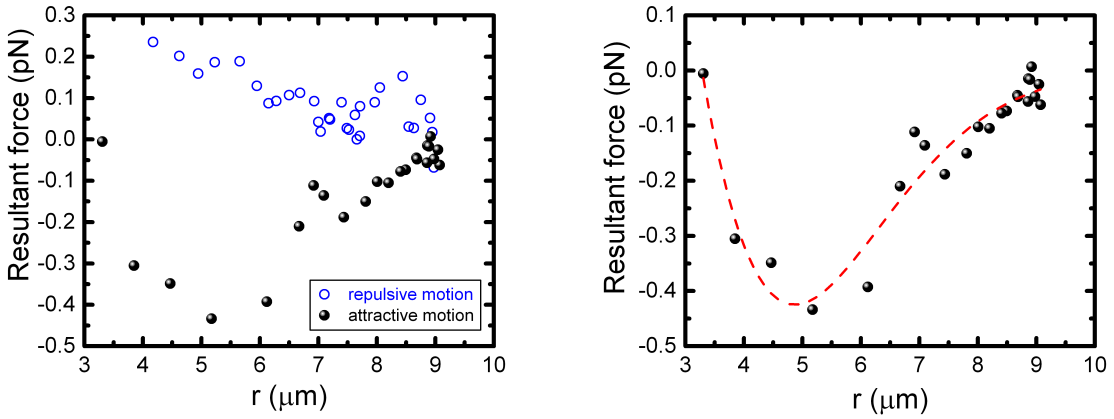

Figure 2.5: (*Left panel*) Experimental resultant force obtained from the first oscillatory cycle in Fig. 2.4, as function of particle position **r**. The attractive regime is represented by the black circles, while the open circles account for the repulsive regime. (*Right panel*) Fitting of Eq. (2.10) with the experimental data for the attractive regime shown in the left panel. Experimental data (*black circles*) are well-fitted by the theoretical model (*dashed line*). The estimated mean uncertainty in the calculation of the force is 0.03 pN. Adapted from Ref. [1].

The repulsive motion shown in Fig. 2.5 here can also be fitted to the model. Since $w(z)$ is a characteristic of the laser beam and therefore is the same for the two motions, the characteristic forces $\mathcal{F}_r$ and $\mathcal{F}_g$ must be different for the two types of motion. In fact, as discussed previously, for the attractive (repulsive) motion one must have $\mathcal{F}_r/2\mathcal{F}_g \exp(0.5)$ $<$ ($>$) 1. We have performed such analysis, however, since the resultant force in this regime presents a simpler behavior and the data dispersion is large (see Fig. 2.5), the

results returned from the fitting have high error bars. Physically, it is expected that our effective model is more accurate to fit the attractive regime, because in the repulsive regime the motion is driven by the radiometric forces, which are much more intricate to modelate.

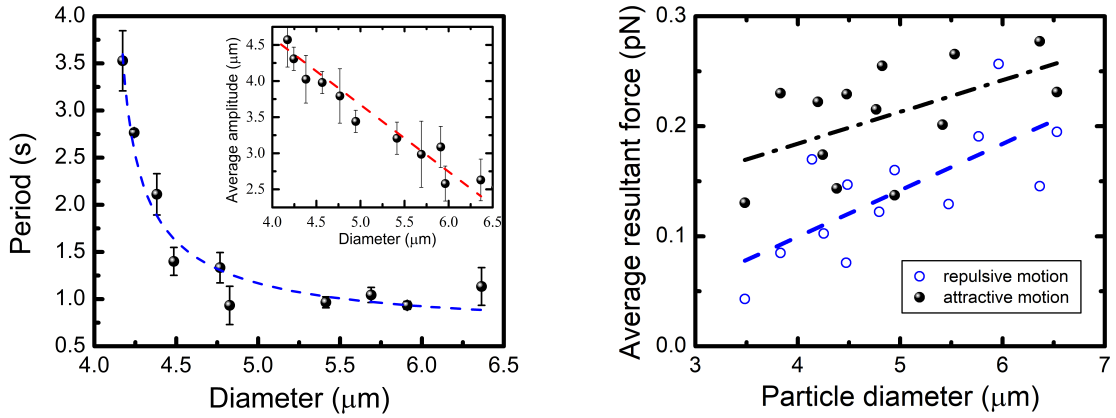

Figure 2.6: (*Left panel*) Period of the oscillatory motion as a function of the particle diameter. Experimental results (black circles) along with their respective errors (black bars). Note that as particle size increases the period diminishes in a way relatively well-described within the harmonic oscillatory regime (traced fitting curve). The inset shows the average amplitude for the particles with different sizes. Dashed red line is just a guide for the eyes and it illustrates its linear decreasing with diameter. All these measurements have been conducted with the particles around $z = 10\,\mu$m, where oscillations show up more evident. (*Right panel*) Average resultant forces as a function of the TI particle diameter. The forces here were calculated as averages over a complete oscillating cycle, separating the attractive (*black circles*) and repulsive (*open circles*) motions. The dashed lines are linear fits to the data that serve only as guides to the eyes. Adapted from Ref. [1].

Fig. 2.6 (left panel) shows how the period and amplitude (inset) of the oscillations depends upon beads diameter. Although the amplitude has a simple linear decreasing, the period shows a more interesting behavior. Smaller beads tend to oscillate slower than larger ones. For instance, a bead with diameter ~ 4.2 μm has a period ~ 3.5 s (frequency ~ 0.3 Hz), while another with ~ 6 μm has its frequency increased to ~ 1 Hz. Although these oscillations are not harmonic (recall the expression of the force, equation (2.10), along with the viscous dissipation), a first approximation for the equation describing the period as a function of the particle diameter can be obtained, and such a behaviour is well-captured within the simple harmonic regime, as follows. For that, recall that the gradient force comes from volumetric bulk refractions, then as particle radius, a, varies it is expected that $F_g \sim Aa^3$ (a is the bead radius). Once radiometric force increases with

the particle area then $F_r \sim Ba^2$, while Stokes force goes like $F_S \sim Ca$, where A, B, and C are constants. Restricting ourselves to simple harmonic oscillatory description dictated by these forces, the period, $T \sim 2\pi\sqrt{m/k}$ ($m = 4\pi\rho a^3/3$ is the particle mass) goes like $T \sim \sqrt{\frac{a^3}{Aa^3+Ba^2+Ca}}$. For the fitting depicted in Fig. 2.6 we have $T \sim \sqrt{\frac{a^3}{Aa^3+Ba^2+Ca}}$, with $A \sim 1.81\,\mathrm{s}^{-2}$, $B \sim 3.89\,\mu\mathrm{m\ s}^{-2}$, and C$\sim -46.50\,\mu\mathrm{m}^2\ \mathrm{s}^{-2}$.

In order to investigate how the magnitude of the measured forces (gradient force + radiometric force) depends on the particle size, in Fig. 2.6 (right panel) we present some measurements of the average forces as a function of the TI particle diameter. The forces here were calculated as averages over a complete oscillating cycle, separating the attractive (*black circles*) and repulsive (*open circles*) motions. The dashed lines are linear fits to the data that serve only as guides to the eyes.

Observe that in both regimes the average force increases with the particle size. In addition, the resultant average force is always higher in the attractive regime, at least for the diameter range studied here ($\sim$ 3.5 - 6.5 μm).

Particles with diameters within this range can be approximately considered in the geometrical optics regime [18], since the wavelength used was 1.064 μm. In this regime, if the particles were ordinary dielectric ones, it would be expected that the trap stiffness (and consequently the optical force at a fixed distance from the optical axis) decreases with the particle diameter [18]. Nevertheless, the results shown in Fig. 2.6 strongly suggest the opposite behavior. This result is certainly related to the frequency of oscillation of the TI particles, which increases with the particle diameter [see Fig. 2.6 (left panel)]. In fact, higher frequencies imply higher accelerations, and thus higher forces.

An important point to be stressed here concerns the actual possibility of tuning the particle period/frequency by just varying its size. Other improvements are certainly obtained by adjusting other physical parameters, like the beam power and so forth. In fact, we have performed an experiment with a single TI particle of $4.89 \pm 0.29\,\mu$m diameter to explicitly investigate how the period and amplitude of oscillations depend on the laser power (see Fig. 2.7). During the experiment, we increase the laser power from 37 mW to 100 mW, and have shown that the amplitude of oscillations increases linearly with the laser power, excluding the possibility of second order effects. The period of oscillation seems to be weakly affected by the power, presenting only a slight increase in such range. This results strongly suggest that, along with the particle size, the laser power can be

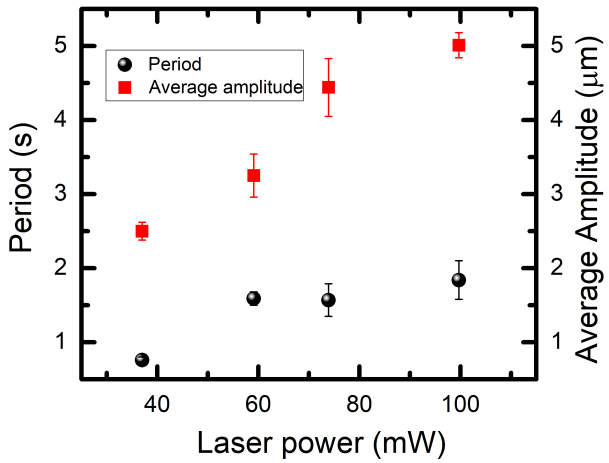

Figure 2.7: Average period (black circles) and amplitude (red squares) of oscillations as a function of the laser power. The same single particle of $4.89 \pm 0.29\,\mu$m diameter was used in all measurements. The amplitude linearly increases with the power of the beam, while the period presents only a small variation. The vertical bars are standard errors over the averages. Adapted from Ref. [1].

used to control the dynamic quantities of the optically induced oscillators, of interest for future applications.

2.4 Conclusions

We have observed that micro-sized topological insulator (Bi_2Te_3 and Bi_2Se_3) particles oscillate perpendicularly to the optical axis whenever subject to a highly focused Gaussian laser beam optical tweezers. Physically, such oscillations are a result of a delicate balance in the competition between gradient forces and radiometric forces. This last component acts as a driving force, changing the usual overdamped motion obtained for ordinary dielectric particles into a driven (but also damped) oscillatory motion. Even though the oscillations are not harmonic, the period/frequency appears to remain practically constant during a number of cycles, being well-defined in time. We have also observed that frequency and amplitude of oscillations are also dependent on the particle size, the former increases with the beads diameter in such a way well-described by a simple harmonic approach. Both of these features are important for practical purposes and they may be further improved by combining particle size/shape with modulated intensity/power laser beam. For instance, beads having more regular spherical shape are crucial for highly precise experiments. This precision is important to make such optically induced

oscillators useful in dynamical force measurements in macromolecules and biopolymers. They may also play an important role in optical rheology of biological membranes and soft matter interfaces. In such type of experiments one usually needs to induce oscillating forces on the investigated systems. Nowadays, the straightforward approach is to mechanically oscillate the microscope stage using piezoelectric actuators. The main results of our present work strongly suggest that these oscillatory forces can be implemented in the system in a more suitable way: the intrinsic oscillations of TI microparticles under a laser beam are such that those desired oscillatory forces are applied to the system with complete and pure optical control, without the necessity of mechanical interventions on the laser setup.

One may wonder whether our observations regarding TI optically induced oscillators may occur to other materials-made microspheres. To our best findings, this may be the case provided that the beads have an intermediary surface conductivity (density of charged states) along with a good transparent bulk (relatively high skin depth). These two key characteristics are accomplished by topological insulator beads. Whether other materials may present similar characteristics remains to be investigated and it should enlarge even more the issue of optically induced oscillators.

Chapter 3

Extending the Ashkin's model to light-absorbing particles

In this chapter, we discuss the results reported in Ref. [7] [Adapted with permission from (W. H. Campos, J. M. Fonseca, J. B. S. Mendes et. al., "How light absorption modifies the radiative force on a microparticle in optical tweezers," *Applied Optics* **57**(25), 7216-7224 (2018). https://doi.org/10.1364/AO.57.007216) © The Optical Society][1], where we propose a generalization of the Ashkin's model for the radiative force exerted on a spherical bead. Besides the usual forces related to refraction and reflection of light, the model accounts for the contribution due to attenuation/absorption of light in the bulk of the particle. We discuss in detail the balance between refraction, reflection, and absorption for different optical parameters and particle sizes. Such a contribution is important because absorption is known to generate radiation pressure, and it has also shown to play an important role in the optically induced oscillations reported in Ref. [1]. Our findings contribute to the understanding of the optical trapping of light-absorbing particles, and may be used to predict whenever absorption is important in real experiments.

Whenever light is absorbed by a particle subjected to a laser beam, a "microscopic" description of the exerted forces requires a clear distinction between thermally originated and radiative effects. In Subsection 1.1.1, we have seen that reflection and refraction of light can be used to trap small dielectric particles. The Ashkin's model captures the main results for the radiative (gradient + radiation pressure) force exerted on a

[1]Copyright credit line obtained, along with permission, via email made available for this purpose by the publisher at https://www.osapublishing.org/submit/review/copyright_permissions.cfm.

dielectric particle in the geometrical optics regime [2, 3, 18]. It can also be adapted to describe the radiation pressure in a fully reflective (metallic) bead (see Subsection 1.1.4) [72]. Absorption of light by the bead is usually neglected in theoretical calculations for the geometrical optics regime, but it is known that it occurs in the trapping of semi-transparent particles, which interpolate between fully transparent and fully reflective ones.

In this work, we propose a generalization of the usual model accounting for the radiative force exerted on a spherical particle by a single light ray in the geometrical optics regime [2, 3]. The absorption/attenuation of light is included in such a way that the model captures the limiting cases of fully transparent (dielectric) and fully reflective (metallic) particles [2, 3, 72], with the novelty of accounting for any intermediary value of the absorption coefficient, namely the case of semi-transparent particles made from semiconductor materials. Our results suggest that such a consideration is important mainly when the skin depth of the light is comparable to the size of the particle.

As a direct example of how the model can be applied, we calculate the total radiative force exerted by a Gaussian laser beam on a particle highly out of the laser focus, a setup similar to that reported in the work of Ref. [9], and discuss upon the modifications on this force caused by different values of the absorption coefficient. Our results suggest that finite values of absorption can either increase or decrease the magnitude of the radiative force, depending on the particle size. Also, we show that our proposal significantly improves the comparison between recently reported experiments and the radiative force calculated with the usual Ashkin's model. We also discuss how the particle weight becomes comparable to the optical forces if its density is high enough, which is the case of the topological insulator microparticles used in Ref. [9], and a number of semiconductor materials where light absorption is expected to be important.

3.1 Objectives

We devote ourselves to derive an analytical expression for the radiative force in the geometrical optics regime, including the attenuation/absorption of light by the bulk of the particle. The expression should account for any value of the absorption coefficient, including the two limiting cases exploited previously on the literature, say, fully transparent and fully reflective beads. We investigate how the balance between refraction, reflection

and absorption of light modifies the radiative force, by exploring different values of the refractive index and the absorption coefficient. We also calculate the total radiative force exerted by a Gaussian laser beam on a spherical particle out of the laser focus, investigate how it is modified by light absorption and compare the calculations with experimental results. Furthermore, we investigate the importance of the apparent weight of the particle on optical tweezers experiments, comparing it with the z component of the total optical force.

3.2 Methods

The methods applied in this study are those of geometrical optics at interfaces. Basically, an incoming light ray is partially reflected and refracted at the surface of a spherical particle, according Snell's law. Multiple reflections at the inside surface are also taken into account, along with attenuation/absorption of the ray in the bulk of the material, according to the Beer's law. The force exerted on the particle is calculated considering the transfer of linear momentum from the light ray to the material, accounting for all reflections at the surface.

3.3 The model: spherical absorbing particle

As usual in geometrical optics regime, we follow the main ideas of Ref. [2] to obtain the radiative force exerted by a light ray on a spherical bead. In their model, the authors obtain the radiative force by computing the variation of the linear momentum of light, as a result of the interaction with the particle surface. They do not consider absorption of light by the particle, so that only reflection or refraction at the surface can modify the linear momentum of the light ray.

Here, we consider a single ray of power dP interacting with an absorbing spherical bead (Fig. 3.1). Every time the ray reaches the bead surface, a fraction R of the incoming power is reflected and a fraction $T_{surface} = 1 - R$ is transmitted through the interface (i.e. R is the reflectivity and T is the transmissivity at the surface). As a result of the reflection and refraction, linear momentum is transferred from the light ray to the bead, exerting a force whose magnitude and direction depends on the angle of incidence, ξ. If absorption is not considered, 100% of the power transmitted

through the surface reaches the opposite side. Say, the particle is supposed to be perfectly transparent, which works well for dielectric beads usually made of polystyrene. However, for general materials the absorption of light cannot be neglected, and we expect that only a fraction $e^{-\alpha(2l\cos\zeta)}$ of the transmitted power will travel across the absorbing particle (Beer's law), where l is the particle radius and ζ is the angle of refraction. α is the absorption coefficient of the material, which can be related to the extinction coefficient, κ, by $\alpha = 4\pi\kappa/\lambda$ [204]. Note that we are working with the real component of the refractive index of the particle, n_p, which results in a real value for the angle of refraction ζ, since $n_m \sin\xi = n_p \sin\zeta$. A completely equivalent approach could be used, where both the refractive index and the angle of refraction are complex numbers. In such case, $n_m \sin\xi = \sqrt{\epsilon' + i\epsilon''}\sin\zeta$, where ϵ' and ϵ'' are the real and imaginary parts of the complex relative dielectric constant, respectively [204]. In the former approach, light absorption is accounted by α, while ϵ'' accounts for absorption in the latter approach.

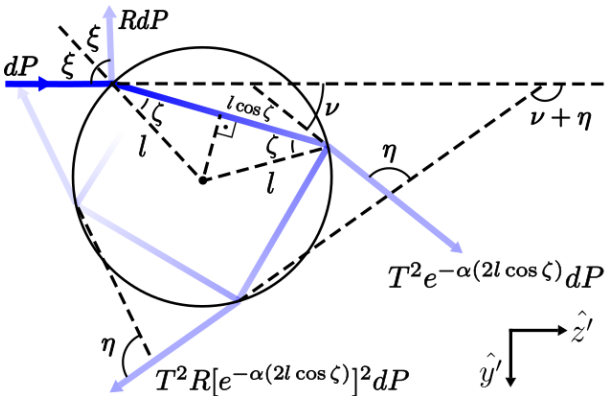

Figure 3.1: Light ray interacting with an absorbing particle. Besides the initial reflection and refraction suffered when it reaches the particle, the ray splits again every time it reaches the inside surface. Furthermore, it suffers an attenuation when propagating throughout the bulk of the particle to the opposite side. ξ and ζ are the incidence and refraction angles, respectively, and l is the sphere radius. See text for discussion. Adapted from Ref. [7].

Once the incident light ray penetrates the interface, there will be new reflections/-transmissions every time it interacts with the inside surface (Fig. 3.1). In each interaction, a fraction $T^2R^n\left[\exp^{-\alpha(2l\cos\zeta)}\right]^{n+1}$ of the initial power leaves the particle in a different direction than that of the incident ray (n accounts for the number of times the ray was reflected before leaving the particle), i.e., there is also a transfer of linear momentum from the ray to the particle due to multiple reflections/transmissions.

We choose the z'-axis to be in the direction of the incident ray, and the y'-axis to be in the plane of incidence, which contains both the light ray and the center of the

particle. The change in the linear momentum of the sphere is obtained by summing up the individual contributions of each ray-surface interaction, with $d\vec{p}_{particle} = -d\vec{p}_{ray}$. Details on the calculations are provided in Appendix A, but the final force exerted on the bead can be written as [2, 18]:

$$d\vec{F} = \frac{n_m}{c}[\mathrm{Re}(Q_t)\hat{z}' + \mathrm{Im}(Q_t)\hat{y}']dP, \tag{3.1}$$

where n_m is the refractive index of the surrounding medium, c is the speed of light, and

$$Q_t = 1 + R\exp(2i\xi) - T^2\frac{\exp[2i(\xi-\zeta)]}{e^{2l\alpha\cos\zeta} + Re^{-2i\zeta}}. \tag{3.2}$$

This result covers the two limiting cases studied previously in the literature. Indeed, taking $\alpha = 0$, one recovers the usual expression of Q_t for fully transparent/dielectric beads [18]. In turn, taking $\alpha \to +\infty$ one recovers the expression for metallic particles reflecting all the incoming light, say, $Q_t = 1 + R\exp(2i\xi)$ [72].

To get intuition about when consideration of the absorption coefficient is important, let us investigate the skin depth, which can be defined as $\delta \equiv 1/\alpha$. The skin depth gives an estimation of the distance traveled by light before its power falls to $1/e$ of its value at the surface. Particles used in optical tweezers are usually a few micrometers large, and transparent materials have $\delta \to +\infty$, so that light can travel a distance much larger than the particle size before being considerable attenuated. In such case the transfer of momentum due to absorption is minimal and can be safely neglected, as usual. Otherwise, if the particle is metallic, $\delta \to 0$ (or usually a few nanometers). This is equivalent of considering a non-absorptive particle with fully reflective surface, i. e. light cannot reach the bulk, and therefore, cannot be attenuated. Here, transfer of momentum due to both refraction and absorption is minimal and can be neglected. A more interesting scenario arises when we consider a skin depth comparable to the particle radius, $\delta \sim l$. Semiconductors materials, for example, can have a skin depth on the order of micrometers, making the microparticles semi-transparent. In such case, absorption of light by the particle is significant and should not be neglected in theoretical calculations. In this case, a small change in the absorption coefficient can lead to an appreciable modification in the radiative force. This will be discussed in more details in Section 3.4.

Now, consider a linearly polarized light ray and take the average over the two laser

polarizations, TE and TM. Assuming no preferential polarization, the reflectivity R can be written as [18, 58]:

$$R(\xi,\zeta) = \frac{1}{2}\left[\frac{\sin(\xi-\zeta)}{\sin(\xi+\zeta)}\right]^2 + \frac{1}{2}\left[\frac{\tan(\xi-\zeta)}{\tan(\xi+\zeta)}\right]^2. \tag{3.3}$$

The refraction angle reads $\zeta(\xi) = \arcsin\left[\frac{n_m}{n_p}\sin\xi\right]$ (Snell's law), where n_p is the refractive index of the particle. Fig. 3.2 shows the behavior of the reflectivity $R(\xi,\zeta) = R(\xi)$ for $0 \leq \xi < \pi/2$ and different values of $n_p > n_m$. For polystyrene particles (usually adopted in experiments), which have $n_p \approx 1.6$, light is mostly transmitted throughout the material. The exception is for $\xi \to \pi/2$ (tangent angles), where light is mostly reflected by the surface. However, in particles with higher index of refraction, such as the Bi_2Te_3 topological insulator (typical value of $n_p \approx 5.5$ [205]), a considerable amount of light is reflected even for small angles, generating radiation pressure. If the material has a very high refractive index, reflectivity is close to one. Therefore, the surface does not allow penetration of light rays to the bulk, and the particles should not distinguish between different values of the bulk absorption coefficient α.

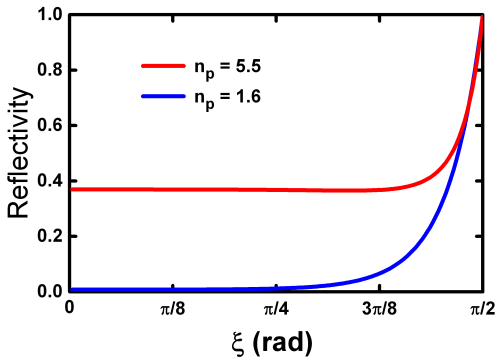

Figure 3.2: Surface reflectivity, R, as function of incident angle, ξ. Higher refractive index of the particle, n_p, leads to higher reflectivity. Also, light is more reflected for tangent angles of incidence, $\xi \to \pi/2$. We take $n_m = 1.33$, the refractive index of deionized water. Adapted from Ref. [7].

3.4 Results and Discussion

The balance between refraction, reflection and absorption can be better understood by studying the real and imaginary components of the adimensional factor Q_t. As usual in the literature, we define $Q_s \equiv \mathrm{Re}(Q_t)$ and $Q_g \equiv \mathrm{Im}(Q_t)$. The former corresponds to the component of the force along z'-axis, and indicates the strength in which the ray pushes the particle along its direction of incidence. The latter corresponds to the component of

the force along y'-axis and indicates the strength in which the bead is attracted ($Q_g < 0$) or deflected ($Q_g > 0$) along the transverse direction. Fig. 3.3 shows the plots of Q_s and Q_g as function of the incident angle ξ for a particle with radius $l = 2.1\,\mu$m and different values of n_p and α.

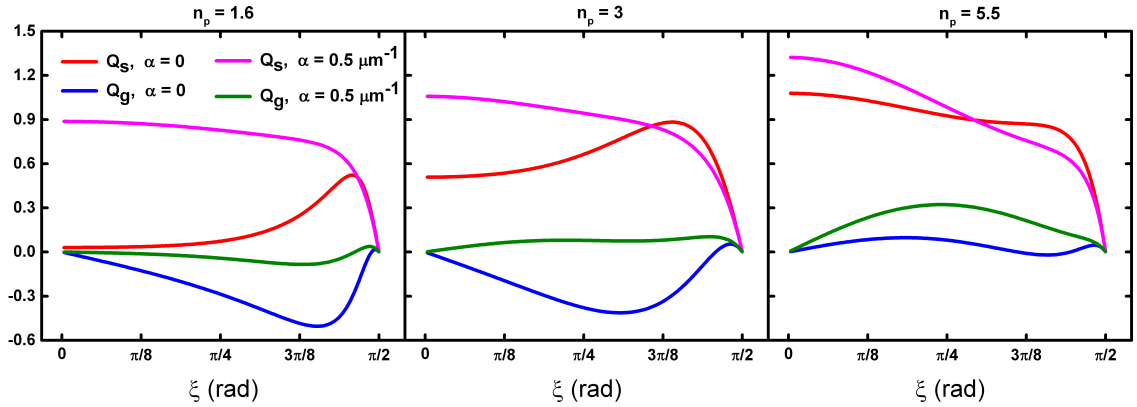

Figure 3.3: Plots of Q_s and Q_g as functions of the incidence angle, ξ, for different values of the refractive index, n_p, and absorption coefficient, α. As n_p increases, the influence of absorption in the bulk is minimized, since a significant fraction of the light is reflected by the surface and cannot be attenuated in the bulk. We have used $n_m = 1.33$, and $l = 2.1\,\mu$m for the sphere radius. Adapted from Ref. [7].

The low reflectivity of particles with small refractive index allows a great amount of light to be transmitted through the surface. As a consequence, these particles are very sensitive to different values of the absorption coefficient. In fact, for $n_p = 1.6$, Fig. 3.3 (left panel) shows that there are significant changes in the behavior of Q_s and Q_g for different values of α. Note the increasing in the adimensional force along z'-axis, Q_s, as the absorption coefficient changes from $\alpha = 0$ to $\alpha = 0.5\,\mu\text{m}^{-1}$, which is expected since absorption must generate radiation pressure. If $\alpha = 0$, $Q_g < 0$ for all values of ξ, and the force along y'-axis is attractive, as known for polystyrene particles. However, for $\alpha = 0.5\,\mu\text{m}^{-1}$ such attraction is weakened by the absorbing bulk of the particle. In this case, the skin depth $\delta = \alpha^{-1} = 2\,\mu$m is smaller than the particle diameter ($4.2\,\mu$m), so the light ray is attenuated before all multiple reflections can contribute significantly to Q_g.

For a particle with intermediary refractive index, say $n_p = 3$ (Fig. 3.3, center panel), Q_s is higher than in the previous example even for $\alpha = 0$. This is a consequence of the higher reflectivity, R, which allows the light to be only partially transmitted through the surface. Nevertheless, $\alpha = 0.5\,\mu\text{m}^{-1}$ implies in an increasing of the adimensional

force along z' -axis, Q_s, since a fraction of the light penetrates the bulk in order to be attenuated. Notice that in this case, $Q_g < 0$ if $\alpha = 0$, but an absorption coefficient of $\alpha = 0.5\,\mu\text{m}^{-1}$ eliminates the attractive behavior along y'-axis.

For higher values of n_p, a greater amount of light is reflected by the surface, and absorption does not change the behavior of Q_t in a significant way, since only a small fraction of light penetrates into the bulk (Fig. 3.3, right panel). Note that in this case ($n_p = 5.5$), even if $\alpha = 0$ we have $Q_g > 0$ for most values of ξ, i.e. reflection assures that the particle will not be attracted along y'-axis . It can be shown that in the limit of very high refractive index (say $n \gtrsim 20$, in our calculations) there are virtually no distinctions between Q_t for $\alpha = 0$ and for $\alpha \neq 0$, since the interface reflects all the incoming light.

It is evident, from the above results, that when considering interaction of a light ray with a spherical bead, the main consequences of a non-zero value of the absorption coefficient is to partially suppress the multiple reflections/transmissions taking place in the inside surface. Such a suppression can become total if the skin depth is much lower than the particle radius, $\delta << l$.

Radiative force exerted by a focused Gaussian beam

As a direct example of how the model can be applied, let us consider a focused Gaussian laser beam propagating along z-axis, toward the focal plane (Fig. 3.4). This is a very common setup, found in many applications of optical tweezers [18–20]. According to the experimental results reported in Ref. [9], if an absorbing particle is placed close enough to the focal plane, the radiometric force is very high and completely overcome the radiative. Therefore, we are interested in a situation where the bead is placed highly out of the beam focus. Fig. 3.4 depicts the spherical particle at a distance z below the focal plane, while the origin of the coordinate system was chosen to be at the beam focus. We set the z-axis along the optical axis, toward the objective lens. The x-axis was chosen so that the center of the sphere lies in the x-z plane, and ρ is the radial distance from the optical axis to the geometrical center of the sphere.

The procedure used to calculate the total radiative force exerted on the spherical bead is described in Appendix B. In summary, the force exerted by a single ray is calculated using Eq. (3.1), and integration over all the rays reaching the sphere gives the final result. In order to perform the numerical calculations, we set $P_t = 15.4\,\text{mW}$ for the total

laser power, and $\sigma = 0.136\,\text{cm}$ for the beam waist before it passes through the objective. The focal length and the refractive index of the medium are taken $f = 0.375\,\text{cm}$ and $n_m = 1.33$, respectively. These are typical values from experiments with optical tweezers.

Figure 3.5 (top panel) shows the radial component of the radiative force along x-axis for a particle of refractive index $n_p = 3$, and different values of the absorption coefficient, α, and radius, l. Observe that for smaller particles ($l = 2.1\,\mu\text{m}$), a higher value of α implies in an increasing of the radial force pushing the particle toward the optical axis, similar to the force driven by reflection of light in the surface of metallic particles, when trapped in two dimensions [71]. This can be understood by the fact that all the incoming rays are directed toward the focus of the light beam, and their linear momentum is transferred to the particle through absorption/reflection. Surprisingly, the situation is inverted for bigger particles ($l = 4\,\mu\text{m}$). In this case, a higher value for α decreases the magnitude of F_x, weakening the attraction toward the optical axis. This result suggests that attraction of bigger particles is driven mainly by the multiple reflections/transmissions at the inside surface, and suppression of such interactions by absorption of light in the bulk causes the magnitude of the radial force to decrease. This result is consistent with the known fact that tri-dimensional stable trapping of very small metallic particles (Rayleigh regime) are more efficient than that of dielectric ones [66], while bigger metallic particles cannot be stably trapped in three dimensions [71].

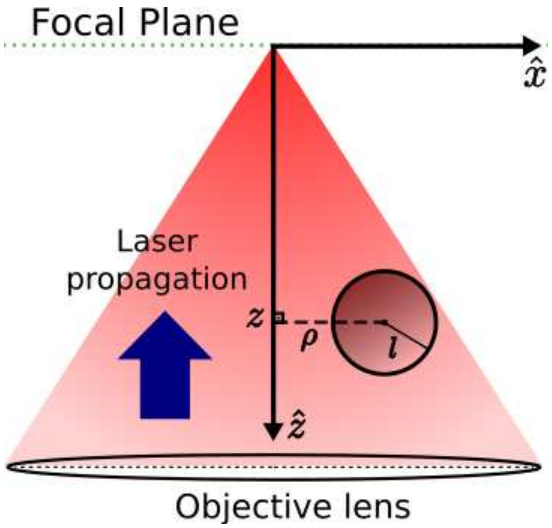

Figure 3.4: Illustration of a focused Gaussian light beam and definition of the coordinate system. The spherical particle is placed a distance z below the focal plane, and a distance ρ from the optical axis. The laser propagates from the objective lens to the origin of the coordinate system. Adapted from Ref. [7].

Figure 3.5 (bottom panel) shows the azimuthal component of the optical force along z-axis for different values of the absorption coefficient, α, and the particle radius, l. No inversion is observed for bigger particles, i.e. for both $l = 2.1\,\mu\text{m}$ and $l = 4\,\mu\text{m}$,

a higher value of the absorption coefficient α implies in an increasing at the magnitude of the force pushing the particle toward the focal plane (observe in Fig. 3.4-a) that the z-axis points down, so a negative value of F_z means a force pointing up to the focal plane).

From Fig. 3.5 (top panel), it is evident that there must be a critical radius l_c where the behavior of the force with absorption coefficient is reversed. Actually, in geometrical optics regime, the waist of the laser beam is expected to significantly influence the critical radius. In fact, Fig. 3.6 shows that l_c increases linearly with the beam waist, σ. At the critical radius, the absorption coefficient α almost does not contribute to the radiative force exerted on the particle.

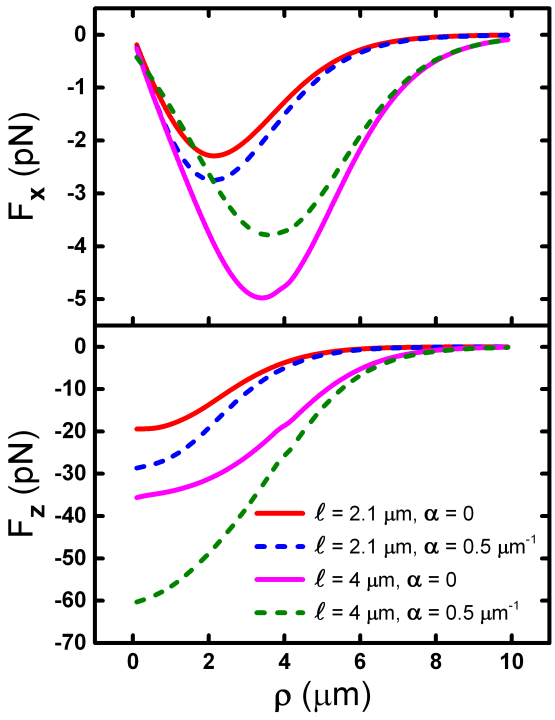

Figure 3.5: Radial and azimuthal components of the optical force along x-axis and z-axis, respectively, as function of the radial distance ρ. We set $n_p = 3$ for the refractive index of the bead. The top panel shows the behavior of the radial force, F_x, for different values of the particle radius, l, and absorption coefficient, α. The bottom panel shows the behavior of the azimuthal force, F_z, for the same parameters. See text for discussion. Adapted from Ref. [7].

The absorption of light can have an effect on the transfer of angular momentum to the sphere, eventually making the particle to rotate. However, here we are devoted only to describe the total radiative force exerted on an absorbing particle in optical tweezers. The well-known phenomena of torque generation by transfer of spin and orbital angular momentum has been extensively investigated in the literature for both absorbing and non-absorbing particles [206–209].

It is important to say that we are not describing any particle dynamics here, since this demands inclusion of radiometric forces. Nevertheless, in what follows we discuss about how the buoyancy and weight of denser particles can influence the optically

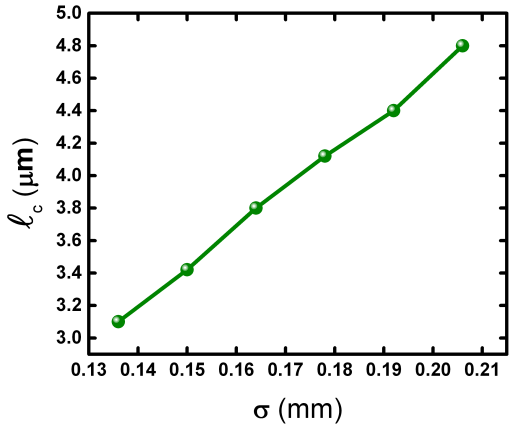

Figure 3.6: Critical radius, l_c, as function of the laser beam waist, σ. Notice that the increasing is approximately linear. Adapted from Ref. [7].

induced oscillations reported in Ref. [9]. Consider a particle of radius $l \sim 2.1\,\mu$m, which leads to a buoyancy around $\sim 0.38\,$pN. If the particle is made from polystyrene (density $\sim 1.04 \times 10^3$ kg/m^3), it has a weight around $\sim 0.4\,$pN. These forces balance each other and become negligible in most experiments, when compared to the magnitude of the other forces involved. However, here we are interested in materials with non-negligible absorption, such as Ge, Bi_2Te_3, and Bi_2Se_3. These materials are usually denser, and the weight can overcomes the buoyancy. For instance, the density of the Bi_2Te_3 topological insulator used in Ref. [9] reads $\sim 7.85 \times 10^3$ kg/m^3, corresponding to a weight around $w \approx 2.98\,$pN.

To be clearer, let us define the z''-axis to be antiparallel to the z-axis, so that the weight points in its negative direction. Fig 3.7 shows the plot of $F_{z''} - w'$ ($F_{z''}$ is the radiative force along z'', and w' is the apparent weight) as function of the radial distance ρ. Near the optical axis, $F_{z''}$ overcomes the apparent weight, pushing the particle toward the focal plane. Radiometric forces would also contribute to the force along this direction. However, at larger values of ρ it is the apparent weight that overcomes the optical force, and the particle must fall toward the coverslip. This point is important in dynamic systems such as that reported in Ref. [9], where the particle approaches and moves away from the optical axis in a quasi-periodic motion. Such a remark leads us to predict that oscillations also take place along the z-axis, where the apparent weight should compete with the radiative and radiometric forces. This is not discussed in the work of Ref. [9], but certainly worth experimental investigation in the future.

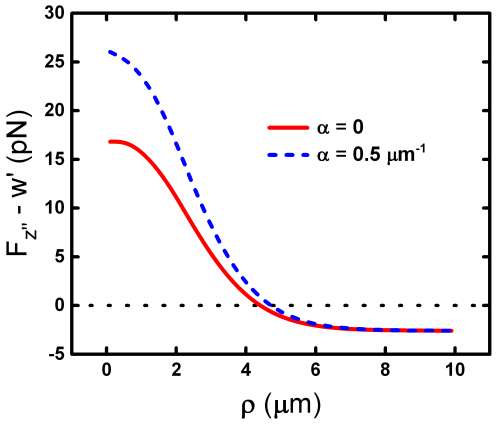

Figure 3.7: Resultant force ($F_{z''} - w'$) along z''-axis as function of the radial distance, ρ, for a particle with radius $l = 2.1\,\mu$m, $n_p = 5.5$, and density $\sim 7.85 \times 10^3\,\mathrm{kg/m^3}$ (as known for Bi_2Te_3 TI's). The particle is pushed toward the focal plane for positive values of the resultant force, while for negative values the weight overcomes the optical force. The same behavior is observed for both $\alpha = 0$ and $\alpha = 0.5\,\mu\mathrm{m}^{-1}$. Adapted from Ref. [7].

Although many calculations regarding optical trapping rely on the generalized Lorenz-Mie scattering theory, for spheres of size a larger than the light wavelength, λ, the Mie series converges slowly, and intricate computational techniques are necessary to overcome this inconvenience [64, 65]. In such regime, the geometric optics approach leads to simpler results, being useful for comparison with experimental observations.

Fig. 3.8 shows the predicted radiative force for the usual ($\alpha = 0$) and generalized ($\alpha = 0.11\,\mu\mathrm{m}^{-1}$) Ashkin's model, along with experimental data, for a Bi_2Te_3 particle of radius about $a \sim 3.1\,\mu$m optically trapped in deionized water. Spherical aberration was included in numerical calculations for both curves as described in Ref. [18]. We have used $n_p = 5.5$ for the particle refractive index, as reported in Ref. [205]. The methods used to obtain the experimental data are described in Ref. [9], where it was reported that Bi_2Te_3 particles oscillate perpendicularly to the optical axis of a Gaussian laser beam optical tweezers, remaining suspended about $\sim 4\,\mu$m above the coverslip and $\sim 10\,\mu$m below the focal plane. The closest approximation to the optical axis was observed to be about $\sim 3.2\,\mu$m. Notice that the usual Ashkin's model (neglecting light absorption) greatly overestimates the magnitude of the radiative force obtained from the experimental data. On the other hand, by using the generalized model one can find an effective value for α so that comparison between theory and experiment is significantly improved. It is worth noting that, so far, there is no microscopic and adequate model that completely explains

the forces exerted on the Bi_2Te_3 particles. Our results represent a step toward the full understanding of such a novel and intriguing phenomena.

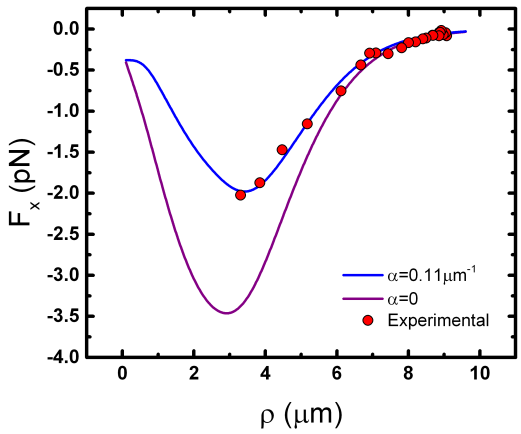

Figure 3.8: Predicted and observed radiative force exerted on a Bi_2Te_3 particle of radius $a \sim 3.1\,\mu$m, trapped in a Gaussian laser beam optical tweezers. The purple curve shows the radiative force for neglected absorption ($\alpha = 0$, usual Ashkin's model), and the blue curve shows the radiative force for an effective absorption of $\alpha = 0.11\,\mu\text{m}^{-1}$. The red dots represent the experimental data. In both calculations and experiments, we have used a laser power of 25 mW, measured at the objective entrance. The uncertainty in the measurement of position is $0.017\,\mu$m, and the estimated mean uncertainty in the calculation of the force is 0.03 pN. Adapted from Ref. [7].

3.5 Conclusions

Although the optical trapping of dielectric and metallic particles in optical tweezers has been well understood, this is not the case for semi-transparent materials. If the skin depth is comparable to the size of the bead, absorption of light can significantly modify the properties of the trapping. A simple generalization of Ashkin's model [2] is proposed in order to include absorption/attenuation of light into account, when considering a spherical bead under the incidence of a single light ray. Our results account for an arbitrary value of the absorption coefficient in the bulk of the bead, including the two limiting cases previously studied in the literature, namely, perfectly dielectric [18] and perfectly metallic particles [72]. Our findings suggest that attenuation effects becomes important mainly when the skin depth is comparable to the particle size. The radiative force along the light ray direction increases with the absorption coefficient, and the radiative force along the transverse direction (which is usually attractive) can be suppressed and become repulsive

with an increase in the absorption coefficient. We have also calculated the radiative force exerted on a spherical particle under a Gaussian laser beam optical tweezers. Interestingly, our results suggest that the effective contribution of absorption/attenuation of light by the particle bulk highly depends on its size. If the particle is small, increasing in the absorption coefficient leads to an increasing in the radial force pushing the particle toward the optical axis. However, for bigger particles the attraction is driven mainly by the multiple reflections/transmissions at the inside surface, which are suppressed by absorption of light in the bulk, causing the magnitude of the radial force to decrease. The critical radius where this inversion occurs is shown to be proportional to the laser beam waist.

We compare the theoretically predicted radiative force with recent experimental observations (Fig. 3.8), namely, Bi_2Te_3 particles trapped in a Gaussian laser beam optical tweezers [9]. Compared to the usual Ashkin's model, the present model accounting for absorption significantly improves the prediction of the minimum point of the radiative force, and mainly, it gives the quantitatively correct value for the force exerted on the particles. As there is no microscopic and adequate model that completely explains the experimental observations, we believe that our results represent a significant contribution to the field of optical trapping, mainly regarding the novel phenomena reported in Ref. [9].

Appendix A

From Fig. 3.1, it can be seen that the component of the radiative force along z'-axis is given by [2]:

$$dF_{z'} = \frac{n_m}{c}\left\{1 + R\cos(2\xi) - T^2\sum_{n=0}^{+\infty} R^n\left[e^{-2l\alpha\cos\zeta}\right]^{n+1}\cos(\nu + n\eta)\right\}dP, \tag{3.4}$$

where n_m is the index of refraction of the medium, $n = 0, 1, 2, 3...$ is an integer number, and the angles ξ, ζ, ν, η are indicated in Fig. 3.1. This can be easily shown to be:

$$dF_{z'} = \frac{n_m}{c}\mathrm{Re}\left\{1 + Re^{2i\xi} - T^2\frac{e^{i\nu}}{e^{2l\alpha\cos\zeta} - Re^{i\eta}}\right\}dP. \tag{3.5}$$

Using the geometric relations $\nu = 2\xi - 2\zeta$ and $\eta = \pi - 2\zeta$, one gets:

$$dF_{z'} = \frac{n_m}{c}\mathrm{Re}\left\{1 + Re^{2i\xi} - T^2\frac{e^{2i(\xi-\zeta)}}{e^{2l\alpha\cos\zeta} + Re^{-2i\zeta}}\right\}dP. \tag{3.6}$$

In turn, along y'-axis, we have that:

$$dF_{y'} = \frac{n_m}{c}\Big\{R\sin(2\xi) - T^2\sum_{n=0}^{+\infty} R^n\Big[e^{-2l\alpha\cos\zeta}\Big]^{n+1}\sin\left(\nu + n\eta\right)\Big\}dP. \tag{3.7}$$

Proceeding in an analogous way, one gets:

$$dF_{y'} = \frac{n_m}{c}\mathrm{Im}\Big\{Re^{2i\xi} - T^2\frac{e^{2i(\xi-\zeta)}}{e^{2l\alpha\cos\zeta} + Re^{-2i\zeta}}\Big\}dP. \tag{3.8}$$

Note that the compact expression (3.1) is equivalent to Eqs. (3.6) and (3.8).

Appendix B

Consider an optical tweezers made of a highly focused laser beam, whose intensity is modulated as a Gaussian profile. Let the z-axis be placed along the optical axis, pointing toward the objective lens (Fig. 3.9-a)). If we choose the origin of the coordinate system to be at the laser focus, it is well-known that power increment dP of a single light ray can be written as [18]:

$$dP = \frac{2P_t}{\pi\sigma^2}\exp\left(\frac{-2f^2\sin^2\theta}{\sigma^2}\right)f^2\sin\theta\cos\theta d\theta d\phi, \tag{3.9}$$

where θ is the angle between the light ray and the optical axis of the Gaussian beam, and ϕ is the usual azimuthal angle. The limits of integration for θ and ϕ will be discussed in details below. P_t is the total power before the laser enters the objective, σ is the beam waist, and f is the focal length.

Fig. 3.9-a) depicts the spherical particle (radius l) at a distance z below the focal plane, at position $\vec{r}$. The vector $\vec{d}$ represents the position where the incoming light ray reaches its surface. The x-z plane was chosen to cross the center of the sphere, and γ is the angle between $\vec{r}$ and the optical axis. Let ρ be the radial distance from the optical axis to the geometric center of the sphere.

Writing $\hat{y}'$, $\hat{z}'$, and all the variables as functions of θ and ϕ, and integrating Eq. (3.1), one obtains the total radiative force exerted on the bead by all light rays reaching

its surface. The vectors $\vec{r}$ and $\vec{d}$ can be written as [18]:

$$\begin{aligned}\vec{r} &= r(\sin\gamma, 0, \cos\gamma),\\ \vec{d} &= d(\sin\theta\cos\phi, \sin\theta\sin\phi, \cos\theta),\end{aligned} \tag{3.10}$$

where

$$d = \sqrt{l^2 - r^2 + r^2(\sin\gamma\sin\theta\cos\phi + \cos\gamma\cos\theta)^2} + r(\sin\gamma\sin\theta\cos\phi + \cos\gamma\cos\theta). \tag{3.11}$$

The ξ angle can be written as

$$\xi = \arccos\left(\frac{d^2 + l^2 - r^2}{2ld}\right). \tag{3.12}$$

The unitary vectors $\hat{z}'$ and $\hat{y}'$ are given by:

$$\begin{aligned}\hat{z}' &= (-\sin\theta\cos\phi, -\sin\theta\sin\phi, -\cos\theta),\\ \hat{y}' &= \frac{\hat{z}' \times (\vec{r} \times \hat{z}')}{|\hat{z}' \times (\vec{r} \times \hat{z}')|}.\end{aligned} \tag{3.13}$$

Note that only a portion of the light rays leaving the objective lens actually reaches the sphere, whenever it is placed out of the focus of the laser beam. The limits of integration for θ are given by (see Fig. 3.9-b)):

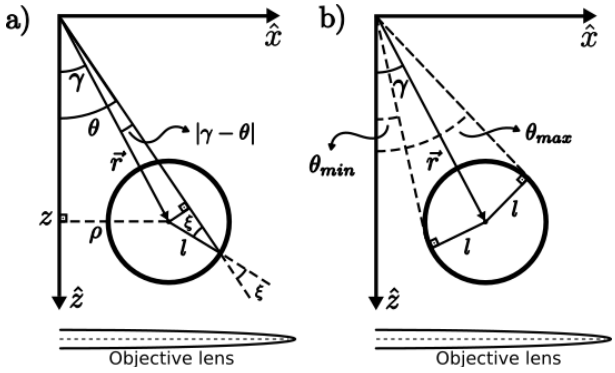

Figure 3.9: a) Spherical particle placed out of the focus, along with the definition of the coordinate system. See text for details. Fig. b) illustrates the fact that only those rays between $\theta_{min} = \text{Max}[0, \gamma - \arcsin(l/r)]$ and $\theta_{max} = \gamma + \arcsin(l/r)$ reach the sphere. Adapted from Ref. [7].

$$\begin{aligned}\theta_{min} &= \text{Max}[0, \gamma - \arcsin(l/r)],\\ \theta_{max} &= \text{Min}[\theta_0, \gamma + \arcsin(l/r)],\end{aligned} \tag{3.14}$$

where θ_0 is the critical angle for the glass-medium interface at the coverslip ($\theta_0 = 1.109$ rad for glass-water interface [18]).

To determine the limits of integration for ϕ, notice that they correspond to the situations where the light rays are tangent to the surface of the bead (Fig. 3.10-a)). This defines a curve at the surface, whose equation can be obtained by subjecting the equation

of the sphere to the constraint $d = d_0 \equiv d(\theta = \gamma + \arcsin(l/r), \phi = 0)$. Therefore, this curve must satisfy $(x - x_0)^2 + (y - y_0)^2 + (z - z_0)^2 = l^2$, where (see Fig. 3.10-b)):

$$\begin{cases} x = d_0 \sin\theta \cos\phi, & x_0 = r \sin\gamma, \\ y = d_0 \sin\theta \sin\phi, & y_0 = 0, \\ z = d_0 \cos\theta, & z_0 = r \cos\gamma. \end{cases} \tag{3.15}$$

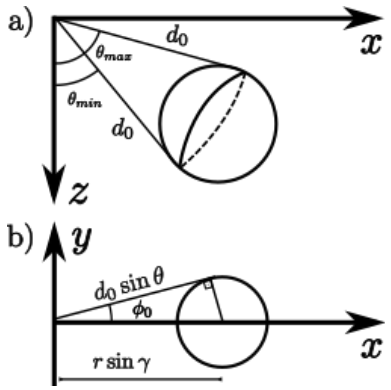

Figure 3.10: Illustration of the procedure used to calculate the limits of integration for ϕ. In a) one sees the curve on the surface of the sphere corresponding to the tangent angles of incidence. The rays tangency the sphere at a fixed distance d_0 from the origin for all values of $\phi_0(\theta)$. b) shows a cross-section parallel to the focal plane, with the coordinates of a tangent ray, together with the limit of integration for the azimuthal angle, ϕ_0. Adapted from Ref. [7].

As a result, $\phi_{min}(\theta) = -\phi_0(\theta)$ and $\phi_{max}(\theta) = \phi_0(\theta)$, where

$$\phi_0(\theta) = \arccos\left[\left(\frac{d_0^2 + r^2 - l^2}{2rd_0} - \cos\theta\cos\gamma\right)\csc\theta\csc\gamma\right]. \tag{3.16}$$

This is valid when $\rho > l$, and the z-axis does not intercept the sphere. However, if $\rho < l$, one needs to be more careful with the limits of integration. Fig. 3.11 shows a cross section parallel to the focal plane in such case. For $0 < \theta < |\gamma - \arcsin(l/r)|$ (region 1), we have $-\pi \leq \phi \leq \pi$, while for $\theta > |\gamma - \arcsin(l/r)|$ (region 2) we have $-\phi_0(\theta) < \phi < \phi_0(\theta)$. Therefore, in this case

$$\phi_{max} = \begin{cases} \pi\,, & 0 < \theta < |\gamma - \arcsin(l/r)| \\ \phi_0(\theta)\,, & |\gamma - \arcsin(l/r)| < \theta < \theta_{max}. \end{cases} \tag{3.17}$$

It is easy to see that $\phi_{min} = -\phi_{max}$.

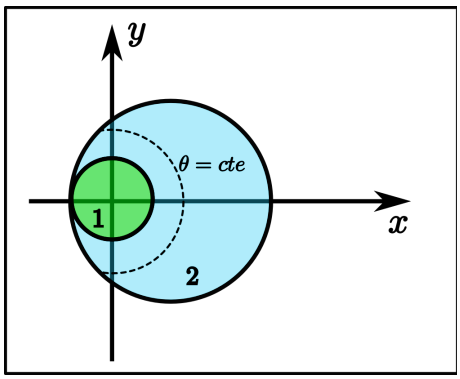

Figure 3.11: Cross-section parallel to the focal plane for the situation where $\rho < l$. If $\theta < |\gamma - \arcsin(l/r)|$ (region 1-green), the light ray crosses the sphere for all values of ϕ. However, if $\theta > |\gamma - \arcsin(l/r)|$ (region 2-blue), only those rays parametrized by $\phi \in [-\phi_0, \phi_0]$ cross the sphere. Adapted from Ref. [7].

Chapter 4

Germanium microparticles as optically induced oscillators

In this chapter we discuss our results reported in Ref. [8] [Adapted from (W. H. Campos, T. A. Moura, O. J. B. J. Marques et. al., "Germanium microparticles as optically induced oscillators in optical tweezers," *Physical Review Research* **1**(3), 033119 (2019). `https://doi.org/10.1103/PhysRevResearch.1.033119`). Published by the American Physical Society under the terms of the Creative Commons Attribution 4.0 International (CC BY 4.0) license][1], regarding the trapping of germanium (Ge) spherical particles under a Gaussian laser beam optical tweezers. We show that Germanium semiconductor beads behave as optically induced oscillators when subjected to a highly focused laser beam. Such unusual motion is due to the competition between the usual optical forces and the radiometric force related to thermal effects, as discussed for topological insulator particles in Chapter 2. Actually, the behavior of Ge particles present an additional attribute, their direction of oscillation highly depends on the polarization of the laser beam, i.e. the particles oscillate perpendicularly to the direction of the light polarization. Also, vertical oscillations were observed to take place, as predicted in Ref. [7] (see Section 3.4). We characterize the behavior of the Germanium beads in detail and propose a modification on the effective model developed in Ref. [1] in order to account for the new results, which have shown a good agreement with the experimental data. Such kind of system

[1] According to the CC BY 4.0 license's website (`https://creativecommons.org/licenses/by/4.0/`) and the "Reuse & permissions" information in the article's webpage, this license permits unrestricted use or adaptation, provided appropriate credit and citation are given, as well as indications if changes were made and a link to the license's website.

can potentially revolutionize the field of optical manipulation, contributing to the design of single molecule machines and to the application of oscillatory forces in fundamental physics, cellular manipulation, fluid dynamics, and other soft matter systems.

Over 100 years after its discovery, Germanium (Ge) is one of the most important and well-characterized materials used in the manufacture of micro and nano devices, and continues to attract tremendous attention in different areas of condensed matter physics and materials science. Although nowadays silicon dominates the semiconductor electronics, in the initial years, the solid-state industry were almost exclusively based on germanium diode and bipolar-junction-transistor technology. Recently, germanium devices have being considered as a possible high-mobility substitute for the silicon MOSFET technology, since germanium has the highest hole mobility of all the known semiconductor materials [210]. Due to its suppression of spin relaxation, the group IV semiconductors, such as Ge and Si, has aroused interest in timely research branches, like spintronics [211–215]. Furthermore, compared with Si, Ge possesses a much higher carrier mobility [214]. In this way, the solid-state device research community is returning to investigate the high-mobility Germanium to improve the performance of transistors based on this material [215]. Nowadays, Ge has application in optical fibers, polymerization catalysts, and Si-Ge alloys in microchip manufacturing, with feature sizes on the chips reaching 7 nm ($<$ 60 Ge atomic layers) [215, 216]. However, to our best knowledge, the trapping of Ge microparticles in OT has not been investigated so far.

For $\lambda = 1064\,\mathrm{nm}$ (wavelength used in our experiments), Ge has a relatively high refractive index, $n \approx 4.41$, and an extinction coefficient of $k = 0.11$ [217]. This value for the refractive index is comparable to that of Bi_2Te_3 topological insulators. In Chapter 3, we also show that the radiative force on a particle is significantly influenced by absorption of light, mainly when the skin depth is comparable to the particle size. The extinction coefficient of Ge leads to an absorption coefficient of $\alpha = 1.30\,\mu\mathrm{m}^{-1}$. As this corresponds to a skin depth of $\delta = 0.77\,\mu\mathrm{m}$, we should expect interesting effects when subjecting microscopic Ge particles under an optical tweezers setup. For more details on the optical properties of germanium and other semi-conductors materials, we refer to Ref. [204].

Surprisingly, Ge beads are observed to oscillate in a plane perpendicular to the optical axis with relatively well-defined amplitude and frequency controllable by the laser power. Fig. 4.1(a) shows our experimental setup, in which the particles are located

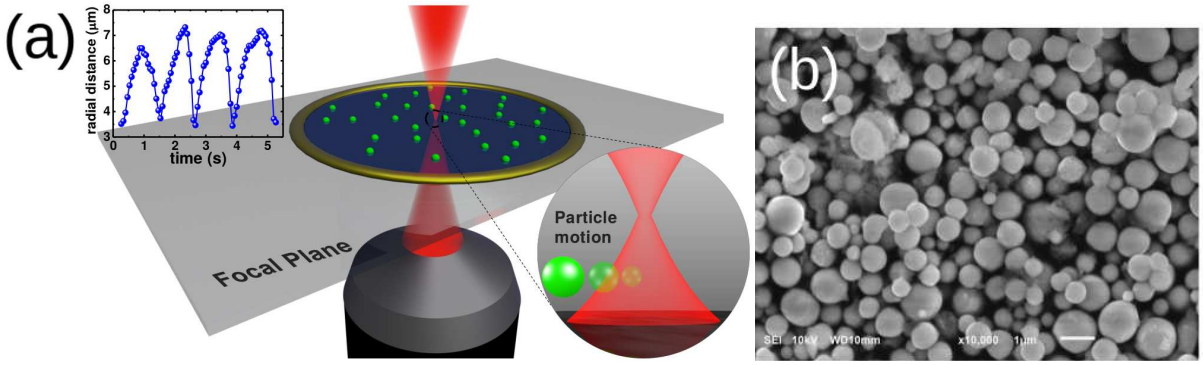

Figure 4.1: (a) Experimental setup yielding the optically induced oscillations of Ge microspheres. The beads are suspended in deionized water and subjected to a Gaussian laser beam OT. The sample chamber consists of an *o-ring* glued in a microscope coverslip. We have observed that, after placing the beads in the sample chamber with deionized water, they remain suspended around $4\,\mu$m above the coverslip surface, before and during the laser incidence. The inset shows the radial displacement of a bead, relative to the optical axis of the laser. (b) Scanning electron microscopy (SEM) of Ge microspheres obtained by the laser ablation technique. The particles present a well-defined spherical shape with smooth and homogeneous surface. Adapted from Ref. [8].

around $z \sim -5\,\mu$m below the focal plane. The position of a $3\,\mu$m diameter Ge particle relative to the optical axis as function of time is shown in the inset, illustrating their typical oscillatory dynamics. In addition, we show that laser polarization can be used to easily guide the oscillations to a preferential direction, an appealing feature for practical applications. Such an oscillatory motion has the potential of extending usual OT setup capabilities for investigating dynamical properties of macromolecules and small systems, like DNA molecules and biological membranes.

4.1 Objectives

We are interested in studying the oscillatory behavior of germanium microparticles under a Gaussian laser beam optical tweezers. For this, we should investigate how some dynamical quantities, such as the amplitude and frequency of oscillations, depend on the power of the laser beam. We are also interested in providing an effective theoretical description for the additional effects observed on this system, say, dependence of the direction of oscillations with the polarization of the laser beam.

4.2 Materials and methods

4.2.1 Synthesis and characterization of the Ge microparticles

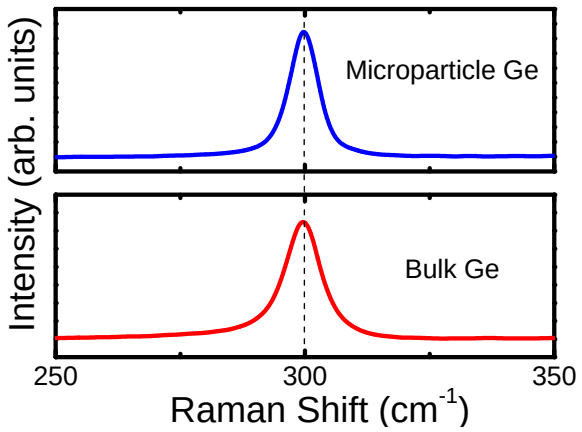

Figure 4.2: Representative Raman spectra acquired from the Ge-bulk (red color) and a Ge-microparticle (blue color), highlighting the fundamental unstrained Ge Raman line at $\sim 300\ cm^{-1}$, which corresponds to the bulk Ge phonon mode. The Raman spectra indicates that the particles did not experience chemical changes during the synthesis process. Adapted from Ref. [8].

The microparticles of Ge were synthesized by pulsed laser ablation technique in liquid solution. Pulsed laser ablation in liquids (PLAL) was carried out in a Nd:YAG laser Quantel, model Brilliant B. The laser light used for the ablation was the second harmonic wave ($\lambda = 532$ nm) with a pulse energy of 70 mJ and 10 Hz in the nanosecond regime. The experimental set up used to synthesize the micro particles consists of using Ge-crystals (99,999%) as a target material immersed in 10 ml of distilled water as a working liquid for ablation. The target was ultrasonically cleaned in distilled water before the process and placed at the bottom of a beaker. The laser beam was focused onto the germanium surface under a liquid layer of approximately 10 mm thick with a spot size of about 1 mm in diameter using focal lens of 50 mm. The target was moved perpendicularly to the laser beam during 5 minutes to irradiate fresh surfaces during the whole process. The experiments were conducted at room temperature (~ 295 K) and pressure of 1 atm.

The high quality of the Ge microparticles was confirmed by Scanning Electron Microscope (SEM) [see Fig. 4.1(b)] and Raman spectroscopy analysis has proven that our Ge-beads maintained their chemical structure during the laser ablation process (Fig. 4.2). Additional characterizations by energy dispersive X-ray (EDX) analysis have also

demonstrated that the synthesized particles have no impurities in their composition.

4.2.2 Optical tweezers setup

The OT consists of a 1064 nm ytterbium-doped fiber laser (IPG Photonics) operating in the TEM_{00} mode, mounted on a Nikon Ti-S inverted microscope with a 100× NA 1.4 objective. We have set the laser power at 37 mW, measured at the objective entrance. The sample chamber consists of an o-ring glued in a microscope coverslip.

4.2.3 Experimental procedures and data analysis to obtain the forces

For the optical experiment, we have selected those particles with well-defined spherical shape. The individual motion of each Ge microparticle for various oscillation cycles was recorded using videomicroscopy. We have used a CCD camera (JAI BM-500GE) with a recording rate of 15 frames per second and a resolution of 29 pixels/μm. An exemplifying video showing the typical dynamics of a 3 μm diameter Ge-microsphere under linearly polarized Gaussian laser beam optical tweezers can be found as a supplemental file of Ref. [8]. Fig. 4.3 shows successive frames of the video, along with a number of features of the particle oscillatory motion. From the video it is evident that whenever a Ge particle is placed near the optical region, it is naturally impelled to oscillate in a preferential direction, i.e. perpendicular to the light polarization [Fig. 4.3(b)]. The video also shows that the Ge microparticles used in our experiments present a very good spherical shape, justifying the use of the laser ablation technique.

The videos were analyzed using the ImageJ software, which allows us to obtain the coordinates of the particle centroid as a function of time. The optical axis position, (x_0, y_0), can be obtained by trapping a dielectric particle and taking the time average of its coordinates. Then, the radial position of the particle relative to the optical axis can be calculated by $\rho = \sqrt{(x - x_0)^2 + (y - y_0)^2}$. The velocity (acceleration) necessary to determine the Stokes (resultant) force is calculated by taking the first (second) order time derivative of the particle position. In order to compare the experimental results with the theoretical model accounting for radiometric and radiative forces, one has to subtract the contribution from the Stokes force:

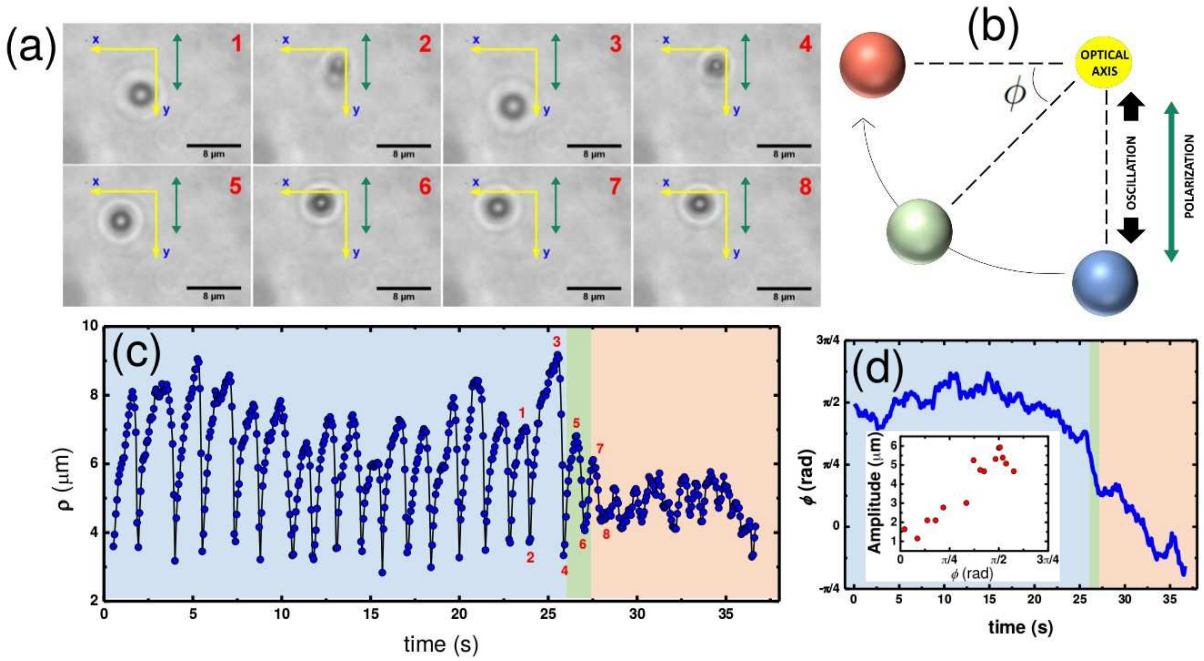

Figure 4.3: Ge microparticle of 3.1 μm diameter under a linearly polarized Gaussian laser beam OT. (a) Successive video frames showing the microsphere oscillating toward the optical axis (origin of the coordinate frame). (b) Direction of light polarization (green arrow), along with the definition of the azimuthal angle, ϕ. (c) Radial displacement of the particle, ρ, as function of time. The blue (red) background indicates oscillations along the y-axis (x-axis), while the green background points out the transient from one axis to the other. This typical oscillatory dynamics indicated by the numbers in red correspond to the frames shown in (a). (d) How the azimuthal angle, ϕ, varies in time. The inset shows the amplitude of the oscillations vs. ϕ. Adapted from Ref. [8].

$$\vec{F} = \vec{F}_{res} - \vec{F}_S, \tag{4.1}$$

where $\vec{F}_S = -6\pi\eta a\frac{d\vec{r}}{dt}$ and $\vec{F}_{res} = \frac{4}{3}\pi a^3\rho_{Ge}\frac{d^2\vec{r}}{dt^2}$ are the Stokes and resultant forces, respectively. η is the medium viscosity (we have used deionized water, $\eta = 8.9 \times 10^{-4}$ Pa.s), a is the particle radius and $\rho_{Ge} \approx 5323$ kg/m^3 is the Germanium density.

The period of oscillation can be estimated by taking the time difference between two consecutive minimum (or maximum) displacements from the optical axis. In turn, the amplitude of oscillation is defined as the distance between the minimum and the maximum radial displacement of a given cycle.

4.3 Results and discussions

Let us define a cylindrical coordinate system whose origin is at the laser beam focus, say, $x_0 = y_0 = 0$ [see Fig. 4.3(a-b)]. The z-axis is taken along the optical axis, pointing in the direction of the laser propagation. We take the y-axis along the polarization direction, and the x-axis defined by the right-hand rule. As usual, the position of the particle is represented by $\vec{r} = (\rho, \phi, z)$, where ρ is the radial distance between the particle and the optical axis, while ϕ is the azimuthal angle, measured relative to the x-axis. How the particle radial distance, $\rho(x, y) = \sqrt{x^2 + y^2}$, varies over time is plotted in Fig. 4.3(c). Notice that the particle is initially in a position parallel to the light polarization, say, along y-axis ($\phi = \pi/2$), where it begins to oscillate toward the optical axis. However, the oscillation direction changes with time, eventually reaching a direction perpendicular to the polarization axis, as shown in Fig. 4.3(d). Once there, the oscillatory direction is relatively stable around the x-axis ($\phi = 0, \pi$). The amplitude of oscillation appears to increase linearly with the azimuthal angle, ϕ, in the range of $[0, \pi/2]$ [see inset of Fig. 4.3(d)]. In addition, the diffraction pattern of the microparticle changes periodically in time [see Video.avi in Ref. [8] and Fig. 4.3(a)], indicating that it is also subject to oscillations along the direction of the laser propagation, a behavior predicted in Ref. [7].

4.3.1 Theoretical model

As briefly mentioned before, the oscillatory dynamics of semi-transparent particles in optical tweezers results from a delicate balance between optical (gradient force and radiation pressure) and radiometric forces [9]. The former is related to linear momentum transfer from the light beam to the particle and it has been extensively investigated in the last decades [2–6, 18]. In turn, the radiometric force comes as a consequence of the temperature gradient induced on the surrounding medium, due to inhomogeneous heating of the particle, repelling it from the focal region. A satisfactory microscopic model describing this effect in a Gaussian laser beam optical tweezers is still lacking.

In Ref. [6], the authors extended the Mie-Debye spherical aberration theory to linearly polarized optical tweezers. They have shown that linear polarization introduces strong axial asymmetry on the optical force due to Mie resonance effects. In other words, the components of the force acquire a sinusoidal dependence on ϕ. These effects become

particularly important when the lateral displacement is of the order of the particle radius. The components of the optical force in a linearly polarized Gaussian laser beam optical tweezers read [6]:

$$\begin{cases} F_j(\rho,\phi,z) = \mathcal{F}'_j(\rho,z) - \mathcal{F}''_j(\rho,z)\cos(2\phi), \qquad j=\rho,z \\ F_\phi(\rho,\phi,z) = -\mathcal{F}_\phi(\rho,z)\sin(2\phi). \end{cases} \tag{4.2}$$

The functions $\mathcal{F}'_j$ and $\mathcal{F}''_j$ take a factor proportional to the laser intensity [6]:

$$I(\vec{r}) = I_0(z)\exp\left(\frac{-2\rho^2}{w(z)^2}\right), \tag{4.3}$$

where $I_0(z)$ is the intensity at the optical axis, for a height z above the focal plane. $w(z) = w_0\sqrt{1+(z/z_R)^2}$ is the beam waist for a given value of z, with $z_R = \pi w_0^2/\lambda$. w_0 is the beam waist at the focal plane, and λ is the laser wavelength.

In order to incorporate these results into the effective model proposed in Ref. [9], $\mathcal{F}'_j$ and $\mathcal{F}''_j$ $(j=\rho,z)$ are taken proportional to $\partial_j I(\vec{r})$. Therefore, the radial component of the gradient force reads:

$$F_{G\rho} = -\frac{2\rho\mathcal{F}_{G\rho}\exp(1/2)}{w(z)(1+\eta_\rho)}\exp\left(\frac{-2\rho^2}{w(z)^2}\right)(1-\eta_\rho\cos 2\phi). \tag{4.4}$$

$\mathcal{F}_{G\rho}$ is the maximum magnitude of $F_{G\rho}$ for a given value of z, which occurs at $\rho = w(z)/2$, and $\phi = \pm\pi/2$. η_ρ is a parameter that accounts for the relative strength of the asymmetric term. An analogous calculation for the z-component gives:

$$F_{Gz} = \frac{2e\mathcal{F}_{Gz}\rho^2}{w(z)^2(1+\eta_z)}\exp\left(\frac{-2\rho^2}{w(z)^2}\right)(1-\eta_z\cos 2\phi). \tag{4.5}$$

The maximum magnitude of F_{Gz}, $\mathcal{F}_{Gz}$, occurs at $\rho = w(z)/\sqrt{2}$ and $\phi = \pm\pi/2$. e is the Euler's number and η_z accounts for the relative strength of the asymmetric term. Finally, Mie scattering theory also predicts a component of the force along $\hat{\phi}$ [6]:

$$F_{G\phi} = -\frac{2\rho\mathcal{F}_{G\phi}\exp(1/2)}{w(z)}\exp\left(\frac{-2\rho^2}{w(z)^2}\right)\sin 2\phi. \tag{4.6}$$

$\mathcal{F}_{G\phi}$ is the maximum magnitude of $F_{G\phi}$, occurring at $\rho = w(z)/2$ and $\phi = n\pi/4, n = \pm1, \pm3, \pm5, \pm7$.

The radiometric force is related to the temperature gradient caused by inhomo-

geneous heating of the particle and its surrounding medium. Such effect is in order due to the spatially-varying intensity profile of the laser beam, which causes the hemisphere facing the optical axis to be heated more than the opposite side. Because heating is a consequence of light absorption, it is present whenever the extinction coefficient of the particle material is non-zero in the wavelength of the microscope ($\lambda = 1064$ nm, in our experiments), which is often the case for most metals and semi-conductor materials [1,2]. Developing a microscopic model for the radiometric force is challenging, but for the purpose of this work it suffices to consider it proportional to the intensity of the laser beam [1,4]:

$$\vec{F}_R = F_{R\rho}\hat{\rho} + F_{Rz}\hat{z} = (\mathcal{F}_{R\rho}\hat{\rho} + \mathcal{F}_{Rz}\hat{z}) \exp\left(\frac{-2\rho^2}{w(z)^2}\right). \tag{4.7}$$

Therefore, the resultant force exerted on the particle (after subtraction of the Stokes force), $\vec{F} = \vec{F}_R + \vec{F}_G$, reads:

$$\begin{aligned}\vec{F} = \Bigg\{ & \left[\mathcal{F}_{R\rho} - \frac{2\rho\mathcal{F}_{G\rho}\exp(1/2)}{w(z)(1+\eta_\rho)}\left(1 - \eta_\rho\cos 2\phi\right)\right]\hat{\rho} \\ & + \left[\mathcal{F}_{Rz} + \frac{2e\mathcal{F}_{Gz}\rho^2}{w(z)^2(1+\eta_z)}\left(1 - \eta_z\cos 2\phi\right)\right]\hat{z} \\ & - \frac{2\rho\mathcal{F}_{G\phi}\exp(1/2)}{w(z)}(\sin 2\phi)\hat{\phi}\Bigg\} \exp\left(\frac{-2\rho^2}{w(z)^2}\right).\end{aligned} \tag{4.8}$$

While the radiometric force and radiation pressure tend to push the particle away, gradient force works as a restoring action towards the laser beam focus. Depending on the optical properties of the material from which the particle is made, three main scenarios emerge: 1) Radiometric force dominates: as occurs to metallic beads, large absorption of the incident light results in inhomogeneous heating of the medium and the particles are drifted away; 2) Suitable conditions favoring optical trapping are accomplished: for example, a dielectric microsphere in which absorption and reflection of light are negligible and gradient force dominates; 3) Special situation takes place whenever both of such forces have comparable magnitudes: the competition between them may yield oscillatory motion, as we have observed to occur with Ge-microspheres. Actually, similar oscillations also happen with topological insulator Bi_2Te_3 and Bi_2Se_3 beads [1]. Once such a kind of compounds share some electrical and optical properties with semiconductors,

we may wonder whether optically induced oscillatory motion is the typical dynamics of semiconductor beads under the action of focused laser light, as commonly used in OT setup.

4.3.2 Comparison between theory and experiments

We now proceed with the discussion of a very important aspect of this effective model. In the real experiments, the local temperature in all points of the system is constantly varying, heating up and cooling down as the particle oscillates. For example, as the particle approaches the optical axis, its temperature rapidly increases due to light absorption. When the radiometric force overcomes the gradient force, the particle is pushed away towards the outermost region of the beam. During its removal the particle cools down, as heat is transferred to the surrounding medium. Thermal equilibrium is achieved when the particle is far from the optical axis, then the cycle restarts. A precise description beyond our effective model is much more involved, once the physical parameters comprised in the resultant force, Eq. (4.8), are expected to bear complicated dependence on the microsphere and medium optical properties at each time instant. Therefore, as the forces depend on the refractive index, extinction coefficient and other temperature sensitive properties, one *should not* expect the parameters of the model to be constant along all the oscillation cycle. An exception would be w_0, which is a characteristic of the laser beam [1]. In order to simplify our analysis, we can consider the effective values of the model parameters ($\mathcal{F}_{G\rho}$, $\mathcal{F}_{R\rho}$, etc) to be static, as long as we separate each cycle into two regimes: *Approach* and *removal*.

Approach regime refers to the time interval in which the particle is moving toward the optical axis [e.g. from 1 to 2 in Fig. 4.3(c)]. The particle is initially at the outermost part of the optical region, in thermal equilibrium with the solution. The gradient force attracts the particle toward the optical axis and heating generates a radiometric force that opposes to the trapping. Fig. 4.4(a) shows a vector plot of the resultant force in the approach regime, at a cross-section of height $z = -0.5\,\mu$m below the focal plane (see caption for parameters). The color bar represents the subtraction $F_z - w$, where $\vec{w}$ is the apparent weight of the particle. The vector plot shows *red* arrows for $F_z - w > 0$ and *blue* arrows for $F_z - w < 0$, which explains the small deviations from the oscillation plane that can be seen in the videos. The strong axial asymmetry induced by the polarization

is evident, and the particle tends to oscillate in a preferential direction, i.e. the x-axis. Notice that there are two "stable" points along this direction, so that the particle will be eventually attracted to one of them. However, for a particle initially placed at the y-axis,

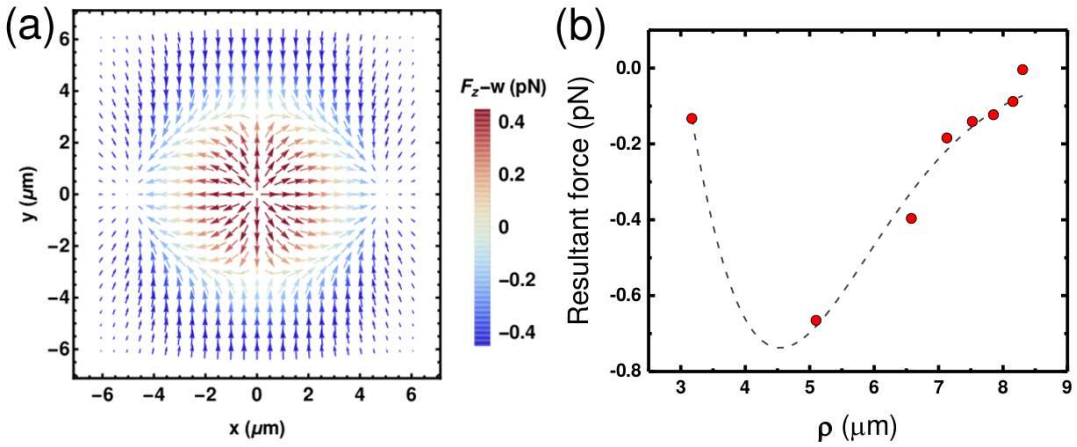

Figure 4.4: (a) Typical vector plot of the resultant force, [Eq. (4.8)], in the approach regime. We have taken the following numeric values for the parameters: $w(z) = 5.2\,\mu$m, $\mathcal{F}_{G\rho} = 3.5\,$pN, $\mathcal{F}_{G\phi} = 0.7\,$pN, $\eta_\rho = 0.22$, $\mathcal{F}_{R\rho} = 7.0\,$pN, $\mathcal{F}_{Rz} = 1.3\,$pN and $\eta_z = 0.1$. The in-plane vectors where plotted using the x and y components of the resultant force, while the color bar represents the total force along z-direction, $F_z - \mathrm{w}$, where $\vec{\mathrm{w}} = -(4/3)\pi a^3(\rho_{Ge} - \rho_m)g\hat{z}$ is the apparent weight of the particle [7]. $F_z - \mathrm{w} > 0$ for red vectors, while blue ones stand for $F_z - \mathrm{w} < 0$. $a \approx 1.55\,\mu$m is the sphere radius, $g = 9.8\mathrm{m/s}^2$ is the acceleration of gravity, $\rho_{Ge} = 5323\,\mathrm{kg/m}^3$ and $\rho_m = 997\,\mathrm{kg/m}^3$ are the Ge and medium (deionized water) densities, respectively. (b) Fitting of the radial component of the resultant force, [Eq. (4.8)], to experimental data in the approach regime. Red dots are experimental data extracted from the third oscillatory cycle in Fig. 4.3(c), which takes place mostly along the polarization direction (y-axis, in which the azimuthal component, F_ϕ, is negligible). The dotted line is the fitting of the radial component of the resultant force with data from the approach regime. The fitting parameters along with their standard errors read as: $\mathcal{F}_{R\rho} = (7.0 \pm 1.4)\,$pN, $\mathcal{F}_{Rg} = (3.59 \pm 0.56)\,$pN and $w(z) = (5.20 \pm 0.18)\,\mu$m. Adapted from Ref. [8].

the time required for it to reach a stable point is longer than the oscillation period, so that it performs a few oscillations before displacing to the x-axis. Along this direction the amplitude of the oscillations decreases whenever compared to the y-axis (notice the smaller modulus of the resultant force vectors), by virtue of the polarization effect. Fig. 4.4(b) shows the radial component of the resultant force, F_ρ, as function of the radial position, ρ, for the approach regime of the third oscillatory cycle in Fig. 4.3(c). The dashed line represents a theoretical fitting of F_ρ [Eq. (4.8)] with experimental data. Among the fitting parameters, we have $w(z \approx -5\,\mu\mathrm{m}) = (5.20 \pm 0.18)\,\mu$m. From $w(z)$, the experimental parameter $w_{0-exp} = (0.327 \pm 0.011)\,\mu$m is readily obtained, whose value

is in good agreement with its theoretical counterpart $w_0 = 0.36\,\mu$m. [Taking the average over many cycles, we have obtained $\langle w_{0-exp} \rangle = (0.31 \pm 0.02)\,\mu$m]. The good fitting and the small error bars suggest that the approximation of static parameters works well for the approach regime. As the particle moves toward the region of higher intensity, the temperature increases very fast around a particular distance to the optical axis. As a consequence, radiometric force overcomes the gradient and the transition to the removal regime takes place very abruptly, resulting sharp peaks in the particle position evolution at the points of minimum radial distance [$\rho \sim 3\,\mu$m in Fig. 4.3(c)].

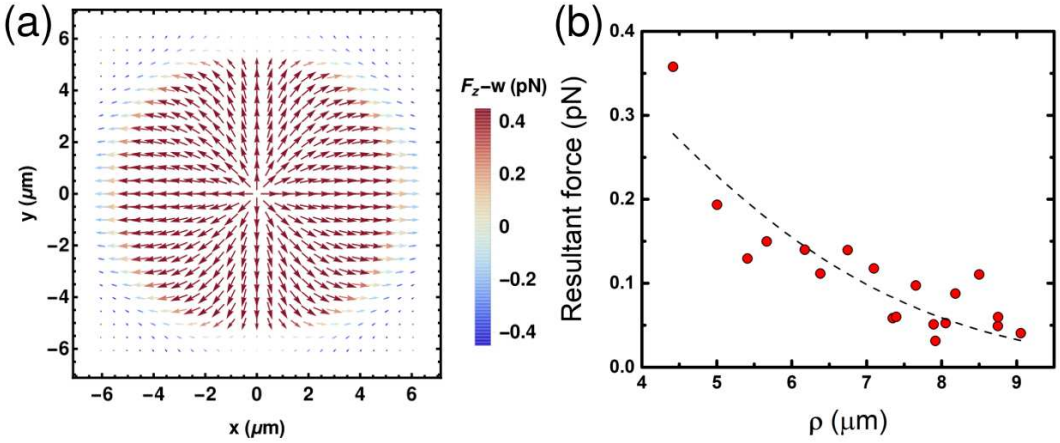

Figure 4.5: (a) Typical vector plot of the resultant force [Eq. 4.8] in the removal regime. The values of the parameters for the gradient force are the same as those used to generate Fig. 4.4(a). For the radiometric force, we have taken $\mathcal{F}_{R\rho} = 13\,$pN and $\mathcal{F}_{Rz} = 7.3\,$pN. It is clear from the plot that the radiometric force overcomes the gradient force along all removal of the particle, until it approaches the outermost part of the optical region and reaches thermal equilibrium with the surrounding medium. (b) Fitting of the radial component of the resultant force [Eq. (4.8)] to experimental data, in the removal regime. As the behavior of the experimental data points is much simpler than the general behavior of Eq. (4.8), the fitting return parameters with large error bars. Adapted from Ref. [8].

Removal regime refers to the time interval in which the particle is moving away from the optical axis [e.g. from 2 to 3 in Fig. 4.3(c)]. The particle is initially at minimum radial distance and repulsive radiometric force dominates. Due to the high temperature gradient, the radiometric force is at its maximum, and repels the particle away from the optical axis. The radiometric force overcomes the gradient force along all the removal regime, until the particle reaches the outermost part of the optical region. Other effects can also contribute to repel the particle from the optical axis. We can cite for example the increase of radiation pressure due to particle heating, which changes the effective number of charge carriers in the semiconductor particle, and a possible inversion in the direction of

the gradient force that can occur due to changes on the dielectric constant of the particles, which occurs also due to heating [72, 218]. At the end of this regime, the particle cools down until it reaches thermal equilibrium with the solution at the point of maximum distance. Thus, smooth transition to the approach regime takes place, restarting the cycle with the gradient force dominating the dynamics. Fig. 4.5(a) shows a vector plot of the resultant force in the removal regime and Fig. 4.5(b) shows the fitting of the radial component of the resultant force, Eq. (4.8), to the experimental data for the removal regime. The oscillation cycle chosen to extract this data is the same as for Fig. 4.4(b). Although the model visually fits the experimental data, we must be attentive to the large error bars obtained from the fitting. The simpler behavior of the experimental data, compared to the general form of Eq. (4.8), results in too much freedom for the values extracted from the fitting. Therefore, the approximation of static parameters is not very accurate for the removal regime.

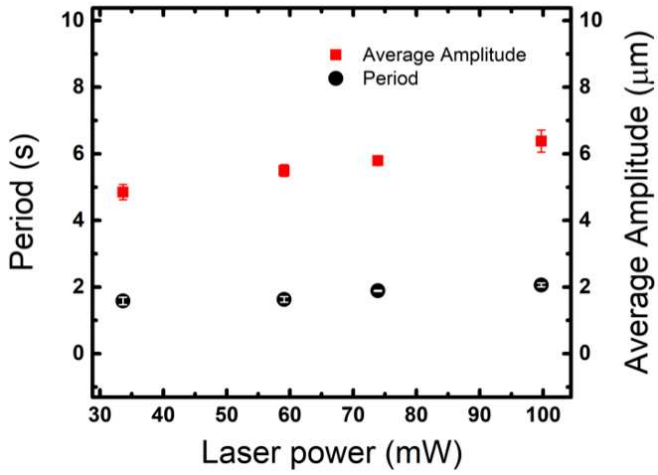

Figure 4.6: Period (black dots) and amplitude (red squares) of oscillation for different laser power. Vertical bars are standard errors over averages. Adapted from Ref. [8].

An animated image showing the dynamics of the resultant force field [Eq. (4.8)] is available as a supplemental file in Ref. [8]. To generate the animation, we have manually set the values of $\mathcal{F}_{R\rho}$ and $\mathcal{F}_{Rz}$ for each frame, while the parameters of the gradient force were kept constant [the same used to generate Fig. 4.4(a)]. Therefore, it should not be interpreted as a simulation, but rather as an illustration of the effective model.

We have also observed that fundamental control over period and amplitude of oscillations can be achieved by tuning laser power (see Fig. 4.6). These observations constitute a very robust experimental result, measured also for other similar particles

(see for example Ref. [1]).

4.3.3 Single particle thermal machine

We believe that the opto-thermal oscillations of the Ge microparticles constitute a very rich scenario for the experimental realization of a single particle thermal machine (microscopic engine) [219–221]. It has been recently reported the realization of a Brownian Carnot engine in which the working substance is a single polystyrene colloidal particle trapped in an OT [222]. However, important features make thermal machines with Ge particles a promising alternative. 1) Robust dynamics: it depends only on the optical properties of the particles and the medium. No external perturbation is necessary in order to achieve a thermodynamic cycle. 2) Injection of heat takes place via absorption of light, so the laser beam itself plays the role of the hot bath. A significant amount of energy that is usually wasted in conventional traps is converted into work in such system. 3) The large amplitude of oscillations is exceptionally appealing when it comes to practical applications of a thermal machine, such as exerting dynamic forces on polymers and other microscopic objects.

We may estimate the work done by cycle, $\mathcal{W} = \int_{\text{cycle}} \vec{F} \cdot d\vec{l}$, and the efficiency, η_{eff}, of our Ge-microsphere faced as an opto-mechanical engine. For that, let us recall that the forces $\vec{F}_G$ and $\vec{F}_R$ have components with magnitudes varying from $\mathcal{F}_{G\phi} = 0.7\,\text{pN}$ to $\mathcal{F}_{R\rho} = 7.0\,\text{pN}$ (see caption from Fig. 4.4 for details). Larger amplitude particle oscillations, Fig. 4.3(c-d), cover distances from $\rho_{\min} \approx 3\mu\text{m}$ to $\rho_{\max} \approx 9\mu\text{m}$, at frequencies $\sim 0.5-1\,\text{Hz}$. In turn, shorter oscillations, taking place along the direction perpendicular to the laser polarization, go from $\rho_{\min} \approx 3.5\mu\text{m}$ to $\rho_{\max} \approx 5.5\mu\text{m}$, with frequency $\sim 1-2\,\text{Hz}$. Evaluating the integrals is lengthy but after some algebra we obtain:

$$\begin{aligned} &\mathcal{W} \sim 10^{-18} \text{ up to } 10^{-17}\text{J} \\ \Longrightarrow \quad &\eta_{\text{eff}} = \frac{\mathcal{W}}{U_{\text{in}}} \sim 10^{-15} \text{ up to } 10^{-14}\,, \end{aligned}$$

where the incident light energy onto the microsphere during a cycle reads

$$U_{\text{in}} = \int_{\text{cycle}} I_o(z)\pi a^2 exp(-2\rho^2/w^2)\, dt \sim 2.5 \times 10^{-3}\text{J} \tag{4.9}$$

(at $z \approx -5\mu$m one has $w = w(z) \sim 5.2\mu$m and $I_0(z) \approx 5 \times 10^8 \mathrm{W/m^2}$). Specifically, the work done during the cycle presented in Fig. 4.4(b) gives 4.3×10^{-18}J. The performance of our Ge-microsphere engine is comparable to that recently realized for a light absorbing microparticle whose dynamics comes about by demixing processes [74]. In this case the estimated (maximum) work/cycle gives $373 k_B T$ ($\sim 1.5 \times 10^{-18}$J at room temperature) and efficiency of 1.16×10^{-14}. Such values are also comparable to those obtained for light absorbing microparticles propelled by explosive bubbles due to excess heating [223]. For instance, a 1μm-size bead was reported to perform work/cycle $\sim 10^{-17}$ J. Above performances are higher than those reported for colloidal heat Brownian-Carnot engine ($\mathcal{W}_{\max} = 5 k_B T \approx 2.1 \times 10^{-20}$ J, at room temperature range) [222] and micrometer-scaled heat engine ($\mathcal{W}_{\max} = 0.3 k_B T \approx 1.2 \times 10^{-21}$ J), see Ref. [224].

It is worth emphasizing that our proposal for a microscopic engine does not depend on mixing different specific liquids nor on boiling bubbles that interact with the beads (as it is the case for Refs. [74] and [223], respectively). The engine operates in the simplest possible medium and works at temperatures below the water boiling temperature. Furthermore, to our best knowledge, our work is the first with direct experimental verification of the results pointed out in Ref. [6], regarding the asymmetry in the optical force generated by linear polarization. Our approach suggests a new application for semiconductors, opening an avenue of possibilities for the application of such materials in optical tweezers and single molecule experiments.

4.4 Conclusions

In summary, Ge microparticles suspended in water are observed to oscillate whenever subject to a highly focused laser beam, with remarkable similarity to what occur to Bi_2Te_3 and Bi_2Se_3 topological insulator beads [1]. Once such a kind of compounds share some electrical and optical properties with semiconductors, we may wonder whether optically induced oscillatory motion is the typical dynamics of semiconductor beads under the action of focused laser light. More specifically, Ge-particles tend to oscillate in a direction perpendicular to the linear polarization of the laser beam. A possible explanation for such a dependence on the laser polarization is based on the theory of charge carriers in crystal lattice materials: Ge has a considerable density of free carriers inside its bulk,

rendering a strong response to the light polarization. In contrast, topological insulator compounds have most of their free electrons lying on the surface, due to the energy band gap in the bulk of the material. This would justify why the topological insulator beads are practically insensitive to light polarization, as reported in Ref. [1]. Our present findings suggest that semiconductor-type beads tend to oscillate under the action of highly focused laser beams, as those used in OT setups. In fact, it has recently been verified the signature of this behavior for silicon (Si) microparticles [77], which indicates that such a novel phenomenon may be typical of conventional semiconductor materials. In Ref. [77] the authors propose that, in some semiconductor materials, the decreasing of the refractive index due to plasmonic resonances [218, 225] can cause an inversion of the gradient force sign as the particle approach the optical axis. As a result, the gradient force can also contribute to the repulsive force responsible for the removal regime of the oscillations.

In face of these results, we believe that semiconductor materials could find applications in dynamical measurements of mechanical properties of small systems, including macromolecules such as DNA, membranes and so forth.

PART II

Chapter 5

Geometrically induced reversion of Hall current in a topological insulator cavity

This Chapter is devoted to the results reported in Ref. [9] [Adapted from (W. H. Campos, W. A. Moura-Melo, J. M. Fonseca, "Geometrically induced reversion of Hall current in a topological insulator cavity," *Physics Letters A* **381**(5), 417-421 (2017). `https://doi.org/10.1016/j.physleta.2016.11.037`) Copyright © 2016 Elsevier B.V.][1]. It is known that an electric charge near the surface of a topological insulator induces an image magnetic monopole, as long as time reversal symmetry is broken and the topological magneto-electric effect is in order. Here, we show that if the topological insulator surface has a negative curvature, i.e., in the case of a semispherical cavity, the induced Hall current reverses its rotation as the electric charge crosses the semisphere geometric focus. Such a reversion is shown to be equivalent of inverting the charge of the image magnetic monopole. We also discuss the case of a semicylindrical cavity, where the Hall current reversion appears to be feasible of probing in realistic experiments.

Condensed matter states described by Landau's theory are characterized by order parameters which are well-behaved, except at phase transitions, where they are related to symmetry breaking in the material structure. Instead, topological insulators (TI's)

[1]This article was published under an Elsevier user license. According to information obtained from the RightsLink system (click here to be redirected to the corresponding page) and from Elsevier copyright webpage (`https://www.elsevier.com/about/policies/copyright`), permission is not required for authors to include their article's content in their thesis, provided it is not published commercially and appropriate reference is made.

[106, 107, 126] constitute a recently discovered state of matter that presents topological order. In such materials the bulk is gapped as in conventional insulators, but they support gapless metallic surface states as a manifestation of topological order. These metallic states are protected by time reversal symmetry (TRS) and their stability is robust against non-magnetic impurities or mechanical deformations on the surface. In addition, the motion of the carriers obeys spin-momentum locking, with their spins lying on the surface and pointing perpendicularly to momentum everywhere [226].

Such surface states may acquire a gap whenever TRS is broken, for instance, by means of a magnetic perturbation (applied field and/or film coating). As a consequence, a superficial Hall conductivity $\sigma_{xy} = (n + \frac{1}{2})\frac{e^2}{h}$ is predicted (we use CGS units; n is an integer, e is the electronic charge, h is the Planck constant). In addition, low energy topological insulating phase properties may be described in terms of the so-called topological magneto-electric effect (TMEE) [84,106,126], which is a (topological) ground-state response function [227]. Such an effect may be readily accounted for in the usual electrodynamics, keeping the Maxwell equations unaltered in form, but changing the constitutive relations according to [84, 123]:

$$\begin{aligned} \mathbf{D} &= \mathbf{E} + 4\pi\mathbf{P} - 2\alpha P_3\mathbf{B} \\ \mathbf{H} &= \mathbf{B} - 4\pi\mathbf{M} + 2\alpha P_3\mathbf{E}, \end{aligned} \tag{5.1}$$

where $\alpha = e^2/\hbar c \approx 1/137$ is the fine structure constant and P_3 is the electric-magnetic polarization [84,123]. In conventional insulators $P_3 = 0$, while $P_3 = \text{sign}[\mathbf{M}\cdot\hat{\mathbf{n}}]/2 = \pm 1/2$ for a TI. The direction of the surface magnetization, $\mathbf{M}$, determines the sign of P_3: + (-) if it points out of (into) the TI surface ($\hat{\mathbf{n}}$ is a unit vector normal to the surface). Physically, we clearly realize how TMEE dictates the unique TI electromagnetic behavior: an electric (and/or magnetic) field induces both an electric polarization and a magnetization, i.e., an electric field crossing the TI surface induces on its surface a Hall current given by [84,106]:

$$\mathbf{J}_{\text{Hall}} = P_3\frac{e^2}{h}\hat{\mathbf{n}} \times \mathbf{E}\,. \tag{5.2}$$

This current clearly depends on the surface geometry, and its associated magnetic field may have special features. For instance, in a conical TI this current yields a topological electric polarization that depends on the cone aperture angle. Under the same external

conditions, wider ($\delta > 30^o$) and narrower ($\delta < 30^o$) cones appear to polarize in opposite directions [137]. On the other hand, a point-like electric charge located near a TI flat surface induces a magnetic field resembling that produced by a magnetic monopole [123]. It should be stressed that such an image magnetic monopole is not an elementary neither an emergent excitation at all: it rather comes to be an artificial particle that describes the physical effects associated to the Hall sources on the surface of a TI, as described by TMEE. Therefore, the monopoles discussed here look like images of Dirac magnetic monopoles [228]. In addition, they should not be confused with the emergent monopoles observed in spin ice systems, even though in both cases the monopole appears attached to a physical string of dipoles. Actually, in spin ices, the original degrees of freedom (magnetic dipoles) are shown to *fractionalize* into isolated magnetic poles connected in pairs by physical strings [229–231]. Here, we consider the case of a concave TI surface, namely, a semispherical cavity. [The semicylindrical cavity is also discussed in some detail]. Besides realizing the induced image monopole, we also find that whenever the electric charge crosses the semispherical focus the magnetic charge of the monopole is reversed. Physically, such a picture corresponds to a reversion in the rotation of the induced Hall current whenever the electric charge exactly crosses the focus.

5.1 The semispherical geometry and the monopole reversion

Let the left half-space, ($z < 0$), be a TI with an electric permittivity and magnetic permeability (ϵ_2, μ_2) whereas the right side, ($z > 0$), is occupied by an ordinary insulator with (ϵ_1, μ_1). A semispherical cavity, radius $\mathbf{R}$ centered at $z = 0$, is made in the TI, according to Fig. 5.1. Let also the electric charge, q, be placed along z-axis, say, at z_0. Whenever one breaks TRS on the cavity surface, for instance, by coating it with a thin ferromagnetic film, a Hall current is induced by the electric field produced by q, according to Eq. (5.2), as depicted in Fig. 5.1. Note that the magnetic field produced by such a current is equivalent to that generated by an image magnetic monopole, g_1, along with an image magnetic string extending from it to $z \to -\infty$. However, as a whole the Hall current produces both, electric and magnetic fields, in such a way that the induced image carries both electric and magnetic charges, (q_1, g_1): it resembles a *dyon*. In addition,

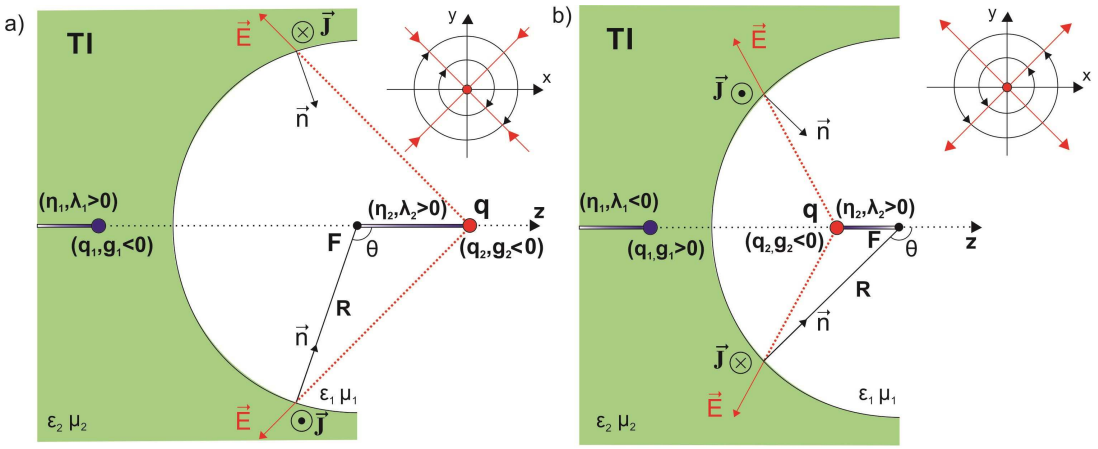

Figure 5.1: Schematic illustration of the semisphere cavity and its coordinate system. The z-axis origin is set at the focus **F**, z_0 accounts for the position of the electric charge, q, while (ϵ_1, μ_1) and (ϵ_2, μ_2) are the electric permittivity and magnetic permeability of conventional and TI, respectively. The magnetic monopole charge is reversed whenever the electric charge crosses the semisphere focus. In figure a), $z_0 > 0$, the Hall current, Eq. (2), rotates clockwise (see inset), being equivalent to a negative image monopole, $g_1 < 0$. In figure b), whenever $z_0 < 0$ the Hall current rotates counterclockwise, whose magnetic field resembles that produced by a monopole with charge $g_1 > 0$ (see inset). Electric charge q was assumed to be positive, otherwise the Hall current and therefore all image charges experience a change of sign. The red lines represent the electric field and the black circles represent the circulating surface current, $\mathbf{J}_{\text{Hall}}$. The magnetic field lines have been omitted for simplicity. Actually, the image object is a dyon, carrying both electric and magnetic charges (q_1 and g_1); attached to it there is a string of electric and magnetic charges, $\eta_1(z)$ and $\lambda_1(z)$ (see text for details). There is also a dyon (q_2,g_2) at z_0, attached to a string ($\eta_2(z)$,$\lambda_2(z)$); these (image) objects describes the magnetic field inside the TI. The latter dyon does not reverses its sign. θ is the usual spherical polar angle; due to the azimuthal symmetry of the cavity, its related angle, ϕ, is not shown. Adapted from Ref. [9].

there are also image strings carrying electric and magnetic charges extending from the dyon to $z \to -\infty$, accounted respectively by $\eta_1(z)$ and $\lambda_1(z)$ in Fig.5.1. The physical reason why such strings must be in order comes from the fact that $\nabla \cdot \mathbf{B} = 0$, so that the total magnetic charge of the image string must exactly cancel the monopole charge: $\int \lambda_1(z)dz = -g_1$. In order to describe the magnetic field inside TI, there is also an image *dyon* (q_2, g_2) located at z_0 and attached to a string ($\eta_2(z)$, $\lambda_2(z)$) extending from it to the semisphere focus **F**. This picture is analogous to that realized in planar and spherical topological insulators, as reported in Ref. [123].

The main finding here concerns the reversion of the magnetic charge sign according to the location of the electric charge: if q is placed at $z > 0$ (on the right of the focus, **F**) $\mathbf{J}_{\text{Hall}}$ rotates clockwise, which corresponds to a negative magnetic monopole, $g_1 < 0$, panel

a) in Fig.5.1; whereas for $z_0 < 0$ the current flows counter-clockwise, whose magnetic field resembles that produced by a positive monopole, $g_1 > 0$, as depicted in panel b) Fig.5.1. The electric charge of the dyon, q_1, does not experience any inversion in its sign as charge q crosses the focus, neither do the image charges inside the cavity.

In order to show the results above in further details, let us consider the simple situation where both dielectrics have the same (ϵ, μ), say, $\mu_1 = \mu_2 = \epsilon_1 = \epsilon_2 = 1$. In addition, consider only the first order contribution to the electric field, say, that due to the charge q: $\mathbf{E} = q\frac{\vec{r}-z_0\hat{z}}{|\vec{r}-z_0\hat{z}|^3}$. Thus, Hall current is obtained, up to order $\alpha = e^2/\hbar c$ (linear response regime), to read:

$$\mathbf{J}_{\text{Hall}} = -\frac{\alpha c}{4\pi}\frac{qz_0\sin\theta}{(R^2 + {z_0}^2 - 2Rz_0\cos\theta)^{3/2}}\hat{\phi}\,, \tag{5.3}$$

where we have used $P_3 = +1/2$. Higher order contribution, $\mathcal{O}(\alpha^2)$, only correct the current by very small values and have been neglected.

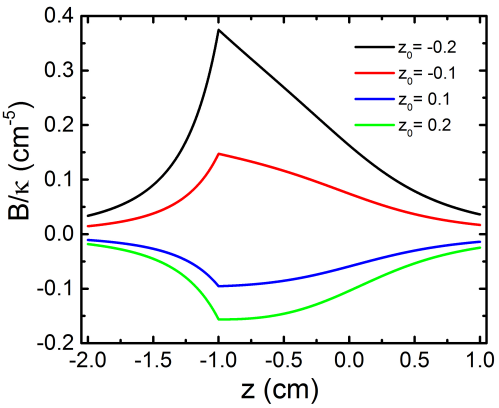

Figure 5.2: Behavior of the magnetic field along z-axis, for q fixed at different positions, z_0. Namely, note the change in the field sign whenever the electric charge crosses the cavity focus, $z = 0$ (we have set $R = 1$cm, and $\kappa = 2\pi\frac{e^2}{2h}\frac{q}{c}R^3$). Adapted from Ref. [9].

From the expression above, one clearly realize the magnetic charge reversion whenever the charge q crosses the cavity focus, $z_0 = 0$. Taking this current to the Biot-Savart equation, we obtain its generated magnetic field, $\mathbf{B}$, Eq. (5.7). Such a calculus is tedious and length; it is presented in the Appendix. How $\mathbf{B}$ behaves along z-axis is shown in Fig. (5.2) for several values of z_0. Notice the change in the magnetic field when the electric charge is on the right or left of the focus, evidencing the reversion of the magnetic charge. For the sake of completeness, let us also briefly discuss the case of a a semicylindrical cav-

ity. Instead of a unique point charge, let also a wire carrying charge density λ extending above the cavity along y-axis, as depicted in Fig.5.3. The wire height z_0 may be varied

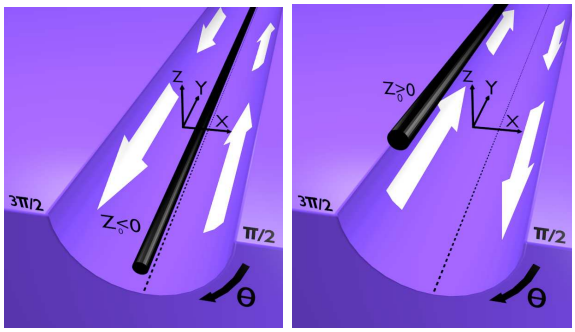

Figure 5.3: The semicylindrical cavity, along with a straight wire of charge density (black bars along y-axis). In this case, the induced Hall current splits into two branches flowing in opposite directions, as indicated by white arrows. As the wire height crosses the cavity focus, $z_0 = 0$, both branches reverse their flows. Adapted from Ref. [9].

and as it crosses $z_0 = 0$ each branch of the induced Hall current reverses its direction along the wire axis. Electric contacts at the cavity borders may directly measure the current properties and its reversion, as well. Therefore, while the straight wire splits the

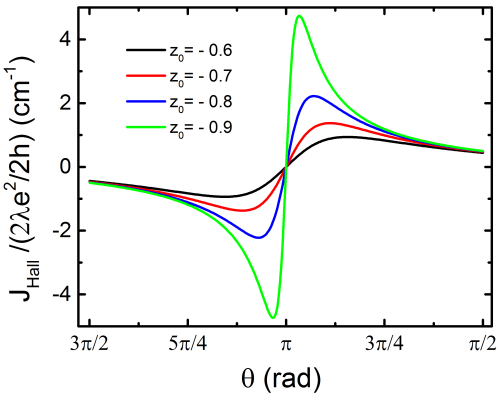

Figure 5.4: How the Hall current behave. Left branch corresponds to $\pi < \theta \leq 3\pi/2$ while $\theta \in [\pi/2, \pi)$ accounts for the right branch (Fig. 5.3). We have taken a unity radius for the cavity, $R = 1$, and put the wire in a number of heights inside the cavity ($z_0 < 0$). Adapted from Ref. [9].

current into two longitudinal branches, the negative curvature of the cavity encompass its flow reversion, like occurs in the semisphere. Actually, the induced Hall current is readily obtained to be (up to α^1):

$$\mathbf{J}_{\text{Hall}} = -\frac{\alpha c}{4\pi} \frac{(2\lambda) z_0 \sin\theta}{R^2 + z_0^2 - 2R z_0 \cos\theta} \, \hat{y} \, . \tag{5.4}$$

The above-mentioned current reversion may be easily realized from the expression above by setting $z_0 \to -z_0$. The current behavior is plotted against θ in Fig. 5.4. From a magnetic monopole point of view, this can be understood as a reversion of the monopole charge, analogously to what occurs in the semispherical case. Such a similarity may be clearly realized if we consider the 2D slice of both cases, giving us a semicircle problem.

5.2 Magnetic monopole picture

We shall discuss on the magnetic monopole description of the problem taking into account the semispherical cavity results. A similar picture may be done for semicylindrical cavity in an analogous way.

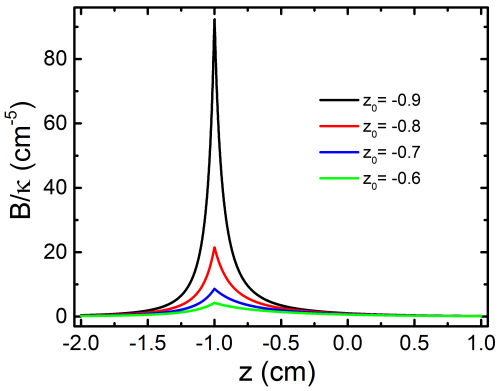

Figure 5.5: Whenever the electric charge is placed very close to the interface, the experienced magnetic field is essentially that produced by an image point-like magnetic charge. Note the large increasing in the magnitude of **B** as one places the charge near to the interface, $z_0 \sim -1$. Adapted from Ref. [9].

The peaks at the interface, $z = -1$, presented in Fig. 5.2 are clear evidences of the monopole, and may be better understood whenever q is taken close to $z = -1$, as shown in Fig. 5.5. Therefore, near the interface one experiences a magnetic field largely dominated by the monopole, so that as $z \to -1$ one practically realize only the point-like monopole itself. This is an expected result, since whenever one approaches the interface one should recover the result of a plane TI discussed in [123], say: charge q induces an image point-like magnetic monopole. Essentially, the contribution due the image magnetic string is very small. Geometrically speaking, whenever q is close to the interface, their relative separation is much smaller than the cavity curvature radius, say $(R - |z_0|) << R$, then the surface seems to be flat.

In Fig. (5.6) we have plotted the magnetic field generated by the Hall current, Eq. (5.7), with that produced by a unique point-like magnetic monopole, $B_m = \mu_1 g_1/(z-z_m)^2$. To improve the comparison, the monopole is slightly shifted around its exact position, $z_m = \frac{R^2}{z_0}$, by $\delta z_m = \pm 0.02R$. At each of these shifted positions, the field due to the monopole alone approaches the real field, Eq. (5.7). Actually, if the monopole is taken to z_m its field fits that due to the induced Hall current with high precision. Such results further support the picture of the physical situation as that provided by a point-like magnetic monopole, namely, when we are close to the interface. But, how close does this picture remains valid? As wee shall see below, it is in good accordance even if the charge is taken to about $z_0 \sim -0.8R$, provided that the probe is kept near to the interface, $z \approx -R$.

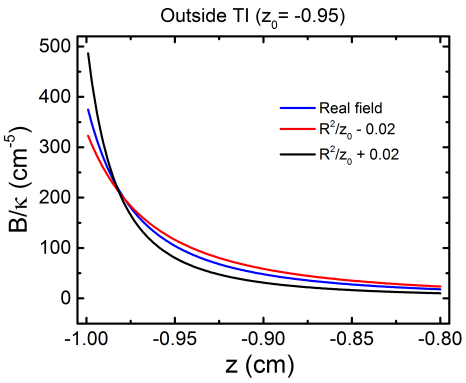

Figure 5.6: Magnetic fields generated by the Hall current (blue curve), Eq. (5.7), and by the image point-like magnetic monopole, $B_m = \mu_1 g_1/(z - z_m)^2$, slightly shifted from its exact position, z_m, by $\delta z_m = \pm 0.02R$. We have taken $R = 1\,\text{cm}$ and placed q close to the interface, at $z_0 = -0.95R$. As the magnetic monopole is placed at z_m its field fits almost exactly the real curve. Adapted from Ref. [9].

In Ref. [123] the authors have found that the strength of the image magnetic monopole decreases with the inverse of the distance between the electric charge and the center of the spherical surface. Here, by virtue of the negative curvature of the semispherical cavity, the magnitude linearly increases, as shown in Fig. (5.7). Such a behavior occurs whenever q is sufficiently close to the interface, say, the regime in which the point-like magnetic picture of the real problem is applicable. According to Fig. (5.7), such a picture remains to be valid at least up to $z_0 \sim -0.8R$. In particular, such an interval comprises the results presented in Fig. 5.6.

However, if we get apart from the interface, say, observing the system from a far away point, $z >> R$, then magnetic field goes as $1/z^3$. This is not surprising, once as

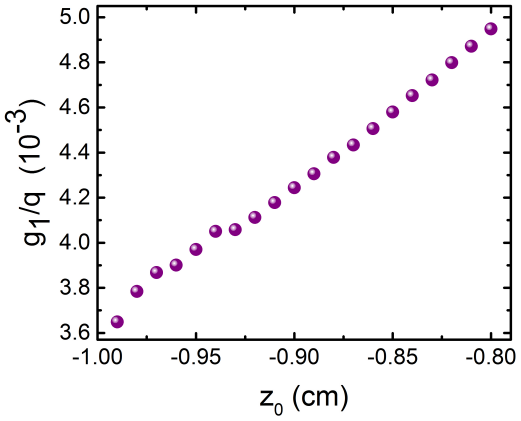

Figure 5.7: Behavior of the image magnetic monopole strength as the electric charge is taken apart from the interface. Since monopole strength, g_1, linearly increases up to $z_0 \approx -0.8R$, the magnetic monopole picture is valid at least to such a separation, provided we also remain close to the interface (further details below). Adapted from Ref. [9].

seen far away, the set magnetic string plus monopole looks like a magnetic dipole around z_m. At some extent, this is what happens with the tip of a magnetic needle, as reported in Ref. [232].

On the other hand, Hall current field spreads throughout the bulk of the topological insulator, as well. Therefore, from the point of view of an observer located inside the bulk, the magnetic field seems to be that produced by an image magnetic monopole, g_2, located at z_0, along with a string, λ_2. Then, as a whole, such an observer realize that all the electromagnetic field resembles that generated by a dyon placed at z_0 along with a string carrying both electric and magnetic charges, but extending from the monopole to the focus.

Following the discussion made by König *et al* [233], we emphasize that in realistic 3D TI's experiments the thickness of the sample takes only a few hundred atomic layers (around a few dozens of nanometers), constituting therefore a thin film. In such a case, an external field applied to a border side may cross the bulk reaching the opposite surface of the film. This is important because each surface contributes with a single Dirac cone yielding a net Hall conductivity of $\sigma_i = (-1)^{i+1}(n_i + \frac{1}{2})\frac{e^2}{h}$, with $i = 1, 2$ accounting for upper and bottom surface, respectively. Taking the linear response approach, the total magnetic field is simply the superposition of those generated by each Hall current.

5.3 Conclusions and Prospects

In summary, we have seen that an electric charge placed near to a semispherical topological insulator cavity induces a superficial Hall current which reverses its rotation whenever the charge crosses the semisphere focus. Such a current is known to generate a magnetic field analogous that produced by an image magnetic monopole. Thus, current reversion is shown to be equivalent to invert the sign of the magnetic monopole.

Experimentally, to probe both the induced Hall current along with its reversion (monopole reversion) a gap must be open in the surface states of the TI in a such a way that the Fermi level is kept within the gap. An efficient way to achieve this is by doping the as-grown TI with Mn and Fe dopants [134]. Later, let the TI cavity be coated with a soft ferromagnetic insulator, say, whose magnetization points normal to its surface. [Alternatively, Cr-doped $Bi_2(Se_xTe_{1-x})_3$ ferromagnetic TI's could be used. In this case, the magnetic order to break TRS is intrinsically provided by the compound itself, without necessity of further coating. See Ref. [234] for details]. Now, whenever placing the electric charge near the cavity, its induced magnetic field does modify the film magnetization whose profile is dependent on the monopole parameters, like strength and sign. Therefore, magnetic force microscopy (MFM) may be used to probe such a magnetization pattern. For the sake of completeness, if we consider a cavity of radius $R = 1\,\mathrm{cm}$, then an electric charge around $q = 10^{15}e$ induces a magnetic field about $100\,\mathrm{Gauss}$, which is enough to modify the magnetization of the film in a detectable way.

Along these lines, the use of the semicylindrical cavity, as illustrated in Fig. 5.3, may be much more feasible for experiments. In this case, it is relatively easy to move the wire to vary its height to the cavity, leading to Hall current reversion. Such a current, along with its reversion may be directly measured by gate potential connected to the cavity borders. Even more important, such a set up may be useful to detect the half-integer Hall conductivity in direct transport experiments, as pointed out in the work of Ref. [233]. Usually, the electric contacts attached to the surface are not able to capture only the local properties of the Hall current, due its curl character around the diode generating the bias potential. Here, the current flows straight along the wire axis diminishing considerably curl effects.

Appendix: Magnetic Field for semispheric geometry

To obtain the magnetic field along z axis, one uses the current given by Eq. (5.3) in the Biot-Savart law [58]:

$$\mathbf{B}(z\hat{\mathbf{z}}) = \frac{1}{c}\int_{\mathcal{S}} \frac{\mathbf{J}_{\text{Hall}}(\mathbf{r}') \times (z\hat{\mathbf{z}} - \mathbf{r}')}{|z\hat{\mathbf{z}} - \mathbf{r}'|^3} da', \tag{5.5}$$

where $\mathcal{S}$ represents the semispherical interface, da' is the infinitesimal area element and c is the speed of light. After some algebra, we obtain:

$$\begin{aligned} \mathbf{B}(z\hat{\mathbf{z}}) = & - 2\pi \frac{e^2}{2h}\frac{qz_0}{c} R^3 \Bigg\{ \int_{\frac{\pi}{2}}^{\pi} \frac{\sin\theta'}{(a + b\cos\theta' + d\cos^2\theta')^{\frac{3}{2}}} d\theta' \\ & - \int_{\frac{\pi}{2}}^{\pi} \frac{\sin\theta'\cos^2\theta'}{(a + b\cos\theta' + d\cos^2\theta')^{\frac{3}{2}}} d\theta' \Bigg\} \hat{\mathbf{z}}\,, \end{aligned} \tag{5.6}$$

where $a = (R^2 + z_0^2)(R^2 + z^2)$, $\quad b = -2R(zR^2 + zz_0^2 + z_0R^2 + z_0z^2)$, $\quad$ and $d = 4R^2zz_0$.

The first integral may be readily solved, while the second one needs the result from Eq. (2.264-7), Ref. [235]. The final expression takes the form below, which has been used in Sections 5.1 and 5.2, mainly for numeric evaluation of a number of plots. It should be stressed that such an expression is exact up to 1st order in α (linear response regime).

$$\frac{\mathbf{B}(z\hat{\mathbf{z}})}{2\pi\frac{e^2}{2h}\frac{q}{c}R^3} = -z_0\hat{\mathbf{z}}\begin{cases} \dfrac{4d-2b}{(4ad-b^2)\sqrt{a-b+d}}+\dfrac{2b}{(4ad-b^2)\sqrt{a}}+ \\ \quad+\dfrac{1}{d(4ad-b^2)}\left[\dfrac{4ad-2b^2+2ab}{\sqrt{a-b+d}}-\dfrac{2ab}{\sqrt{a}}\right]+ \\ \quad+\dfrac{1}{d\sqrt{d}}\ln\dfrac{2\sqrt{d(a-b+d)}-2d+b}{2\sqrt{ad}+b}, \\ \qquad\qquad \text{if } d>0. \\ \dfrac{4d-2b}{(4ad-b^2)\sqrt{a-b+d}}+\dfrac{2b}{(4ad-b^2)\sqrt{a}}+ \\ \quad+\dfrac{1}{d(4ad-b^2)}\left[\dfrac{4ad-2b^2+2ab}{\sqrt{a-b+d}}-\dfrac{2ab}{\sqrt{a}}\right]+ \\ \quad+\dfrac{1}{d\sqrt{-d}}\left[\arcsin\dfrac{b}{\sqrt{b^2-4ad}}-\arcsin\dfrac{b-2d}{\sqrt{b^2-4ad}}\right], \\ \qquad\qquad \text{if } d<0. \end{cases} \tag{5.7}$$

Chapter 6

Higher order topology analysis of electronic band structures in (anti) ferromagnetic systems

In this chapter we discuss our investigations in collaboration with Dr. Libor Šmejkal and Prof. Jairo Sinova during my Ph.D. "Sandwich" scholarship with their group in Germany, at the Johannes Gutenberg Universität Mainz (JGU). It should be stressed that the results reported here are very preliminary, so that their refinement and interpretation are still in progress. We have studied a modified version of the spinless model proposed by Benalcazar et. al. in Ref. [159] for the quantized electric quadrupole moment in a higher order topological insulator (HOTI) phase (see Subsection 1.2.4). Here, we consider spinful electrons hopping between atoms with either ferromagnetic (FM) or antiferromagnetic (AF) ordering. We have also analyzed the minimal model inspired by the tetragonal AF CuMnAs, proposed by Šmejkal et. al. in Ref. [196], as well as its FM variation. The lattice tight-binding approach is applied to all systems above to investigate the existence of metallic edge-states, corner states, and their topology. With the experience obtained by analyzing these models, we intend to expand our investigations to more complex and realistic materials.

6.1 Objectives

Our main goal is to propose a theoretical model for an AF crystal presenting also HOTI phase. We expect to predict topologically quantized corner states which are time reversal symmetry (TRS) broken counterparts of the spinless corner states present in the electric quadrupole phase [159] (see Subsection 1.2.4), corresponding to a magnetic quadrupole phase. We believe that adjacent corners would exhibit localized states of opposite spin-polarizations in such system, which could find interesting applications in spintronics. Our strategy is to first reproduce the main results of Ref. [159] for the energy spectrum of quantized electric multipole insulators in two and three dimensions. Subsequently, we define the systems of interest by adding a Zeeman-like term that couples the spin degrees of freedom to either a uniform or staggered exchange field. By calculating the energy spectrum for the bulk, edges and corners, we aim to investigate the presence of localized states in such systems. We also calculate the Wannier charge centers (WCC's) for the systems above to investigate their topology. Following the same line of reasoning, we reproduce the main results for the minimal model inspired by the tetragonal AF CuMnAs reported in Ref. [196], define an analogous model with FM order and investigate the presence of localized states and topology for both systems. The analysis of the systems above gives us experience with the numerical simulation of electronic band structures of magnetic materials and topological materials protected by crystal symmetries. By performing these tasks, we have learned programming in Python using the "PythTB" package for numerical simulations in condensed matter quantum systems. Furthermore, we have also implemented parallel computing in "High Performance Computing" (HPC) with "Message Passing Interface" (MPI). After the successful accomplishment of the objectives above, we aim to identify real materials in which the desired effects could manifest.

6.2 Methods

All numerical simulations in this Chapter were performed in Python, using the PythTB package developed by S. Coh, D. Vanderbilt and collaborators [236]. The package is able cut the system in either ribbon or rectangular geometries, diagonalize the Hamiltonian and return the eingenvalues and eingenvectors for each crystal momentum $\vec{k}$. It can also calculate Berry phases and WCC's, being very useful for our purposes.

Detailed definitions and discussions about WCC's can be found in Ref. [237] and in the Supplementary Material of Ref. [159]. Here, we restrict ourselves to provide a brief physical interpretation and to discuss how they can be used to infer the topology of a system.

Consider the projection operator onto the set of occupied energy bands, defined as

$$P(k_x) \equiv \sum_{n}^{occ} \sum_{k_y} |\psi_{n\vec{k}}\rangle\langle\psi_{n\vec{k}}|, \tag{6.1}$$

where $|\psi_{n\vec{k}}\rangle = e^{i\vec{k}\cdot\vec{r}}|u_{n\vec{k}}\rangle$ are the extended Bloch functions, $|u_{n\vec{k}}\rangle$ are the cell-periodic Bloch states, $\vec{k} = (k_x, k_y)$ and n are the crystal momentum and the band index, respectively. Notice that the summation in n runs only over the occupied energy bands (indicated by "occ"), while the summation in k_y runs over the Brillouin Zone (BZ).

The eigenstates of the band-projected position operator $P(k_x)\hat{y}P(k_x)$ are known as maximally localized Wannier functions (WF's) and can be written as unitary transformations of the cell-periodic Bloch states:

$$|W_{n,l_y}(k_x)\rangle = \frac{1}{2\pi}\int_{BZ} dk_y e^{i\vec{k}\cdot(\vec{r}-l_y\hat{y})}|u_{n\vec{k}}\rangle, \tag{6.2}$$

where l_y is a layer index. Due to the $U(N)$ gauge freedom (N is the number of occupied states for each $\vec{k}$-point) in the choice of $|u_{n\vec{k}}\rangle$, the WF's are gauge-dependent. This allows for a convenient gauge choice that minimizes the spread of the WF's, so that they become maximally localized [237].

The WCC's of the WF's along y direction, which are also eigenvalues of the band-projected position operator $P(k_x)\hat{y}P(k_x)$, are defined as the expectation values of the position operator $\hat{y}$ for the WF's with $l_y = 0$, that is

$$\overline{y}_n(k_x) = \langle W_{n,0}(k_x)|\hat{y}|W_{n,0}(k_x)\rangle. \tag{6.3}$$

Therefore, the WCC's correspond to the average positions of the electrons relative to the origin of the unit cell.

As discussed in Ref. [237], the WCC's share the same kind of topological information as the boundary energy bands. If the Fermi level is located inside the bulk gap, crossing the energy eigenvalues of the boundary states an even number of times, then the system is in a trivial phase and the WCC's also present a trivial behavior. In turn, if the

system is topological and the Fermi level crosses the boundary states an odd number of times, the WCC's present a zig-zag structure, changing partners at high-symmetry points just as the energy bands of topological boundary states. This allows for the topological classification of materials by analyzing the WCC's.

In the present study, we are also interested in the $\vec{k}$-dependent spin-polarization of the energy bands, defined as [238]

$$P_i^{n\vec{k}} \equiv \left\langle \psi_{n\vec{k}} \right| \frac{\sigma_i}{2} \left| \psi_{n\vec{k}} \right\rangle, \tag{6.4}$$

where σ_i $(i = x, y, z)$ are the Pauli matrices representing spin degrees of freedom. It is implemented in our code as follows.

Let $|\phi_{\vec{R}js}\rangle$ be the tight-binding basis for the orbital of type j, spin $s = \pm 1/2$ (along z), in cell $\vec{R}$. In the PythTB package, the Bloch-like basis reads

$$\left| \chi_{js}^{\vec{k}} \right\rangle = \sum_{\vec{R}} e^{i\vec{k}\cdot\left(\vec{R}+\vec{t}_j\right)} \left| \phi_{\vec{R}js} \right\rangle, \tag{6.5}$$

where $\vec{t}_j$ is the location of the atom hosting orbital j relative to the center of the unit cell. The Bloch eigenstates can be expanded as

$$\left| \psi_{n\vec{k}} \right\rangle = \sum_{js} C_{js}^{n\vec{k}} \left| \chi_{js}^{\vec{k}} \right\rangle. \tag{6.6}$$

Finally, the $\vec{k}$-dependent spin-polarization (along i) of state $\left|\psi_{n\vec{k}}\right\rangle$ can be calculated by substituting Eq. (6.6) in Eq. (6.4). When calculating the spin-polarization along z, it can be easily shown to be

$$P_z^{n\vec{k}} = \sum_{js} \left| C_{js}^{n\vec{k}} \right|^2 s = \frac{1}{2} \sum_j \left(|C_{j\uparrow}^{n\vec{k}}|^2 - |C_{j\downarrow}^{n\vec{k}}|^2 \right), \tag{6.7}$$

where $\uparrow = +1/2$ and $\downarrow = -1/2$.

6.3 Spinful quantized electric quadrupole moment in the (anti)ferromagnetic 2D SSH model

Topological states have been one of the most active topics of condensed matter physics in the last two decades. Special attention has been given to TCI's and HOTI's [153, 239]. In both cases, protection of the topological boundary states involves at least one crystal point group symmetry, and may or may not involve TRS. In addition, many of these materials do not require SOC, being fundamentally distinct from their TI's cousins. In Ref. [159], Benalcazar et. al. have proposed two and three-dimensional analogues

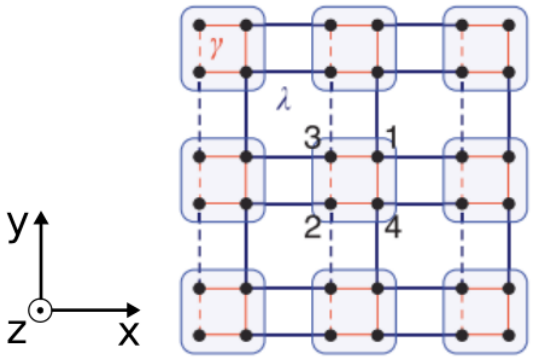

Figure 6.1: Tight binding model for the spinless electric quadrupole insulator in 2D, along with definition of the coordinate system. Solid (dashed) lines represent positive (negative) hopping terms, in which lines representing the hopping of strength γ between orbitals within the same unit cell are colored red and those representing the hopping of strength λ between orbitals in adjacent unit cells are colored blue. Adapted from Ref. [159].

of the spinless Su-Schrieffer-Heeger (SSH) model [240], which they have shown to host HOTI phases. These systems are said to host quantized electric multipole insulators, for they represent a generalization of the dipole polarization to higher electric multipole moments, with fractional electric charge of $\pm e/2$ at the boundaries of the boundaries. In Subsection 1.2.4, we have presented the 4-band Bloch Hamiltonian [Eq. (1.53)] for their toy-model describing an electric quadrupole insulator in 2D. Here, to perform the numerical simulations, we write this model in tight-binding as (see Fig. 6.1)

$$\begin{aligned} H = \; & \textstyle\sum_{\vec{R}} \sum_{i<j} t_{ij} a^{\dagger}_{\vec{R},i} a_{\vec{R},j} + \\ & + \lambda \textstyle\sum_{\vec{R}} \left[\left(a^{\dagger}_{\vec{R}+\hat{x},3} a_{\vec{R},1} + a^{\dagger}_{\vec{R}+\hat{x},2} a_{\vec{R},4} \right) + \left(a^{\dagger}_{\vec{R}+\hat{y},4} a_{\vec{R},1} - a^{\dagger}_{\vec{R}+\hat{y},2} a_{\vec{R},3} \right) \right], \end{aligned} \tag{6.8}$$

where

$$\begin{cases} t_{12} &= t_{34} = 0 \\ t_{13} &= t_{14} = -t_{23} = t_{24} = \gamma, \end{cases} \tag{6.9}$$

$\vec{R}$ labels the unit cell and $\{i, j\} = 1, 2, 3, 4$ label the four orbitals within each unit cell. The first term in Eq. (6.8) accounts for hopping of strength γ between orbitals within the same unit cell, while the second term accounts for hopping of strength λ between orbitals in neighboring cells. $\vec{R} + \hat{x}$ is the cell immediately to the right of $\vec{R}$ and $\vec{R} + \hat{y}$ is the cell immediately above (we consider the lattice constant to be normalized).

This model has a very simple form, so that it is invariant under many symmetries, including time-reversal, charge-conjugation and fourfold rotations. However, the ones important for the topological protection of the corner states are mirror symmetry about x [$M_x : (x, y) \to (-x, y)$] and y [$M_y : (x, y) \to (x, -y)$], and inversion symmetry [$\mathcal{I} : (x, y) \to (-x, -y)$]. According to Refs. [159, 241], $\mathcal{I}$ ensures the quantization of the electrical polarization, while the M_x and M_y symmetries are responsible for quantizing the electric quadrupole moment [159].

Here, we modify the spinless model above by adding new degrees of freedom to be acted upon by Pauli matrices $\vec{\sigma} = (\sigma_x, \sigma_y, \sigma_z)$. In principle, the physical meaning of these degrees of freedom depends on microscopic details of the atomic orbitals. For our preliminary analysis of this toy-model, we consider them to be spin degrees of freedom coupled to an external exchange field through a Zeeman-like term $H_Z = -\sum_{\vec{R}} \sum_{i,s} a^{\dagger}_{\vec{R},i,s} \vec{B}_i \cdot \vec{\sigma} a_{\vec{R},i,s}$. The $\vec{B}_i$ field can represent either a uniform ($\vec{B}_{uniform}$) or a staggered ($\vec{B}^i_{stagg}$) exchange field, i.e. the equivalent of FM or AF configurations of atoms at the underlying lattice, respectively. Even if such construction turns out not to be feasible in solid state systems, it could be engineered by using ultracold atoms in optical lattices [159, 242–244].

Although the model Hamiltonian in Eq. (6.8) is two-dimensional, we allow the exchange field to be perpendicular to the crystal plane, along the z direction. Notice that we are fundamentally changing important attributes of the system. First, the number of degrees of freedom is doubled with spin, so that the new model leads to eight energy bands, instead of four. Second, the exchange field $\vec{B}_i$ can break one or more of the three important symmetries. In fact, a uniform exchange field perpendicular to the crystal plane preserves $\mathcal{I}$ but breaks both M_x and M_y. A staggered exchange field, on the other hand, preserves both inversion and mirror symmetries. Therefore, it is expected that the

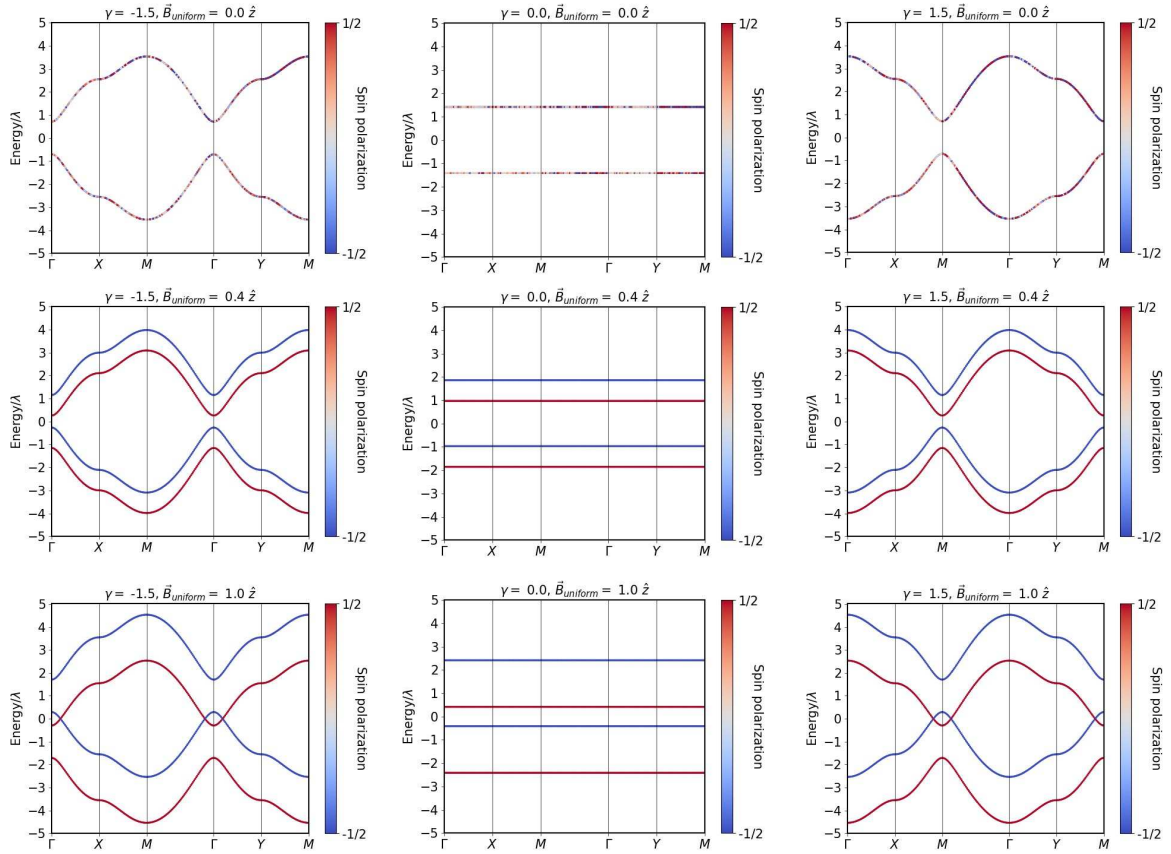

Figure 6.2: Bulk band structure of the FM model ($\vec{B}_i = \vec{B}_{uniform}$, along $\hat{z}$) on a 8×8 lattice with PBC. Each column from left to right shows our results for $\gamma = -1.5, 0.0$ and 1.5, respectively. In the original model, the system is in the trivial phase for $|\gamma| = 1.5$ and in the topological electrical quadrupole phase for $\gamma = 0$. Each line (of graphs) from top to bottom shows our results for $B_{uniform} = 0.0, 0.4$ and 1.0, respectively, in which the color scale indicates the spin-polarization defined by Eq. (6.4). For $|\gamma| = 1.5$, the bulk undergoes a metal-insulator transition with the variation of the exchange field, while for $\gamma = 0$ it remains insulating with such variation.

system present topological order in the latter situation. The fact that electrons are now spinful might change the symmetry criteria for the existence of a topological phase, a detail that still has to be investigated.

With all that in mind, we write the modified version of the model as

$$\begin{aligned} H = & \sum_{\vec{R}} \sum_{i<j,s} t_{ij} a^{\dagger}_{\vec{R},i,s} a_{\vec{R},j,s} \\ & + \lambda \sum_{\vec{R}} \sum_{s} \left[\left(a^{\dagger}_{\vec{R}+\hat{x},3,s} a_{\vec{R},1,s} + a^{\dagger}_{\vec{R}+\hat{x},2,s} a_{\vec{R},4,s} \right) + \left(a^{\dagger}_{\vec{R}+\hat{y},4,s} a_{\vec{R},1,s} - a^{\dagger}_{\vec{R}+\hat{y},2,s} a_{\vec{R},3,s} \right) \right] \\ & - \sum_{\vec{R}} \sum_{i,s} a^{\dagger}_{\vec{R},i,s} \vec{B}_i \cdot \vec{\sigma} a_{\vec{R},i,s}, \end{aligned} \tag{6.10}$$

where s labels the spin degrees of freedom, t_{ij} ($\propto \gamma$) is given in Eq. (6.9), and

$$\vec{B}_i = \begin{cases} \vec{B}_{uniform} & \text{uniform exchange field,} \\ \vec{B}^{i}_{stagg} & \text{staggered exchange field.} \end{cases} \tag{6.11}$$

At first, we consider periodic boundary conditions (PBC) in both x and y to obtain information about the bulk. Fig. 6.2 shows the bulk band structure for uniform exchange fields (FM model), $\vec{B}_{uniform} = B_{uniform}\hat{z}$, with $B_{uniform} = \{0.0, 0.4, 1.0\}$ and $\gamma = \{-1.5, 0.0, 1.5\}$. We have set $\lambda = 1$ in all our calculations. As discussed in Subsection 1.2.4, $\gamma = 0$ represents the topological phase limit for the original model, and $|\gamma| = 1.5$ represents its trivial insulator phase. The color scale indicates the spin-polarization [Eq. (6.4)] for each $\vec{k}$-point in the Brillouin zone (BZ). As expected, the exchange field splits the degeneracy of the energy bands, which now become spin-polarized. For $|\gamma| = 1.5$, notice that increasing $B_{uniform}$ leads to the closing of the energy gap, so that the bulk becomes metallic. For even higher values of $B_{uniform}$, the bands intercept each other but do not interact. For $\gamma = 0$, the energy bands are horizontal and the group velocities, $\vec{v}_g = (1/\hbar)\vec{\nabla}_k E_n$, are equal to zero for any value of the exchange field. Therefore, the bulk is always insulator in this case. Fig. 6.3 shows the band structure for staggered exchange fields (AF model), $\vec{B}^{i}_{stagg} = (-1)^i B_{stagg}\hat{z}$, with $B_{stagg} = \{0.0, 0.4, 1.0\}$ and $\gamma = \{-1.5, 0.0, 1.5\}$. Although the energy bands are split by the field, they are not spin-polarized. Also, the energy spectrum remains gapped regardless the values of γ and B_{stagg}, so that the bulk of the antiferromagnetic model is always insulating.

Now, we keep PBC in x but set open boundary conditions (OBC) in y to obtain a ribbon geometry. The energy spectrum of the ribbon gives information about the edge-states of the system, which is gapped for both trivial and topological phases of the original model, since the metallic states are localized at the corners [159]. Figs. 6.4 and

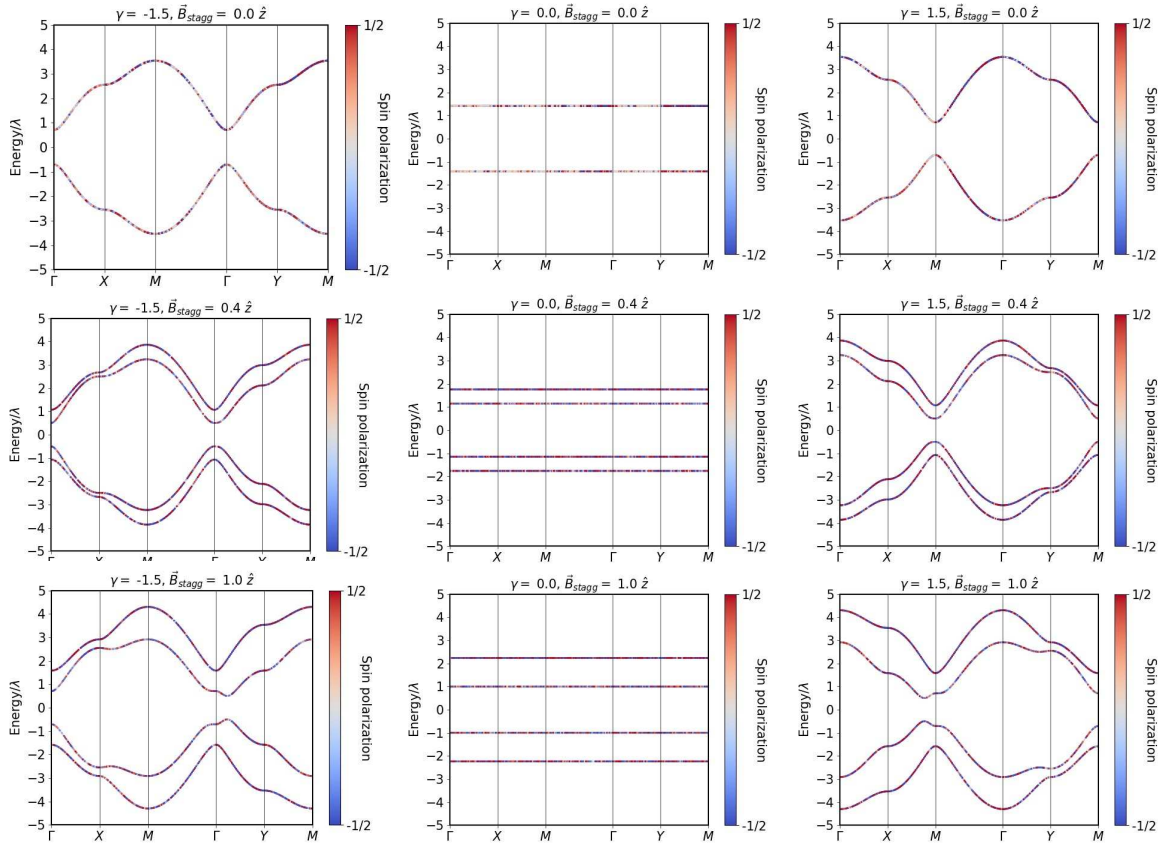

Figure 6.3: Bulk band structure of the AF model ($\vec{B}_i = \vec{B}^i_{stagg}$, along $\hat{z}$) on a 8×8 lattice with PBC. From left to right, each column shows our results for $\gamma = -1.5, 0.0$ and 1.5, respectively. From top to bottom, each line shows our results for $B_{stagg} = 0.0, 0.4$ and 1.0, respectively. The color scale indicates the spin-polarization. Regardless the values of γ and of the staggered exchange field, the bulk of the system is insulating.

6.5 show the band structures of the ribbon system for uniform and staggered exchange fields, respectively. The results are very similar to those of the bulk band structures. For uniform exchange fields, there is splitting and spin-polarization of the energy bands, with a gap closing for higher exchange fields. For staggered exchange fields the energy bands also split but they are not spin-polarized, and the energy gap cannot be closed. This robustness of the bulk and edge energy gaps reinforces our presumption that the topological phase is preserved after including spin and the staggered exchange field, i.e. even changing from spinless to spinful electrons and doubling the number of degrees of freedom, the symmetry criteria for topology appears to be the same.

Finally, we set OBC in both x and y to study the energy spectrum of the corner states. Fig. 6.6 (top panel) shows our results for the FM model with different values of

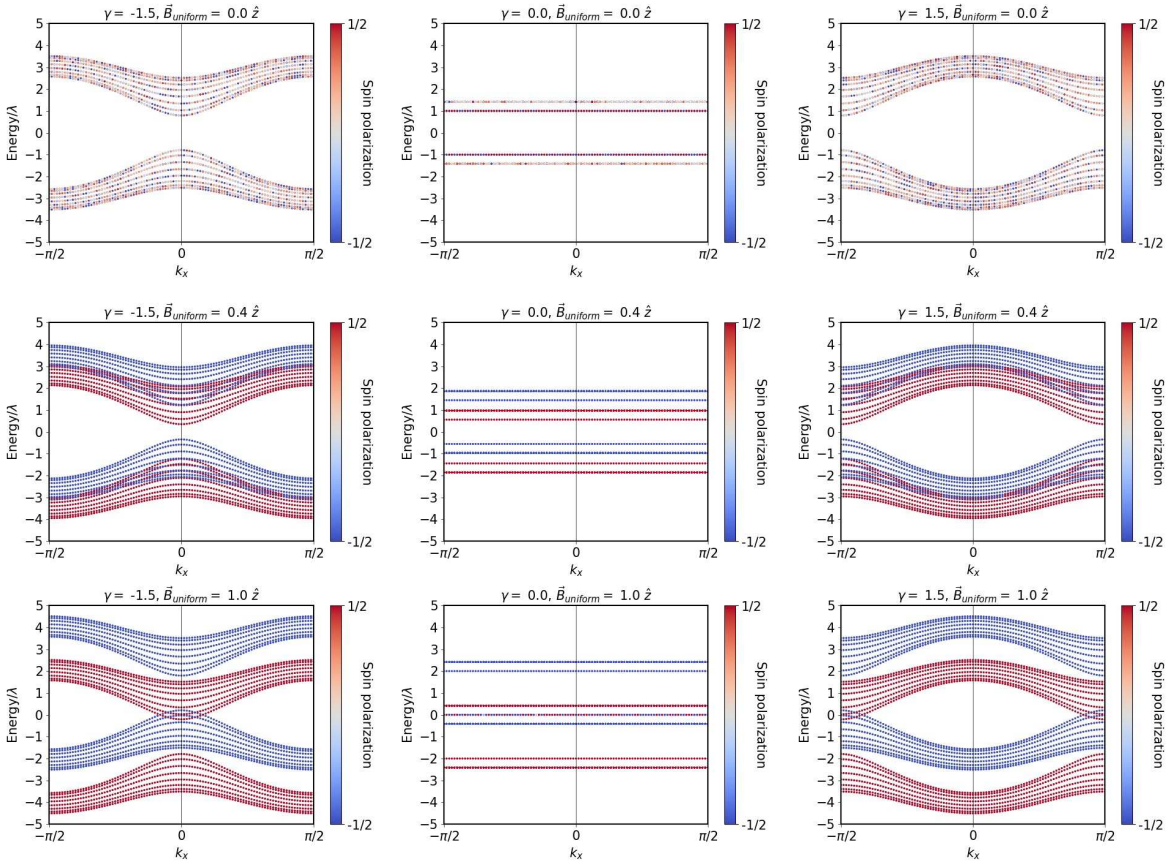

Figure 6.4: Band structure for the FM model on a 8×8 lattice with PBC in x and OBC in y, i.e. a ribbon geometry. The graphs from top to bottom show our results for $B_{uniform} = 0.0, 0.4$ and 1.0, respectively. For $|\gamma| = 1.5$, we see that the energy bands are spin-polarized and the ribbon becomes metallic as we increase the magnitude of the field. For $\gamma = 0$, the bands also become spin-polarized but the ribbon remains insulating.

the uniform exchange field, $B_{uniform} = \{0.0, 0.4, 1.0\}$, and γ varying continuously from -1.5 to 1.5. Again, we can see the Zeeman splitting of the bands, along with their spin-polarization. Naturally, for zero exchange field we recover the results reported by Benalcazar et. al. in Ref. [159] (see Subsection 1.2.4). By increasing the exchange field, the zero energy modes initially localized at the corners are split and end up crossing with the bulk-like states of opposite spin-polarization [Fig. 6.6 (right of top panel)]. In the continuation of this work, we intend to verify if these states are kept localized at the corners or if the exchange field somehow delocalizes the wave functions.

To study the topology of the system, we now investigate the behavior of the WCC's for the ribbon geometry with PBC in x and OBC in y. Fig. 6.6 (bottom panel) shows the WCC's along the y direction for both $k_x = 0$ and $k_y = \pi$, $B_{uniform} = \{0.0, 0.4, 1.0\}$

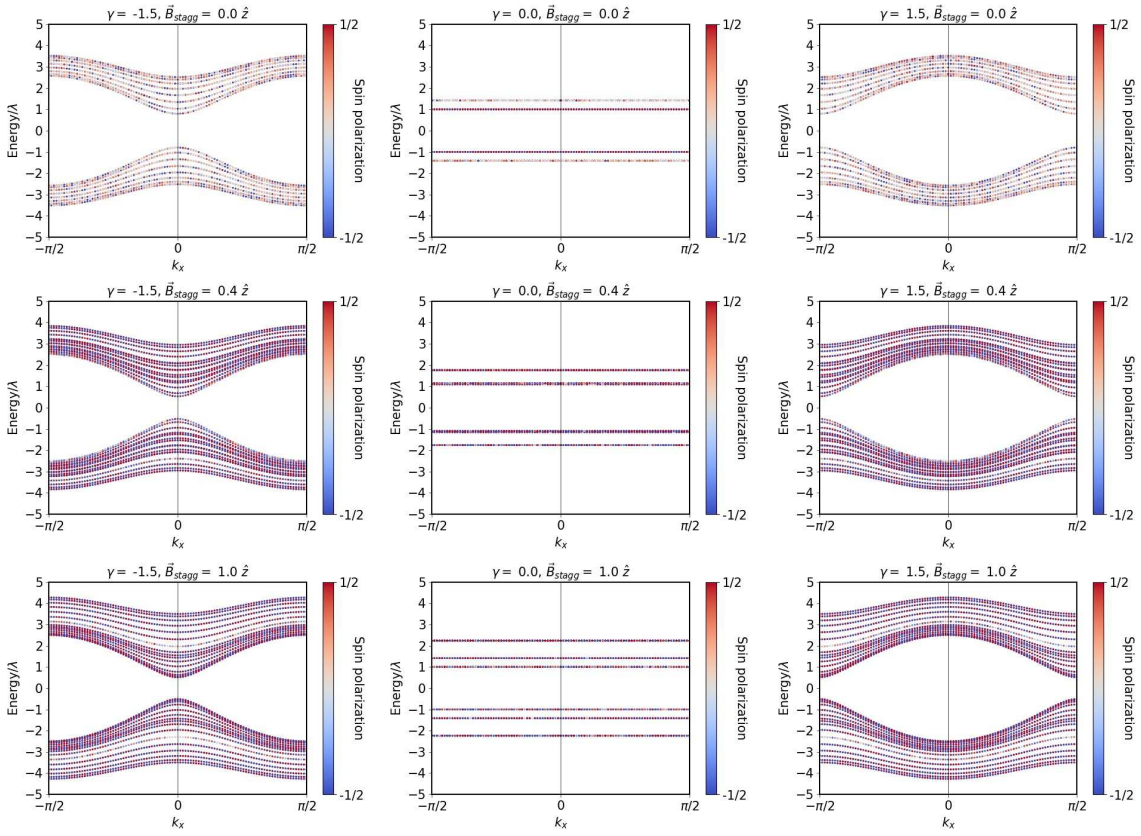

Figure 6.5: Band structure for the AF model on a 8×8 lattice with PBC in x and OBC in y, i.e. a ribbon geometry. The graphs from top to bottom show our results for $B_{stagg} = 0.0, 0.4$ and 1.0, respectively. Regardless the value of γ and B_{stagg}, the ribbon remains insulating and is not spin-polarized.

and $-2 \leq \gamma \leq 2$. Let us consider the graph for $B_{uniform} = 0$ (left of bottom panel) as reference, since we already know which values of γ represent a trivial phase and which ones represent the topological quantized electric quadrupole insulator phase. Focusing our attention on the trivial phase for $\gamma \leq -1$, we can see pairs of WCC's for both $k_x = 0$ and $k_y = \pi$, whose pattern is maintained for all the trivial phase range. As $\gamma \to -1$, the pattern is maintained for $k_y = \pi$, but the WCC's for $k_x = 0$ reverse their polarization, changing their pattern. Therefore, now the polarizations for $k_x = 0$ and $k_y = \pi$ are opposite to each other, so the system enters the topological phase. This is analogous to the inverted time-reversal polarizations for adjacent projections of time-reversal invariant points in TI's [119, 120]. The new pattern is maintained along all the topological phase range, but as $\gamma \to 1$ the polarization for the $k_y = \pi$ centers is also reversed. Since now both end points have the same polarization, the system returns to its topologically trivial

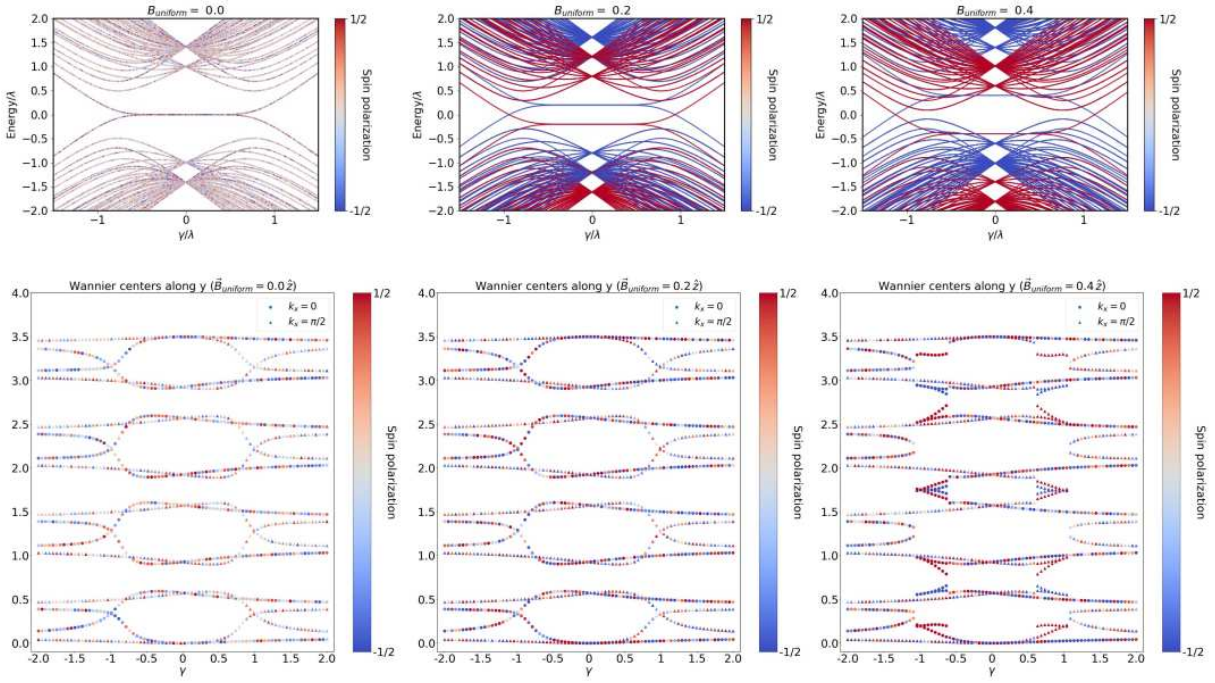

Figure 6.6: (Top panel) Energy spectrum of the FM model on a 8×8 lattice with OBC in x and y, i.e., a finite system with square geometry. The mid-gap horizontal bands for $-1 < \gamma/\lambda < 1$ and $B_{uniform} = 0$ are corner-localized states [159]. For higher values of the field, the energy bands split and become spin-polarized. (Bottom panel) WCC's along y direction for the FM model on a ribbon with PBC in x and OBC in y, in a 10×4 lattice. The circles (triangles) label the WCC's for $k_x = 0$ ($k_x = \pi$). The behavior of the WCC's as function of γ for $B_{uniform} = 0.2$ equals that of the original model, suggesting that the topological phase transition at $\gamma = \pm 1$ is still achieved for small fields. For $B_{uniform} = 0.4$, the pattern is broken and a new phase seems to appear in a region near the $\gamma = \pm 1$ points.

phase.

For small exchange fields ($B_{uniform} = 0.2$; center of bottom panel in Fig. 6.6) we can see that the behavior of the WCC's is exactly the same as that for zero field, which is an indicative that the system preserves the topological phase, even though we have broken the mirror symmetries. This observation remains to be analyzed in more detail. It can also be seen that the WCC's are not spin-polarized, just as for zero exchange field. Looking at the energy spectrum for this case, it appears that the system has both spin-up and spin-down corner-localized states, with an energy gap separating them. For $B_{uniform} = 0.4$ (right of bottom panel in Fig. 6.6), in which the energy bands of the corner-localized states intersect the bulk-like bands, a different behavior of the WCC's manifests. It can be seen that for a small range $-1 < \gamma \lesssim -0.6$ the WCC's for $k_x = 0$ become spin-polarized and present an unusual pattern. For $-0.6 \lesssim \gamma \lesssim 0.6$, it can be seen

that the topological electric quadrupole phase is still present. The same unusual pattern can be observed for $k_y = \pi$ in the range $0.6 \lesssim \gamma \lesssim 1$. A more detailed investigation of the system within the ranges with unusual WCC's pattern will be performed in the continuation of this work.

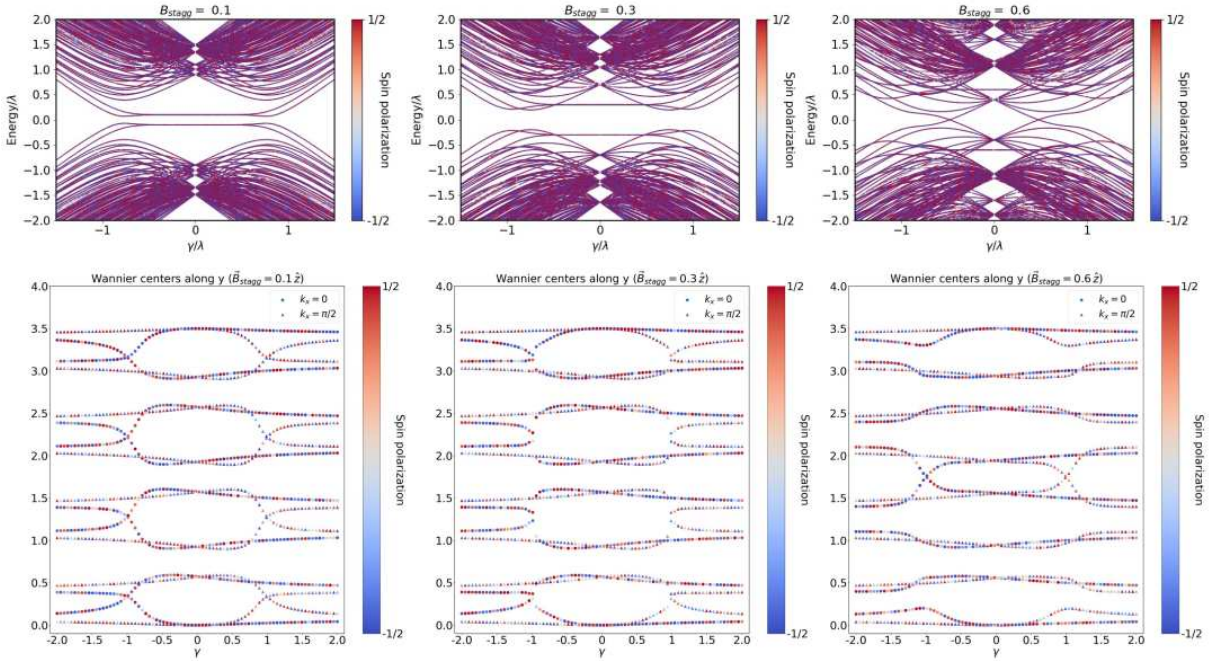

Figure 6.7: (Top panel) Energy spectrum of the AF model on a 8×8 lattice with OBC in x and y, for $B_{stagg} = \{0.1, 0.3, 0.6\}$ and $-1.5 < \gamma/\lambda < 1.5$. The energy bands are not spin-polarized for the staggered field. For $B_{stagg} = 0.1$, the mid-gap horizontal bands split into two degenerate branches, forming a gap in the corner states. For $B_{stagg} = 0.3$, the gap increases and the corner states are pushed towards the bulk-like bands. For $B_{stagg} = 0.6$, the bulk-like bands touch each other, suggesting a possible phase transition. (Bottom panel) WCC's along y direction for the AF model on a ribbon with PBC in x and OBC in y, in a 10×4 lattice. The circles (triangles) label the WCC's for $k_x = 0$ ($k_x = \pi$). The behavior of the WCC's for $B_{stagg} = 0.1$ and $B_{stagg} = 0.3$ suggests that the topological phase transition at $\gamma = \pm 1$ is achieved for small values of the field. For $B_{uniform} = 0.6$, the pattern is changed and a new topological phase seems to be in order for $-1 < \gamma < 1$.

Fig. 6.7 (top panel) shows the energy spectrum for the corner states of the AF model with different values of the staggered exchange field, $B_{stagg} = \{0.1, 0.3, 0.6\}$, and γ varying continuously from -1.5 to 1.5. Notice that, for $B_{stagg} = 0.1$ (left of top panel), an energy gap is opened by the staggered field but the states are not spin-polarized. Also, it can be seen that the bands are degenerate for small γ values. The behavior of the WCC's can be seen in Fig. 6.7 (left of bottom panel) and present the same pattern as that for zero field, which is an indication that that topological phase is still present. We

plan to investigate this in more detail by studying the localization of the wave functions of the horizontal energy bands. For $B_{stagg} = 0.3$ (center of bottom panel), the horizontal bands are lifted and intercept the bulk-like states. Despite the small discontinuity around $\gamma = \pm 1$, it can be seen that the behavior of the WCC's is similar to that for zero exchange field. Therefore, we believe that the quantized electric quadrupole phase can still be found for $-1 < \gamma < 1$, which also remains to be verified.

Interesting and unexpected results are found for both the energy spectrum and WCC's when $B_{stagg} = 0.6$. As the horizontal bands are lifted away from the zero-energy region (Fig. 6.7, right of top panel), the bulk-like valence and conduction bands end up closing the energy gap and connecting with each other. There are two different behaviors for the WCC's in this case (Fig. 6.7, right of bottom panel). For the central region, $1.25 < y < 2.25$, it can be seen that the WCC's reverse their polarization in the $-1 < \gamma < 1$ range. However, there is a subtle difference from the previous cases. When reversing their polarization, a WCC intercepts another coming not from the same unit cell, but from the adjacent one. The WCC's for regions close to the boundaries appears not to reverse their polarization as γ is changed. However, this might be a consequence from the fact that we are calculating the WCC's for a ribbon. We intend to perform this calculations for PBC along both directions in order to recover the periodic behavior of the WCC's. We expect that all WCC's will present similar behavior as those from the central region.

6.4 Tetragonal Copper Manganese Arsenide (CuMnAs)

In this section, we report our preliminary investigations on the existence of edge and/or corner-localized states in the minimal model for tetragonal AF CuMnAs proposed by L. Šmejkal et. al. in Ref. [196]. We anticipate that the main purpose when performing these simulations is to acquire expertise in implementing the tight-binding approach on our search for higher order topology in AF materials with SOC. Although our results are very preliminary, this work was important for our better understanding of systems with topological phases protected by crystal symmetries. The next step is to include new terms in the Hamiltonian that could generate higher order topology.

The tetragonal CuMnAs, in which Mn nearest-neighbors are coupled antiferromag-

netically, can be obtained by epitaxial growth on III-V substrates of GaAs or GaP [191]. As discussed in Subsection 1.2.5, when the Néel vector describing the orientation of the Mn magnetic moments is along the x or y directions, the tetragonal AF CuMnAs is a Dirac semimetal topologically protected by glide mirror plane symmetry about x ($\mathcal{G}_x = \{M_x|\frac{1}{2}00\}$; combination of mirror symmetry along the (100) plane with a half-primitive cell translation along the [100] axis) or y ($\mathcal{G}_y = \{M_y|0\frac{1}{2}0\}$; combination of mirror symmetry along the (010) plane with a half-primitive cell translation along the [010] axis), respectively. Because of this remarkable feature, CuMnAs serves as a platform for the topological metal-insulator transition, in which $\mathcal{G}_x$ (or $\mathcal{G}_y$) is broken by the reorientation of the Néel vector and the model becomes insulating. This can be achieved, for example, by applying an electric current perpendicular to the desired orientation for the Néel vector [189, 196].

We perform numerical calculations of the bulk band structure of CuMnAs for different orientations of the Néel vector, reproducing the main results reported for the minimal model in Ref. [196]. For learning purposes, we have also studied a ferromagnetic variation of such model with magnetization parallel to the xy-plane. Furthermore, we calculate the energy spectrum and WCC's positions for both FM and AF models in a ribbon geometry, as well as the energy spectrum for a finite rectangular sample, for different orientations of the Néel vector.

In Subsection 1.2.5, we have shown the original minimal model Bloch Hamiltonian [Eq. (1.61)] from Ref. [196], which is constructed considering only the Mn atoms of CuMnAs in a stack of crinkled quasi-2D lattices [Fig. 1.19(a)], with the Néel vector lying parallel to the xy-plane. From Eq. (1.61), we derive a tight-binding Hamiltonian that accounts for either FM or AF ordering:

$$\begin{aligned} H = &-t \sum_{\langle i,j\rangle,s,s'} c_{js'}^{(B)\dagger}\sigma_0 c_{is}^{(A)} - t' \sum_{\langle\langle i,j\rangle\rangle,s,s'} \left[c_{js'}^{(A)\dagger}\sigma_0 c_{is}^{(A)} + c_{js'}^{(B)\dagger}\sigma_0 c_{is}^{(B)}\right] \\ &- i\lambda \sum_{\langle\langle i,j\rangle\rangle,s,s'} \left[c_{js'}^{(A)\dagger}\left(\vec{\sigma}\times\vec{d}_{ij}\right)\cdot\hat{z}c_{is}^{(A)} - c_{js'}^{(B)\dagger}\left(\vec{\sigma}\times\vec{d}_{ij}\right)\cdot\hat{z}c_{is}^{(B)}\right] \\ &+ J_n \sum_{i,s,s'} \left[c_{is'}^{(A)\dagger}(\vec{\sigma}\cdot\vec{n})c_{is}^{(A)} \pm c_{is'}^{(B)\dagger}(\vec{\sigma}\cdot\vec{n})c_{is}^{(B)}\right], \end{aligned} \tag{6.12}$$

where $c_i^{(A)\dagger}$ ($c_i^{(B)\dagger}$) and $c_i^{(A)}$ ($c_i^{(B)}$) are the electron creation and annihilation operators in sublattice A (B) of the unit cell in site i, respectively. σ_0 is the 2×2 identity matrix, $\vec{\sigma} = (\sigma_x, \sigma_y, \sigma_z)$ is the Pauli vector representing the spin degrees of freedom and $\vec{d}_{ij}$ is a

vector connecting site i to site j. The parameters t, t', λ and J_n are the nearest-neighbor hopping, next-nearest-neighbor hopping (intrasublattice hopping), next-nearest-neighbor SOC and the AF exchange coupling, respectively. In the last term of the Hamiltonian, $\pm$ accounts for either ferromagnetic (+) or antiferromagnetic (−) order. $\vec{n}$ represents either the magnetization direction for the FM model or the Néel vector for the AF model.

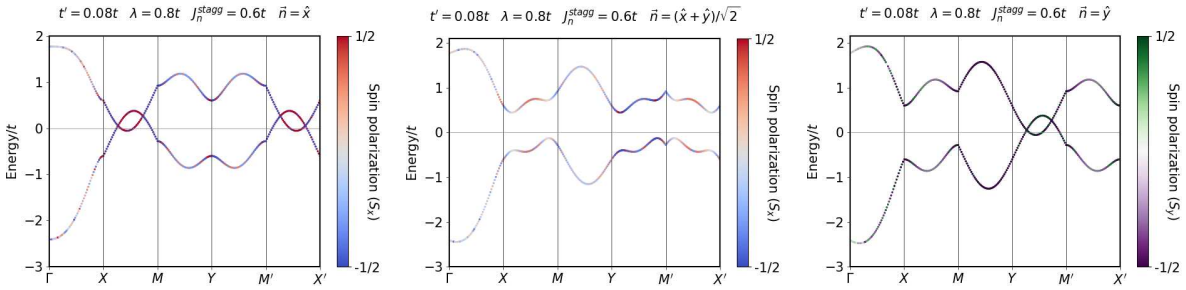

Figure 6.8: Bulk band structure for the AF model on a 5×5 lattice with PBC in x and y. The orientation of the Néel vector $\vec{n}$ is indicated at the top of each panel, along with the model parameters. The red-blue (green-purple) color scale represents the spin-polarization [Eq. (6.4)] along the x (y) direction. If $\vec{n} = \hat{x}$ or $\vec{n} = \hat{y}$, glide mirror plane symmetry is preserved, protecting the band crossings so that the system is in a metallic phase. If $\vec{n} = (\hat{x} + \hat{y})/\sqrt{2}$, glide mirror plane symmetry is broken and the bands interact. In this case, a gap is opened and the system becomes insulating.

We start with the results for the AF model with PBC in both x and y. Fig. 6.8 shows the bulk band structures for three distinct orientations of the Néel vector; namely $\vec{n} = \hat{x}$, $\vec{n} = (\hat{x}+\hat{y})/\sqrt{2}$ and $\vec{n} = \hat{y}$. In order to compare our results with their calculations, we have used the same parameters provided in Ref. [196], i.e. $t' = 0.08t$, $\lambda = 0.8t$ and $J_n^{stagg} = 0.6t$ [$stagg$ indicates that we have used the minus sign in the last term of Eq. (6.12)]. Notice that the energy bands are doubly degenerate over all the BZ. This is because the AF CuMnAs is symmetric under the combined $\mathcal{PT}$ symmetry ($\mathcal{P}$ is the space inversion and $\mathcal{T}$ is the TRS), although both $\mathcal{P}$ and $\mathcal{T}$ are broken individually. In analogy to the Kramers degeneracy for $\mathcal{T}$-invariant systems, two orthogonal states of opposite spins are guaranteed to be degenerate at the same $\vec{k}$-point over the whole BZ[1] [196]. Our results for the bulk band structure are exactly the same reported in Ref. [196]. For the Néel vector along the x (y) direction, band crossings appear and are protected by glide mirror plane symmetry $\mathcal{G}_x$ ($\mathcal{G}_y$). In such case the model is in a metallic phase. On the

[1]It can be shown that $[H, \mathcal{PT}] = 0 \Rightarrow \mathcal{PT}\mathcal{H}(\vec{k})(\mathcal{PT})^{-1} = \mathcal{H}(\vec{k})$, where H is given by Eq. (6.12) and $\mathcal{H}(\vec{k}) \equiv e^{-i\vec{k}\cdot\vec{r}} H e^{i\vec{k}\cdot\vec{r}}$ is the Bloch Hamiltonian. Furthermore, the Bloch eigenstates $|u_n(\vec{k})\rangle$ and $\mathcal{PT}|u_n(\vec{k})\rangle$ are orthogonal, since $(\mathcal{PT})^2 = -1$ [245]. As a result, for each $\vec{k}$-vector there are two orthogonal states with the same energy.

other hand, for the Néel vector along the $\vec{n} = (\hat{x} + \hat{y})/\sqrt{2}$ direction, neither $\mathcal{G}_x$ nor $\mathcal{G}_y$ symmetry is preserved, so that a gap is opened and the bulk is insulating. The color scale indicates the spin-polarization [Eq. (6.4)] for each $\vec{k}$-point in the BZ. However, it is not clear from the graph if the energy bands are spin-polarized or not, because the overlap of the degenerate bands is preventing the proper visualization of their coloring. We intend to perform projections of the energy bands also on the orbital degrees of freedom in order to obtain a clearer picture of the spin-polarization.

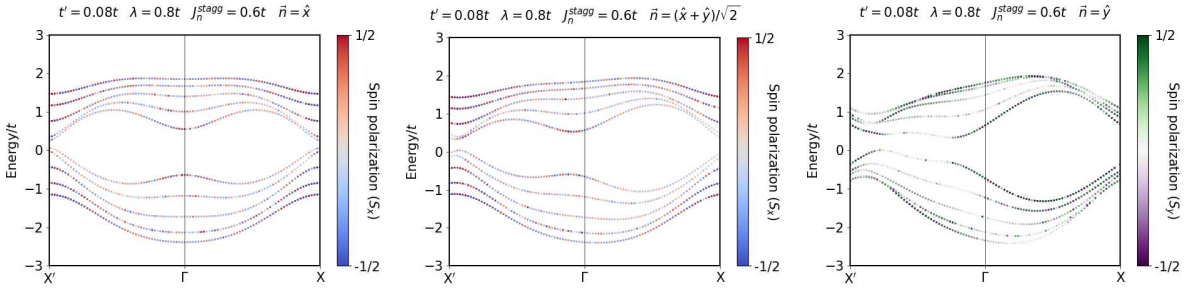

Figure 6.9: Energy band structure for the AF model on a 5×5 lattice with PBC in x and OBC y, constituting a ribbon geometry. There is an energy gap for any orientation of the Néel vector $\vec{n}$ and, therefore, the ribbon is insulating. The appearance of such gap for the ribbon geometry is very likely due to the finite size effect.

Fig. 6.9 shows the band structures for the AF model in a ribbon geometry, with PBC in x and OBC in y. As the system with ribbon geometry is also invariant under $\mathcal{PT}$ symmetry, the energy bands are doubly degenerate over all the edge BZ. The energy spectrum of the ribbon is gapped regardless the orientation of the the Néel vector, so the ribbon is insulating. We plan to study the energy spectrum of the ribbon for different widths in order to be sure if the origin of the energy gap is the finite size effect, in which wave functions tend to hybridize. Once again, it is not clear from the graphs if the energy bands are spin-polarized or not, due to degeneracy.

In Fig. 6.10 (left panel), we show the energy spectrum for the AF model with OBC in both x and y, as a function of the azimuthal angle between the Néel vector and the x-axis. The spectrum is gapped regardless the orientation of the Néel vector. Fig. 6.10 (right panel) shows the WCC's along the y direction for the AF model in a ribbon geometry with PBC in x and OBC in y. The WCC's are localized approximately at the same positions as the fixed Mn atoms and, as could be expected, are polarized according to the magnetic moments of the atoms in each sublattice. As the Néel vector is rotated parallel to the xy-plane, the spin-polarization of the WCC's changes with the magnetic

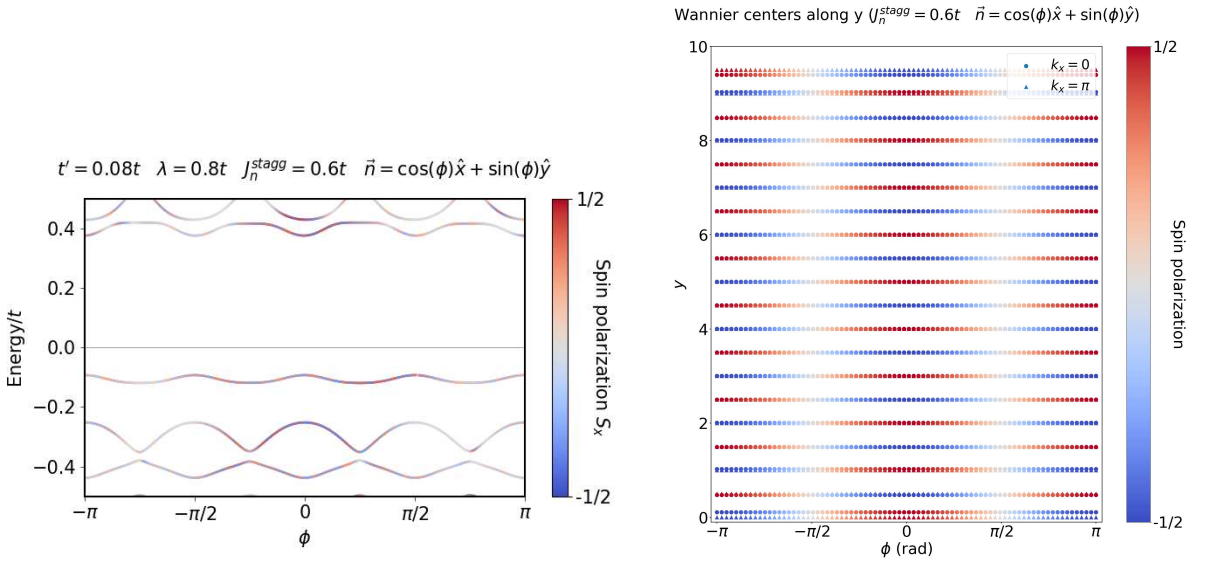

Figure 6.10: (Left panel) Energy spectrum for the AF model on a 10×10 lattice with OBC in both x and y. There is an energy gap regardless of the orientation of the Néel vector, which shows that there are no corner-localized metallic states for this model. (Right panel) WCC's along the y direction for the AF model on a 10×10 lattice with PBC in x and OBC in y. ϕ is the azimuthal angle of the Néel vector relative to the x-axis. The WCC's are located at the same positions of the Mn atoms in each sublattice, with spin-polarization following the direction of their magnetic moments.

moments of the Mn atoms, reversing their sign at $\phi = \pm\pi/2$. As the behavior of the WCC's positions with the variation of ϕ is trivial, there is no evidence of higher topology in the AF model.

Now, we turn to the results for the FM model with PBC in both x and y. Fig. 6.11 shows the bulk band structures for three distinct orientations of the magnetization direction. For the sake of comparison, we have used the same parameters as in the AF model, i.e. $t' = 0.08t$, $\lambda = 0.8t$ and $J_n^{uniform} = 0.6t$ [$uniform$ indicates that we have used the plus sign in the last term of Eq. (6.12)]. Now, as the $\mathcal{PT}$ symmetry is broken by the uniform magnetization, the energy bands are no longer doubly degenerate over all the BZ. Notice that $\mathcal{G}_x$ ($\mathcal{G}_y$) is preserved even for the FM model, as long as the magnetization is along the x (y) direction. As a result, band crossings are also present and protected, and the model is in a metallic phase. As neither $\mathcal{G}_x$ nor $\mathcal{G}_y$ symmetry is preserved when $\vec{n} = (\hat{x} + \hat{y})/\sqrt{2}$, a gap is opened and the bulk is insulating in this situation. Therefore, the topological metal-insulator transition seems to be achievable also in the FM model. One can see that the spin-polarization, defined in Section 6.2 as the expectation value of the spin operator for a particular Bloch eigenstate [$\langle\psi_{n\vec{k}}|\sigma_i/2|\psi_{n\vec{k}}\rangle$, Eq. (6.4)], varies with

the crystal momentum $\vec{k}$ due to SOC.

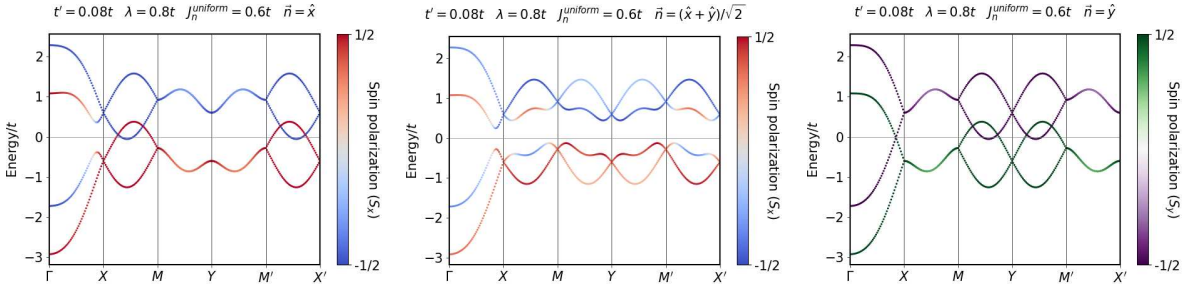

Figure 6.11: Bulk band structure for the FM model on a 5×5 lattice with PBC in x and y. The model parameters and the orientation of the magnetization $\vec{n}$ are indicated at the top of each graph. The red-blue (green-purple) color scale represents the $\vec{k}$-dependent spin-polarization [Eq. (6.4)] along the x (y) direction. If $\vec{n} = \hat{x}$ or $\vec{n} = \hat{y}$, glide mirror plane symmetry is preserved, protecting the band crossings so that the system is in a metallic phase. If $\vec{n} = (\hat{x} + \hat{y})/\sqrt{2}$, glide mirror plane symmetry is broken and the bands interact. In this case, a gap is opened and the system becomes insulating.

Fig. 6.12 shows the band structures for the FM model on a ribbon geometry with PBC in x and OBC in y. Just as for the bulk band structure, the energy bands for the ribbon are split by the $\mathcal{PT}$-breaking magnetization. When the magnetization is oriented along the $\vec{n} = \hat{x}$ or $\vec{n} = (\hat{x}+\hat{y})\sqrt{2}$ directions, the band structure is gapped and the ribbon is insulating. On the other hand, the gap is closed for $\vec{n} = \hat{y}$ and metallic states appear in the ribbon. This result can be a starting point for the construction of a FM TCI model hosting a topological edge-state metal-insulator transition [in analogy to the topological (bulk) metal-insulator transition in Ref. [196]] mediated by the uniform magnetization. Again, as a result of the coupling between spin and momentum due to the SOC, the spin-polarization of the energy bands varies with the crystal momentum $\vec{k}$.

In Fig. 6.13 (left panel), we show the energy spectrum for the FM model with OBC in both x and y as a function of the azimuthal angle between the magnetization direction and the x-axis. The band structure is gapped regardless the orientation of the magnetization. Fig. 6.13 (right panel) shows the WCC's along the y direction for the FM model in a ribbon geometry, with PBC in x and OBC in y. The polarization of the WCC's are also reversed when $\phi = \pm\pi/2$, but notice that the uniform magnetization splits their degeneracy. Just as for the AF model, the behavior of the WCC's positions with the variation of ϕ in the FM is trivial. Therefore, there is no evidence of higher topology in the Hamiltonian (6.12).

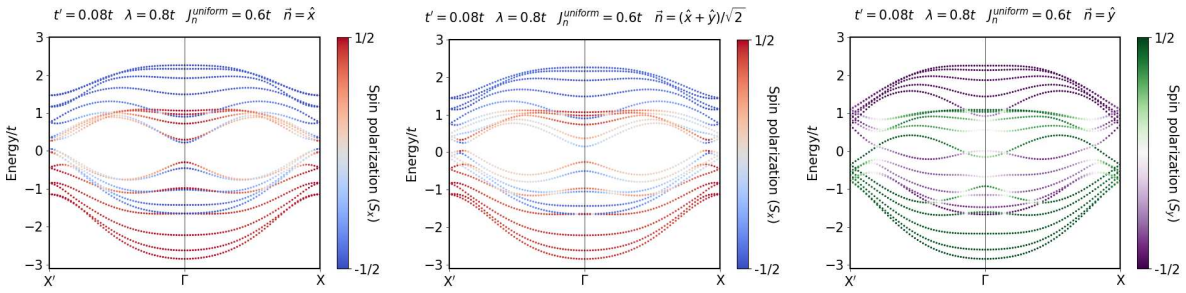

Figure 6.12: Energy band structure for the FM model on a 5×5 lattice with PBC in x and OBC in y, constituting a ribbon geometry. If the magnetization vector reads $\vec{n} = \hat{x}$ or $\vec{n} = (\hat{x} + \hat{y})/\sqrt{2}$, a small gap is opened and the ribbon becomes insulating. If $\vec{n} = \hat{y}$, the band structure has no gap and the ribbon is in a metallic phase. The $\vec{k}$-dependent spin polarization along x or y are indicted by the red-blue and green-purple color scales, respectively.

6.5 Conclusions and prospects

We have analyzed the higher order topology of electronic band structures in 2D ferromagnetic and antiferromagnetic models. For this, we calculate the energy spectrum of both ribbon and square geometries and the corresponding positions of their Wannier charge centers.

For the spinful 2D SSH model with ferromagnetic order, we have found that the uniform exchange field causes the splitting and spin-polarization of the energy bands, as can be expected. Furthermore, the initially gapped energy spectrum of both periodic and ribbon systems become metallic as the strength of the coupling between electrons spin and atomic magnetic moments increases. Inspection of the Wannier charge centers have indicated that aspects of the topological phase of the original model [159] are preserved in the presence of magnetization. We believe that in this case the electric polarization (which is protected by the preserved space inversion symmetry) remains quantized, while the electric quadrupole moment (protected by the mirror symmetries about x and y, broken by the magnetization) does not. Further analysis will be made to confirm this hypothesis. For higher values of the coupling between spin and the uniform exchange field, the horizontal bands of the corner energy spectrum intercept the bulk-like conduction/valence bands. Simultaneously, a new phase seems to appear, in which the Wannier charge centers at specific terminations have their degeneracy lift and become spin-polarized. These two results are probably related and we hope to have a clearer picture of their physical consequences soon.

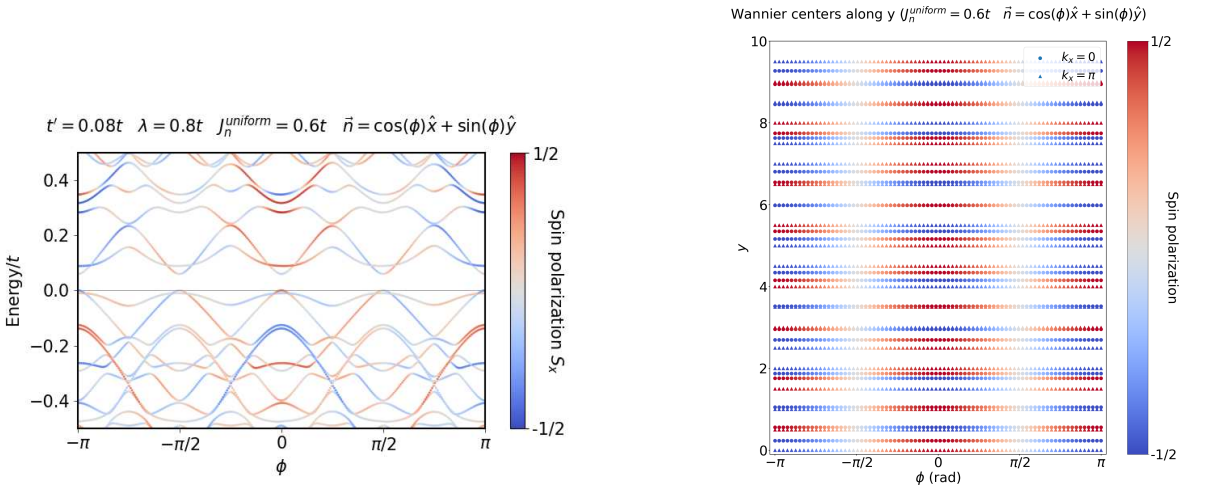

Figure 6.13: (Left panel) Energy spectrum for the FM model on a 10×10 lattice with OBC in both x and y. There is an energy gap regardless of the orientation of the magnetization vector $\vec{n}$, indicating that there are no corner-localized metallic states for this model. (Right panel) WCC's along the y direction for the FM model on a 10×10 lattice with PBC in x and OBC in y. ϕ is the azimuthal angle of the magnetization vector relative to the x-axis. The $\vec{k}$-dependent spin-polarizations of the WCC's reverse their sign at $\phi = \pm\pi/2$, but do not intercept, which also indicates that the model has no higher order topology.

For the antiferromagnetic variation of the spinful 2D SSH model, the exchange field also split the degeneracy of the bands, but they do not become spin-polarized. By studying the energy spectrum of the system with either periodic boundary conditions and in a ribbon geometry, we have seen that both bulk and edges of the system remain insulating regardless the strength of the exchange field. The antiferromagnetic order does not break either the space inversion or mirror symmetries protecting the quantized electric quadrupole moment. The analysis of the Wannier charge centers shows that, apparently, the higher order topology with corner-localized states is still present in this case, although a gap appears between the horizontal bands of the corner energy spectrum. For strong coupling between the spin and the exchange field, the bulk-like valence and conduction bands enter the gap between the horizontal bands and connect to each-other. From the Wannier charge centers analysis for this case, it seems that a new topological phase appears, in which the Wannier charge centers migrate from the unit cell to the adjacent one.

We have also studied a minimal model inspired by the tetragonal antiferromagnetic CuMnAs, which hosts the topological metal-insulator transition [196]. This model describes a Dirac semi-metal when the Néel vector preserves mirror glide plane symmetry

about x or y, but becomes a trivial insulator otherwise. By calculating the energy spectrum of this model on both ribbon and square geometries, we have shown that both edges and corners are insulating, regardless the orientation of the Néel vector. Although the Wannier charge centers indicate trivial higher order topology, they become spin-polarized according to the magnetic moments in the adjacent sublattices. For the ferromagnetic version of this model, our calculations show that the direction of the magnetization can also be used to induce a topological metal-insulator transition. In fact, the mirror glide plane symmetry about x or y is preserved when the magnetization is parallel to the respective axis, and broken otherwise. Furthermore, the uniform magnetization (along with SOC) leads to the $\vec{k}$-dependent spin-polarization of the bands, which does not happen for the antiferromagnetic model. The band structure calculations for the ferromagnetic model on a ribbon geometry have shown that the magnetization direction can also be used to manipulate the gap closing of the ribbon energy states. In fact, when the system is magnetized along the ribbon, it is insulating. On the other hand, a transversal magnetization closes the energy gap and the ribbon becomes metallic. The energy spectrum for the corner states is gapped regardless the direction of the magnetization vector. Furthermore, in the ferromagnetic version the Wannier charge centers not only become spin-polarized but also split their degeneracy, reversing their spin-polarization according to the magnetization direction.

Although our results are preliminary, this work has provided us with an important understating of higher order topology in magnetic systems and numerical calculations in the tight-binding approach. Such experience will be very beneficial to our goal of proposing a generalization from quantized electric multipoles to quantized magnetic multipoles. We also intend to expand our investigations to more complex and realistic systems, as well as to investigate in which materials the effects predicted here could be realized.

Chapter 7

Final conclusions and prospects

In this thesis we have summarized the main results of our research in two very different and celebrated areas of physics. Namely, optical tweezers (OT), which allows for the trapping and manipulation of microscopic objects with a focused laser beam, and topological states of matter, with unique electronic properties that cannot be described by conventional spontaneous-symmetry-breaking related phase transition theories.

We have shown that Bi_2Te_3 and Bi_2Se_3 topological insulator (TI) microparticles behave like optically induced oscillators whenever subject to a highly focused Gaussian laser beam OT. Such dynamics results from a delicate balance in the competition between gradient and radiometric forces. The period of oscillations is well-defined in time, remaining virtually constant during a number of cycles. We have also observed that frequency and amplitude of oscillations depend on both particle size and power of the laser beam, providing additional control over the system. The optically induced oscillations are not restricted to TI beads, as we have reported that they also take place for germanium (Ge) microparticles in a similar setup. We have observed that the oscillation direction of the Ge particles can be controlled by the polarization of the laser beam. Such a novel feature could be very useful in applications, as it would allow for dynamic measurements along a defined direction. Our approach suggests a new application for semiconductors, opening an avenue of possibilities for the application of such materials in OT. In fact, it was recently reported that these optically induced oscillations also take place for silicon microparticles [77], indicating that this effect may be typical of conventional semiconductor materials.

We also propose an effective model to explain the optically induced oscillations,

based on the competition between radiometric and gradient forces. The model is shown to reproduce the experimental data with good accuracy, and successfully captures the strong asymmetry on the optical force observed for the germanium microparticles. Furthermore, we propose a generalization of the well-known Ashkin's model for optical tweezers in the geometrical optics regime. The model is extended for inclusion of the radiation pressure generated by absorption of light in the bulk of the particle. Our results account for an arbitrary value of the absorption coefficient in the bulk of the bead, including the two limiting cases previously studied in the literature, namely, perfectly dielectric and perfectly metallic particles. Our findings suggest that attenuation effects becomes important mainly when the skin depth is comparable to the particle size. This result is important for a complete understanding of the optically induced oscillations, since a microscopic description of the phenomena requires a separation of the individual contributions of radiometric and radiative forces. We show that our generalization significantly improves the comparison of the Ashkin's model with the radiative force obtained in the experiments with TI particles in OT.

In addition to the works discussed above, it is worth mentioning our recent/ongoing collaborations, such as the investigation on the trapping of superparamagnetic beads in an annular-shaped laser beam [21] [L. Oliveira, W. H. Campos and M. S. Rocha, *Meth. Protoc.* **1**(4), 44 (2018)] and the calculation of the Kerr topological force exerted on magnetically caped TI particles in OT [Y. Müller, W. H. Campos et. al., *work in progress*].

Our results open an avenue for dynamical force measurements with unprecedented simplicity and purely optical control. Among the possible applications, stand out the optical rheology of soft matter interfaces and biological membranes, as well as single molecule biophysics and dynamical force measurements in macromolecules, colloid science and biopolymers. In fact, oscillatory dynamics often appears in studies of biological systems, in which a piezoelectric stage is used for the manipulations. In contrast, the optically induced oscillations do not require any mechanical interventions on the laser setup, so that oscillatory forces can be implemented in a much more suitable way. Furthermore, our investigations indicate that this recently discovered effect constitute a very rich scenario for the experimental realization of a single-particle thermal machine in OT.

In our recent investigations, we have shown that an electric charge placed near a semispherical TI cavity induces a surface Hall current which reverses its rotation whenever

the charge crosses the semisphere focus. Such a current is known to generate a magnetic field analogous that produced by an image magnetic monopole, so that the Hall current reversion is equivalent to reversing the sign of the magnetic monopole. Here, we show that an electrically charged wire near a semi-cylindrical cavity in a TI can be used to induce a simultaneous Hall current reversion of the antiparallel channels on its surface.

We have performed a higher order topology analysis of electronic band structures in 2D ferromagnetic (FM) and antiferromagnetic (AF) models by calculating their energy spectrum in both ribbon and square geometries, along with the corresponding positions of their Wannier charge centers. For the spinful 2D SSH model with FM order, the energy band spectrum becomes spin-polarized and its degeneracy is split by the uniform magnetization, as can be expected. Inspection of the Wannier charge centers indicates that, in the presence of a small magnetization, their behavior as function of the model parameters is preserved, suggesting that corner-localized metallic states are still in place. For higher values of the coupling between spin and magnetization, a new phase seems to appear, in which the degeneracy of the Wannier centers at specific terminations is split and they become spin-polarized. For the AF variation of this model, although the exchange field also split the degeneracy of the bands, they do not become spin-polarized. The analysis of the Wannier centers in this case shows that, apparently, the higher order topology with corner-localized states is still present, although a gap appears between the horizontal bands of the corner energy spectrum. For strong coupling between the spin and the exchange field, it seems that a new topological phase appears, in which the bulk-like conduction and valence bands connect to each other and the Wannier centers migrate from a unit cell to the adjacent one as the model parameters are varied.

We have also studied a minimal model inspired by the tetragonal AF CuMnAs, which hosts the topological metal-insulator transition. Our analysis have shown that both edges and corners of the system are insulating, regardless the orientation of the Néel vector. Despite trivial higher order topology, the Wannier charge centers become spin-polarized according to the atomic magnetic moments in the adjacent sublattices. Our calculations for the FM version of this model have also manifested topological metal-insulator transition, in which the magnetization direction determines the phase. The band structure calculations for the FM model on a ribbon geometry have shown that the magnetization direction can also be used to manipulate the gap closing of the spin-

polarized energy bands of the ribbon. In fact, when the system is magnetized along the ribbon, the edges are insulating. On the other hand, a perpendicular magnetization closes the energy gap and the edges become metallic. The corner energy spectrum is gapped regardless the direction of the magnetization vector. Furthermore, in addition to reversing their spin-polarization according to the magnetization direction, the Wannier charge centers in the FM version also experience a splitting of their degeneracy.

Our results regarding the higher order topology analysis of electronic band structures on magnetic models are preliminary. However, they represent an important step forward towards our goal of proposing topological systems with quantized magnetic multipoles. We have also been expanding our investigations to more complex and realistic systems, to predict in which materials our results could be observed experimentally.

Due to their unique properties, both topological materials and magnetism have been the subject of intense research of condensed matter physicists in the last decade. The strong spin-orbit coupling in TI's leads to important effects, such as the conversion of charge current into spin current and vice-versa. New topological materials have been discovered at an unbelievable pace, and further examples include Weyl and Dirac semimetals, topological superconductors, Majorana fermions, topological crystalline insulators and higher order TI's. These materials have been quoted as promising candidates for near future technology, with possibilities for applications in spintronics, quantum computation and advanced devices with low-energy dissipation.

References

[1] W. H. Campos, J. M. Fonseca, V. E. de Carvalho, J. B. S. Mendes, M. S. Rocha, and W. A. Moura-Melo, "Topological insulator particles as optically induced oscillators: Toward dynamical force measurements and optical rheology," *ACS Photonics*, vol. 5, no. 3, pp. 741–745, 2018.

[2] A. Ashkin, "Forces of a single-beam gradient laser trap on a dielectric sphere in the ray optics regime," *Biophys. J.*, vol. 61, pp. 569–582, 1992.

[3] R. Gauthier and S. Wallace, "Optical levitation of spheres: analytical development and numerical computations of the force equations," *J. Opt. Soc. Am. B*, vol. 12, no. 9, pp. 1680–1686, 1995.

[4] J. P. Gordon, "Radiation forces and momenta in dielectric media," *Phys. Rev. A*, vol. 8, no. 1, p. 14, 1973.

[5] A. Mazolli, P. A. M. Neto, and H. M. Nussenzveig, "Theory of trapping forces in optical tweezers," *Proc. R. Soc. Lond. A*, vol. 459, no. 2040, pp. 3021–3041, 2003.

[6] R. S. Dutra, N. B. Viana, P. A. Maia Neto, and H. M. Nussenzveig, "Absolute calibration of optical tweezers including aberrations," *Appl. Phys. Lett.*, vol. 100, no. 13, p. 131115, 2012.

[7] W. H. Campos, J. M. Fonseca, J. B. Mendes, M. S. Rocha, and W. A. Moura-Melo, "How light absorption modifies the radiative force on a microparticle in optical tweezers," *Appl. Opt.*, vol. 57, no. 25, pp. 7216–7224, 2018.

[8] W. Campos, T. Moura, O. Marques, J. Fonseca, W. Moura-Melo, M. Rocha, and J. Mendes, "Germanium microparticles as optically induced oscillators in optical tweezers," *Phys. Rev. Research*, vol. 1, no. 3, p. 033119, 2019.

[9] W. H. Campos, W. A. Moura-Melo, and J. M. Fonseca, "Geometrically induced reversion of Hall current in a topological insulator cavity," *Phys. Lett. A*, vol. 381, no. 5, pp. 417 – 421, 2017.

[10] A. Ashkin, "Acceleration and trapping of particles by radiation pressure," *Phys. Rev. Lett.*, vol. 24, no. 4, pp. 156–159, 1970.

[11] A. Ashkin and J. Dziedzic, "Optical levitation by radiation pressure," *Appl. Phys. Lett.*, vol. 19, no. 8, pp. 283–285, 1971.

[12] A. Ashkin and J. M. Dziedzic, "Optical trapping and manipulation of viruses and bacteria," *Science*, vol. 235, pp. 1517–1521, 1987.

[13] K. Tych, V. K. Hechtl, and S. Mandal, "The power of light: Nobel prize in physics 2018," *IEEE Pulse*, vol. 10, no. 2, pp. 14–19, 2019.

[14] K. Dholakia and T. Čižmár, "Shaping the future of manipulation," *Nat. Photonics*, vol. 5, no. 6, pp. 335–342, 2011.

[15] J. E. Molloy and M. J. Padgett, "Lights, action: optical tweezers," *Contemp. Phys.*, vol. 43, no. 4, pp. 241–258, 2002.

[16] D. G. Grier, "A revolution in optical manipulation," *Nature*, vol. 424, no. 6950, pp. 810–816, 2003.

[17] K. C. Neuman and S. M. Block, "Optical trapping," *Rev. Sci. Instrum.*, vol. 75, no. 9, pp. 2787–2809, 2004.

[18] M. S. Rocha, "Optical tweezers for undergraduates: Theoretical analysis and experiments," *Am. J. Phys.*, vol. 77, no. 704, pp. 704–712, 2009.

[19] H. M. Nussenzveig, "Cell membrane biophysics with optical tweezers," *Eur. Biophys. J.*, vol. 47, pp. 499–514, 2018.

[20] S. E. S. Spesyvtseva and K. Dholakia, "Trapping in a material world," *ACS Photonics*, vol. 3, no. 5, pp. 719–736, 2016.

[21] L. Oliveira, W. H. Campos, and M. S. Rocha, "Optical trapping and manipulation of superparamagnetic beads using annular-shaped beams," *Methods Protoc.*, vol. 1, no. 4, p. 44, 2018.

[22] N. Viana, A. Mazolli, P. Maia Neto, H. Nussenzveig, M. Rocha, and O. Mesquita, "Absolute calibration of optical tweezers," *Appl. Phys. Lett.*, vol. 88, no. 13, p. 131110, 2006.

[23] N. B. Viana, M. S. Rocha, O. N. Mesquita, A. Mazolli, P. A. M. Neto, and H. M. Nussenzveig, "Towards absolute calibration of optical tweezers," *Phys. Rev. E*, vol. 75, no. 2, p. 021914, 2007.

[24] http://eea.spaceflight.esa.int/portal/exp/?id=9283 (2020).

[25] A. Ashkin, "How it all began," *Nat. Photonics*, vol. 5, pp. 316–317, 2011.

[26] M. A. Taylor, M. Waleed, A. B. Stilgoe, H. Rubinsztein-Dunlop, and W. P. Bowen, "Enhanced optical trapping via structured scattering," *Nat. Photonics*, vol. 9, no. 10, p. 669, 2015.

[27] C. Bustamante, S. B. Smith, J. Liphardt, and D. Smith, "Single-molecule studies of DNA mechanics," *Curr. Opin. Struct. Biol.*, vol. 10, no. 3, pp. 279–285, 2000.

[28] A. Ashkin, "History of optical trapping and manipulation of small-neutral particle, atoms, and molecules," *IEEE J. Sel. Top. Quantum Electron.*, vol. 6, no. 6, pp. 841–856, 2000.

[29] K. Svoboda, P. P. Mitra, and S. M. Block, "Fluctuation analysis of motor protein movement and single enzyme kinetics," *Proc. Natl. Acad. Sci. U.S.A.*, vol. 91, no. 25, pp. 11782–11786, 1994.

[30] L. Oliveira and M. S. Rocha, "Force spectroscopy unravels the role of ionic strength on DNA-cisplatin interaction: Modulating the binding parameters," *Phys. Rev. E*, vol. 96, no. 3, p. 032408, 2017.

[31] D. Gao, W. Ding, M. Nieto-Vesperinas, X. Ding, M. Rahman, T. Zhang, C. Lim, and C.-W. Qiu, "Optical manipulation from the microscale to the nanoscale: fundamentals, advances and prospects," *Light Sci. Appl.*, vol. 6, p. e17039, 2017.

[32] K. Hayashi, S. Hasegawa, T. Sagawa, S. Tasaki, and S. Niwa, "Non-invasive force measurement reveals the number of active kinesins on a synaptic vesicle precursor in axonal transport regulated by ARL-8," *Phys. Chem. Chem. Phys.*, vol. 20, pp. 3403–3410, 2018.

[33] L. Jiang, S. Yang, B. Tsang, M. Tu, and S. Granick, "Vector assembly of colloids on monolayer substrates," *Nat. Commun.*, vol. 8, p. 15778, 2017.

[34] K. Svoboda and S. M. Block, "Biological applications of optical forces.," *Annu. Rev. Biophys. Biomol. Struct.*, vol. 23, pp. 247–285, 1994.

[35] M. D. Wang, H. Yin, R. Landick, J. Gelles, and S. M. Block, "Stretching DNA with optical tweezers," *Biophys. J.*, vol. 72, pp. 1335–1346, 1997.

[36] P. M. Hansen, V. K. Bhatia, N. Harrit, and L. Oddershede, "Expanding the optical trapping range of gold nanoparticles," *Nano Lett.*, vol. 5, pp. 1937–1942, 2005.

[37] P. J. Reece, W. J. Toe, F. Wang, S. Paiman, Q. Gao, H. H. Tan, and C. Jagadish, "Characterization of semiconductor nanowires using optical tweezers," *Nano Lett.*, vol. 11, pp. 2375–2381, 2011.

[38] L. Bosanac, T. Aabo, P. M. Bendix, and L. B. Oddershede, "Efficient optical trapping and visualization of silver nanoparticles," *Nano Lett.*, vol. 8, pp. 1486–1491, 2008.

[39] M. L. Juan, M. Righini, and R. Quidant, "Plasmon nano-optical tweezers," *Nat. Photonics*, vol. 5, pp. 349–356, 2011.

[40] J. W. Black, M. Kamenetska, and Z. Ganim, "An optical tweezers platform for single molecule force spectroscopy in organic solvents," *Nano Lett.*, vol. 17, p. 6598, 2017.

[41] J. R. Moffitt, Y. R. Chemla, S. B. Smith, and C. Bustamante, "Recent advances in optical tweezers," *Annu. Rev. Biochem.*, vol. 77, pp. 205–228, 2008.

[42] K. C. Neuman and A. Nagy, "Single-molecule force spectroscopy: optical tweezers, magnetic tweezers and atomic force microscopy," *Nat. Methods*, vol. 5, pp. 491–505, 2008.

[43] H. Kress, J.-G. Park, C. O. Mejean, J. D. Forster, J. Park, S. S. Walse, Y. Zhang, D. Wu, O. D. Weiner, T. M. Fahmy, *et al.*, "Cell stimulation with optically manipulated microsources," *Nat. Methods*, vol. 6, no. 12, p. 905, 2009.

[44] F. M. Fazal and S. M. Block, "Optical tweezers study life under tension," *Nat. Photonics*, vol. 5, pp. 318–321, 2011.

[45] M. Capitanio, M. Canepari, M. Maffei, D. Beneventi, C. Monico, F. Vanzi, R. Bottinelli, and F. S. Pavone, "Ultrafast force-clamp spectroscopy of single molecules reveals load dependence of myosin working stroke," *Nat. Methods*, vol. 9, no. 10, p. 1013, 2012.

[46] V. Shvedov, A. R. Davoyan, C. Hnatovsky, N. Engheta, and W. Krolikowski, "A long-range polarization-controlled optical tractor beam," *Nat. Photonics*, vol. 8, no. 11, pp. 846–850, 2014.

[47] Z. Zhang, D. Cannan, J. Liu, P. Zhang, D. N. Christodoulides, and Z. Chen, "Observation of trapping and transporting air-borne absorbing particles with a single optical beam," *Opt. Express*, vol. 20, no. 15, pp. 16212–16217, 2012.

[48] Y.-L. Pan, C. Wang, S. C. Hill, M. Coleman, L. A. Beresnev, and J. L. Santarpia, "Trapping of individual airborne absorbing particles using a counterflow nozzle and photophoretic trap for continuous sampling and analysis," *Appl. Phys. Lett.*, vol. 104, no. 11, p. 113507, 2014.

[49] C. Wang, Z. Gong, Y.-L. Pan, and G. Videen, "Laser pushing or pulling of absorbing airborne particles," *Appl. Phys. Lett.*, vol. 109, no. 1, p. 011905, 2016.

[50] Z. Gong, Y.-L. Pan, and C. Wang, "Optical configurations for photophoretic trap of single particles in air," *Rev. Sci. Instrum.*, vol. 87, no. 10, p. 103104, 2016.

[51] V. G. Shvedov, A. V. Rode, Y. V. Izdebskaya, A. S. Desyatnikov, W. Krolikowski, and Y. S. Kivshar, "Giant optical manipulation," *Phys. Rev. Lett.*, vol. 105, no. 11, p. 118103, 2010.

[52] V. G. Shvedov, A. S. Desyatnikov, A. V. Rode, W. Krolikowski, and Y. S. Kivshar, "Optical guiding of absorbing nanoclusters in air," *Opt. Express*, vol. 17, no. 7, pp. 5743–5757, 2009.

[53] J. Lin and Y.-q. Li, "Optical trapping and rotation of airborne absorbing particles with a single focused laser beam," *Appl. Phys. Lett.*, vol. 104, no. 10, p. 101909, 2014.

[54] B. Redding and Y.-L. Pan, "Optical trap for both transparent and absorbing particles in air using a single shaped laser beam," *Opt. Lett.*, vol. 40, no. 12, pp. 2798–2801, 2015.

[55] D. S. Ether Jr, L. B. Pires, S. Umrath, D. Martinez, Y. Ayala, B. Pontes, G. R. de S. Araújo, S. Frases, G.-L. Ingold, F. S. S. Rosa, N. B. Viana, and H. M. Nussenzveig, "Probing the casimir force with optical tweezers," *EPL*, vol. 112, no. 4, p. 44001, 2015.

[56] Z. Xu and T. Li, "Detecting casimir torque with an optically levitated nanorod," *Phys. Rev. A*, vol. 96, p. 033843, 2017.

[57] G. Pesce, G. Volpe, O. M. Maragó, P. H. Jones, S. Gigan, A. Sasso, and G. Volpe, "Step-by-step guide to the realization of advanced optical tweezers," *J. Opt. Soc. Am. B*, vol. 32, no. 5, pp. B84–B98, 2015.

[58] J. D. Jackson, *Classical electrodynamics*. John Wiley & Sons, 2007.

[59] D. J. Griffiths, "Introduction to electrodynamics," 2005.

[60] Y. Harada and T. Asakura, "Radiation forces on a dielectric sphere in the Rayleigh scattering regime," *Opt. Commun.*, vol. 124, no. 5-6, pp. 529–541, 1996.

[61] Z. Liu and D. Zhao, "Radiation forces acting on a Rayleigh dielectric sphere produced by highly focused elegant hermite-cosine-gaussian beams," *Opt. Express*, vol. 20, no. 3, pp. 2895–2904, 2012.

[62] R. S. Dutra, N. B. Viana, P. A. M. Neto, and H. M. Nussenzveig, "Exact theory of optical tweezers and its application to absolute calibration," in *Optical Tweezers*, pp. 25–39, Springer, 2017.

[63] R. S. Dutra, N. B. Viana, P. A. M. Neto, and H. M. Nussenzveig, "Polarization effects in optical tweezers," *J. Opt. A: Pure Appl. Opt.*, vol. 9, no. 8, pp. S221–S227, 2007.

[64] H. C. Bryant and A. J. Cox, "Mie theory and the glory," *J. Opt. Soc. Am.*, vol. 56, no. 11, pp. 1529–1532, 1966.

[65] R. T. Wang and H. C. Van de Hulst, "Rainbows: Mie computations and the airy approximation," *Appl. Opt.*, vol. 30, no. 1, pp. 106–117, 1991.

[66] K. Svoboda and S. M. Block, "Optical trapping of metallic Rayleigh particles," *Opt. Lett.*, vol. 19, no. 13, pp. 930–932, 1994.

[67] C. Min, Z. Shen, J. Shen, Y. Zhang, H. Fang, G. Yuan, L. Du, S. Zhu, T. Lei, and X. Yuan, "Focused plasmonic trapping of metallic particles.," *Nat. Comunn.*, vol. 4, p. Art. 2891, 2013.

[68] Q. Zhan, "Trapping metallic Rayleigh particles with radial polarization.," *Opt. Express*, vol. 12, pp. 3377–3382, 2004.

[69] L. Huang, H. Guo, J. Li, L. Ling, B. Feng, and Z. Li, "Optical trapping of gold nanoparticles by cylindrical vector beam.," *Opt. Lett.*, vol. 37, pp. 1694–1696, 2012.

[70] M. Lewittes, S. Arnold, and G. Oster, "Radiometric levitation of micron sized spheres," *Appl. Phys. Lett.*, vol. 40, no. 6, pp. 455–457, 1982.

[71] S. Sato, Y. Harada, and Y. Waseda, "Optical trapping of microscopic metal particles," *Opt. Lett.*, vol. 19, no. 22, pp. 1807–1809, 1994.

[72] P. C. Ke and M. Gu, "Characterization of trapping force on metallic Mie particles," *Appl. Opt.*, vol. 38, no. 1, pp. 160–167, 1999.

[73] A. B. Pluchino and S. Arnold, "Comprehensive model of the photophoretic force on a spherical microparticle," *Opt. Lett.*, vol. 10, no. 6, pp. 261–263, 1985.

[74] O. A. Schmidt, M. K. Garbos, T. G. Euser, and P. S. J. Russell, "Reconfigurable optothermal microparticle trap in air-filled hollow-core photonic crystal fiber," *Phys. Rev. Lett.*, vol. 109, no. 2, p. 024502, 2012.

[75] K. Dholakia and T. Čižmár, "Light and heat in a balancing act," *Physics*, vol. 5, p. 76, 2012.

[76] N. Viana, M. Rocha, and O. Mesquita, "In situ laser power measurement at the focus of microscope objectives used in optical tweezers," *Am. J. Phys.*, vol. 73, no. 3, pp. 201–205, 2005.

[77] T. Moura, U. Andrade, J. Mendes, and M. Rocha, "Silicon microparticles as handles for optical tweezers experiments," *Opt. Lett.*, vol. 45, no. 5, pp. 1055–1058, 2020.

[78] L. Jia and E. L. Thomas, "Radiation forces on dielectric and absorbing particles studied via the finite-difference time-domain method," *J. Opt. Soc. Am. B*, vol. 26, no. 10, pp. 1882–1891, 2009.

[79] G. G. Stokes *et al.*, *On the effect of the internal friction of fluids on the motion of pendulums*, vol. 9. Pitt Press Cambridge, 1851.

[80] Y. Deng, J. Bechhoefer, and N. R. Forde, "Brownian motion in a modulated optical trap," *J. Opt. A: Pure Appl. Opt.*, vol. 9, no. 8, p. S256, 2007.

[81] M. Grimm, T. Franosch, and S. Jeney, "High-resolution detection of brownian motion for quantitative optical tweezers experiments," *Phys. Rev. E*, vol. 86, no. 2, p. 021912, 2012.

[82] R. P. Brody, *On The Stochastic Behavior of Brownian Particles in Potential Wells, as Observed with Optical Traps*. Fogler Library, 2008.

[83] A. A. Bui, A. B. Stilgoe, I. C. Lenton, L. J. Gibson, A. V. Kashchuk, S. Zhang, H. Rubinsztein-Dunlop, and T. A. Nieminen, "Theory and practice of simulation of optical tweezers," *J. Quant. Spectrosc. Radiat. Transf.*, vol. 195, pp. 66–75, 2017.

[84] X.-L. Qi, T. L. Hughes, and S.-C. Zhang, "Topological field theory of time-reversal invariant insulators," *Phys. Rev. B*, vol. 78, no. 19, p. 195424, 2008.

[85] Y. Chen, J. G. Analytis, J.-H. Chu, Z. Liu, S.-K. Mo, X.-L. Qi, H. Zhang, D. Lu, X. Dai, Z. Fang, *et al.*, "Experimental realization of a three-dimensional topological insulator, Bi_2Te_3," *Science*, vol. 325, no. 5937, pp. 178–181, 2009.

[86] J. E. Moore, "The birth of topological insulators," *Nature*, vol. 464, no. 7286, pp. 194–198, 2010.

[87] Z.-H. Pan, E. Vescovo, A. Fedorov, D. Gardner, Y. Lee, S. Chu, G. Gu, and T. Valla, "Electronic structure of the topological insulator Bi_2Se_3 using angle-resolved photoemission spectroscopy: evidence for a nearly full surface spin polarization," *Phys. Rev. Lett.*, vol. 106, no. 25, p. 257004, 2011.

[88] G. A. Fiete, "How do you want that insulator?," *Science*, vol. 332, no. 6029, pp. 546–547, 2011.

[89] C.-K. Chiu, J. C. Teo, A. P. Schnyder, and S. Ryu, "Classification of topological quantum matter with symmetries," *Rev. Mod. Phys.*, vol. 88, no. 3, p. 035005, 2016.

[90] B. Bradlyn, L. Elcoro, J. Cano, M. Vergniory, Z. Wang, C. Felser, M. Aroyo, and B. A. Bernevig, "Topological quantum chemistry," *Nature*, vol. 547, no. 7663, pp. 298–305, 2017.

[91] J. Wang and S.-C. Zhang, "Topological states of condensed matter," *Nature materials*, vol. 16, no. 11, pp. 1062–1067, 2017.

[92] F. D. M. Haldane, "Nobel lecture: Topological quantum matter," *Rev. Mod. Phys.*, vol. 89, no. 4, p. 040502, 2017.

[93] P. Liu, J. R. Williams, and J. J. Cha, "Topological nanomaterials," *Nat. Rev. Mater.*, vol. 4, no. 7, pp. 479–496, 2019.

[94] F. Tang, H. C. Po, A. Vishwanath, and X. Wan, "Comprehensive search for topological materials using symmetry indicators," *Nature*, vol. 566, no. 7745, pp. 486–489, 2019.

[95] M. Vergniory, L. Elcoro, C. Felser, N. Regnault, B. A. Bernevig, and Z. Wang, "A complete catalogue of high-quality topological materials," *Nature*, vol. 566, no. 7745, pp. 480–485, 2019.

[96] V. L. Berezinskii, "Destruction of long-range order in one-dimensional and two-dimensional systems possessing a continuous symmetry group. ii. quantum systems," *Sov. Phys. JETP*, vol. 34, no. 3, pp. 610–616, 1972.

[97] J. M. Kosterlitz and D. J. Thouless, "Ordering, metastability and phase transitions in two-dimensional systems," *J. Phys. C: Solid State Physics*, vol. 6, no. 7, p. 1181, 1973.

[98] K. v. Klitzing, G. Dorda, and M. Pepper, "New method for high-accuracy determination of the fine-structure constant based on quantized Hall resistance," *Phys. Rev. Lett.*, vol. 45, pp. 494–497, 1980.

[99] D. J. Thouless, M. Kohmoto, M. P. Nightingale, and M. den Nijs, "Quantized Hall conductance in a two-dimensional periodic potential," *Phys. Rev. Lett.*, vol. 49, no. 6, p. 405, 1982.

[100] G. Agnolet, D. McQueeney, and J. Reppy, "Kosterlitz-Thouless transition in helium films," *Phys. Rev. B*, vol. 39, no. 13, p. 8934, 1989.

[101] D. J. Bishop and J. D. Reppy, "Study of the superfluid transition in two-dimensional He 4 films," *Phys. Rev. Lett.*, vol. 40, no. 26, p. 1727, 1978.

[102] Y. Ando and L. Fu, "Topological crystalline insulators and topological superconductors: From concepts to materials," *Annu. Rev. Condens. Matter Phys.*, vol. 6, no. 1, pp. 361–381, 2015.

[103] S. Hyde, Z. Blum, T. Landh, S. Lidin, B. W. Ninham, S. Andersson, and K. Larsson, *The language of shape: the role of curvature in condensed matter: physics, chemistry and biology*. Elsevier, 1996.

[104] E. H. Hall *et al.*, "On a new action of the magnet on electric currents," *Am. J. Math.*, vol. 2, no. 3, pp. 287–292, 1879.

[105] C.-X. Liu, S.-C. Zhang, and X.-L. Qi, "The quantum anomalous Hall effect: Theory and experiment," *Annu. Rev. Condens. Mat. Phys.*, vol. 7, pp. 301–321, 2016.

[106] X.-L. Qi and S.-C. Zhang, "Topological insulators and superconductors," *Rev. Mod. Phys.*, vol. 83, pp. 1057–1110, 2011.

[107] M. Z. Hasan and C. L. Kane, "Colloquium: Topological insulators," *Rev. Mod. Phys.*, vol. 82, pp. 3045–3067, 2010.

[108] C. Kane and J. Moore, "Topological insulators," *Phys. World*, vol. 24, no. 02, pp. 32–36, 2011.

[109] D. Xiao, M.-C. Chang, and Q. Niu, "Berry phase effects on electronic properties," *Rev. Mod. Phys.*, vol. 82, no. 3, p. 1959, 2010.

[110] C. L. Kane and E. J. Mele, "Quantum spin Hall effect in graphene," *Phys. Rev. Lett.*, vol. 95, no. 22, p. 226801, 2005.

[111] B. A. Bernevig and S.-C. Zhang, "Quantum spin hall effect," *Phys. Rev. Lett.*, vol. 96, no. 10, p. 106802, 2006.

[112] Y. Yao, F. Ye, X.-L. Qi, S.-C. Zhang, and Z. Fang, "Spin-orbit gap of graphene: First-principles calculations," *Phys. Rev. B*, vol. 75, no. 4, p. 041401, 2007.

[113] H. Min, J. Hill, N. A. Sinitsyn, B. Sahu, L. Kleinman, and A. H. MacDonald, "Intrinsic and Rashba spin-orbit interactions in graphene sheets," *Phys. Rev. B*, vol. 74, no. 16, p. 165310, 2006.

[114] B. A. Bernevig, T. L. Hughes, and S.-C. Zhang, "Quantum spin Hall effect and topological phase transition in HgTe quantum wells," *Science*, vol. 314, no. 5806, pp. 1757–1761, 2006.

[115] M. König, S. Wiedmann, C. Brüne, A. Roth, H. Buhmann, L. W. Molenkamp, X.-L. Qi, and S.-C. Zhang, "Quantum spin Hall insulator state in HgTe quantum wells," *Science*, vol. 318, no. 5851, pp. 766–770, 2007.

[116] D. R. Candido, *Blurring the boundaries between topological and non-topological physical phenomena in dots*. PhD thesis, Universidade de São Paulo, 2018.

[117] S.-Q. SHEN, *Topological Insulators: Dirac Equation in Condensed Matters*. Springer, 2018.

[118] E. Fradkin, *Field theories of condensed matter physics*. Cambridge University Press, 2013.

[119] L. Fu and C. L. Kane, "Time reversal polarization and a $\mathbb{Z}_2$ adiabatic spin pump," *Phys. Rev. B*, vol. 74, no. 19, p. 195312, 2006.

[120] L. Fu, C. L. Kane, and E. J. Mele, "Topological insulators in three dimensions," *Phys. Rev. Lett.*, vol. 98, no. 10, p. 106803, 2007.

[121] J. E. Moore and L. Balents, "Topological invariants of time-reversal-invariant band structures," *Phys. Rev. B*, vol. 75, no. 12, p. 121306, 2007.

[122] R. Roy, "Topological phases and the quantum spin Hall effect in three dimensions," *Phys. Rev. B*, vol. 79, no. 19, p. 195322, 2009.

[123] X.-L. Qi, R. Li, J. Zang, and S.-C. Zhang, "Inducing a magnetic monopole with topological surface states," *Science*, vol. 323, no. 5918, pp. 1184–1187, 2009.

[124] D. Hsieh, D. Qian, L. Wray, Y. Xia, Y. S. Hor, R. J. Cava, and M. Z. Hasan, "A topological Dirac insulator in a quantum spin Hall phase," *Nature*, vol. 452, no. 7190, p. 970, 2008.

[125] X. Qi and S. Zhang, "The quantum spin Hall effect and topological insulators," *Phys. Today*, vol. 63, p. 33, 2010.

[126] Y. Ando, "Topological insulator materials," *J. Phys. Soc. Japan*, vol. 82, p. 102001, 2013.

[127] P. Roushan, J. Seo, C. V. Parker, Y. S. Hor, D. Hsieh, D. Qian, A. Richardella, M. Z. Hasan, R. J. Cava, and A. Yazdani, "Topological surface states protected from backscattering by chiral spin texture," *Nature*, vol. 460, no. 7259, pp. 1106–1109, 2009.

[128] V. Iyer, Y. P. Chen, and X. Xu, "Ultrafast surface state spin-carrier dynamics in the topological insulator bi 2 te 2 se," *Phys. Rev. Lett.*, vol. 121, no. 2, p. 026807, 2018.

[129] C.-X. Liu, X.-L. Qi, H. Zhang, X. Dai, Z. Fang, and S.-C. Zhang, "Model Hamiltonian for topological insulators," *Phys. Rev. B*, vol. 82, no. 4, p. 045122, 2010.

[130] L. Fu and C. L. Kane, "Topological insulators with inversion symmetry," *Phys. Rev. B*, vol. 76, no. 4, p. 045302, 2007.

[131] H. Zhang, C.-X. Liu, X.-L. Qi, X. Dai, Z. Fang, and S.-C. Zhang, "Topological insulators in Bi_2Se_3, Bi_2Te_3 and Sb_2Te_3 with a single Dirac cone on the surface," *Nat. Phys*, vol. 5, no. 6, pp. 438–442, 2009.

[132] Y. Xia, D. Qian, D. Hsieh, L. Wray, A. Pal, H. Lin, A. Bansil, D. Grauer, Y. S. Hor, R. J. Cava, *et al.*, "Observation of a large-gap topological-insulator class with a single Dirac cone on the surface," *Nat. Phys*, vol. 5, no. 6, pp. 398–402, 2009.

[133] D. Hsieh, Y. Xia, L. Wray, D. Qian, A. Pal, J. Dil, J. Osterwalder, F. Meier, G. Bihlmayer, C. Kane, *et al.*, "Observation of unconventional quantum spin textures in topological insulators," *Science*, vol. 323, no. 5916, pp. 919–922, 2009.

[134] Y. Chen, J.-H. Chu, J. Analytis, Z. Liu, K. Igarashi, H.-H. Kuo, X. Qi, S.-K. Mo, R. Moore, D. Lu, *et al.*, "Massive Dirac fermion on the surface of a magnetically doped topological insulator," *Science*, vol. 329, no. 5992, pp. 659–662, 2010.

[135] W.-Y. Shan, H.-Z. Lu, and S.-Q. Shen, "Effective continuous model for surface states and thin films of three-dimensional topological insulators," *New J. Phys.*, vol. 12, no. 4, p. 043048, 2010.

[136] K. Nomura, M. Koshino, and S. Ryu, "Topological delocalization of two-dimensional massless Dirac fermions," *Phys. Rev. Lett.*, vol. 99, no. 14, p. 146806, 2007.

[137] J. M. Fonseca, W. A. Moura-Melo, and A. R. Pereira, "Geometrically induced electric polarization in conical topological insulators," *J. Appl. Phys.*, vol. 111, no. 6, p. 064913, 2012.

[138] Y. G. Muller, W. A. Moura-Melo, and J. M. Fonseca, "Shedding light onto topological insulator beads: perspectives for optical tweezing application.," *arXiv:1609.00308v1*, 2016.

[139] K. Everschor-Sitte, M. Sitte, and A. H. MacDonald, "Interaction correction to the magnetoelectric polarizability of $\mathbb{Z}_2$ topological insulators," *Phys. Rev. B*, vol. 92, no. 24, p. 245118, 2015.

[140] X.-L. Qi, T. L. Hughes, S. Raghu, and S.-C. Zhang, "Time-reversal-invariant topological superconductors and superfluids in two and three dimensions," *Phys. Rev. Lett.*, vol. 102, p. 187001, 2009.

[141] M. Wimmer, A. R. Akhmerov, M. V. Medvedyeva, J. Tworzydło, and C. W. J. Beenakker, "Majorana bound states without vortices in topological superconductors with electrostatic defects," *Phys. Rev. Lett.*, vol. 105, p. 046803, 2010.

[142] H. Ren, F. Pientka, S. Hart, A. T. Pierce, M. Kosowsky, L. Lunczer, R. Schlereth, B. Scharf, E. M. Hankiewicz, L. W. Molenkamp, *et al.*, "Topological superconductivity in a phase-controlled josephson junction," *Nature*, vol. 569, no. 7754, pp. 93–98, 2019.

[143] N. P. Armitage, E. J. Mele, and A. Vishwanath, "Weyl and Dirac semimetals in three-dimensional solids," *Rev. Mod. Phys.*, vol. 90, p. 015001, 2018.

[144] A. B. Khanikaev, S. Hossein Mousavi, W. K. Tse, M. Kargarian, A. H. MacDonald, and G. Shvets, "Photonic topological insulators," *Nat. Mater.*, vol. 12, no. 3, pp. 233–239, 2013.

[145] Y. Yang, Z. Gao, H. Xue, L. Zhang, M. He, Z. Yang, R. Singh, Y. Chong, B. Zhang, and H. Chen, "Realization of a three-dimensional photonic topological insulator," *Nature*, vol. 565, no. 7741, pp. 622–626, 2019.

[146] E. Lustig, S. Weimann, Y. Plotnik, Y. Lumer, M. A. Bandres, A. Szameit, and M. Segev, "Photonic topological insulator in synthetic dimensions," *Nature*, vol. 567, no. 7748, pp. 356–360, 2019.

[147] C. He, X. Ni, H. Ge, X.-C. Sun, Y.-B. Chen, M.-H. Lu, X.-P. Liu, and Y.-F. Chen, "Acoustic topological insulator and robust one-way sound transport," *Nat. Phys*, vol. 12, no. 12, pp. 1124–1129, 2016.

[148] X. Zhang, M. Xiao, Y. Cheng, M.-H. Lu, and J. Christensen, "Topological sound," *Commun. Phys.*, vol. 1, no. 1, pp. 1–13, 2018.

[149] J. Sinova and T. Jungwirth, "Surprises from the spin Hall effect," *Phys. Today*, vol. 70, no. 7, pp. 38–42, 2017.

[150] J. Sinova and I. Žutić, "New moves of the spintronics tango," *Nat. Mater.*, vol. 11, no. 5, pp. 368–371, 2012.

[151] T. Neupert and F. Schindler, "Topological crystalline insulators," in *Topological Matter*, vol. 190, pp. 31–61, Springer, 2018.

[152] M. Pletyukhov, D. M. Kennes, K. Piasotski, J. Klinovaja, D. Loss, and H. Schoeller, "Rational boundary charge in one-dimensional systems with interaction and disorder," *Phys. Rev. Research*, vol. 2, p. 033345, 2020.

[153] L. Fu, "Topological crystalline insulators," *Phys. Rev. Lett.*, vol. 106, no. 10, p. 106802, 2011.

[154] Y. Ando and L. Fu, "Topological crystalline insulators and topological superconductors: From concepts to materials," *Annu. Rev. Condens. Matter Phys.*, vol. 6, no. 1, pp. 361–381, 2015.

[155] T. H. Hsieh, H. Lin, J. Liu, W. Duan, A. Bansil, and L. Fu, "Topological crystalline insulators in the snte material class," *Nat. Commun.*, vol. 3, no. 1, pp. 1–7, 2012.

[156] Y. Tanaka, Z. Ren, T. Sato, K. Nakayama, S. Souma, T. Takahashi, K. Segawa, and Y. Ando, "Experimental realization of a topological crystalline insulator in SnTe," *Nat. Phys*, vol. 8, no. 11, pp. 800–803, 2012.

[157] P. Dziawa, B. Kowalski, K. Dybko, R. Buczko, A. Szczerbakow, M. Szot, E. Łusakowska, T. Balasubramanian, B. M. Wojek, M. Berntsen, *et al.*, "Topological crystalline insulator states in $Pb_{1-x}Sn_xSe$," *Nature materials*, vol. 11, no. 12, pp. 1023–1027, 2012.

[158] S.-Y. Xu, M. Neupane, C. Liu, D. Zhang, A. Richardella, L. Andrew Wray, N. Alidoust, M. Leandersson, T. Balasubramanian, J. Sánchez-Barriga, O. Rader, G. Landolt, B. Slomski, J. Hugo Dil, J. Osterwalder, T.-R. Chang, H.-T. Jeng, H. Lin, A. Bansil, N. Samarth, and M. Zahid Hasan, "Hedgehog spin texture and Berry's phase tuning in a magnetic topological insulator," *Nat. Phys.*, vol. 8, no. 8, pp. 616–622, 2012.

[159] W. A. Benalcazar, B. A. Bernevig, and T. L. Hughes, "Quantized electric multipole insulators," *Science*, vol. 357, no. 6346, pp. 61–66, 2017.

[160] F. Schindler, A. M. Cook, M. G. Vergniory, Z. Wang, S. S. Parkin, B. A. Bernevig, and T. Neupert, "Higher-order topological insulators," *Sci. Adv.*, vol. 4, no. 6, p. eaat0346, 2018.

[161] F. Schindler, M. Brzezińska, W. A. Benalcazar, M. Iraola, A. Bouhon, S. S. Tsirkin, M. G. Vergniory, and T. Neupert, "Fractional corner charges in spin-orbit coupled crystals," *Phys. Rev. Research*, vol. 1, p. 033074, 2019.

[162] Y. Otaki and T. Fukui, "Higher-order topological insulators in a magnetic field," *Phys. Rev. B*, vol. 100, no. 24, p. 245108, 2019.

[163] I. Petrides and O. Zilberberg, "Higher-order topological insulators, topological pumps and the quantum Hall effect in high dimensions," *Phys. Rev. Research*, vol. 2, no. 2, p. 022049, 2020.

[164] M. Ezawa, "Minimal models for wannier-type higher-order topological insulators and phosphorene," *Phys. Rev. B*, vol. 98, p. 045125, 2018.

[165] Z. Wang, Q. Wei, H.-Y. Xu, and D.-J. Wu, "A higher-order topological insulator with wide bandgaps in lamb-wave systems," *J. Appl. Phys.*, vol. 127, no. 7, p. 075105, 2020.

[166] A. Dutt, M. Minkov, and S. Fan, "Higher-order topological insulators in synthetic dimensions," *arXiv preprint arXiv:1911.11310*, 2019.

[167] R. Chen, C.-Z. Chen, J.-H. Gao, B. Zhou, and D.-H. Xu, "Higher-order topological insulators in quasicrystals," *Phys. Rev. Lett.*, vol. 124, no. 3, p. 036803, 2020.

[168] J. Langbehn, Y. Peng, L. Trifunovic, F. von Oppen, and P. W. Brouwer, "Reflection-symmetric second-order topological insulators and superconductors," *Phys. Rev. Lett.*, vol. 119, p. 246401, 2017.

[169] E. Khalaf, H. C. Po, A. Vishwanath, and H. Watanabe, "Symmetry Indicators and Anomalous Surface States of Topological Crystalline Insulators," *Phys. Rev. X*, vol. 8, no. 3, p. 31070, 2018.

[170] M. Ezawa, "Magnetic second-order topological insulators and semimetals," *Phys. Rev. B*, vol. 97, no. 15, p. 155305, 2018.

[171] M. Ezawa, "Topological switch between second-order topological insulators and topological crystalline insulators," *Phys. Rev. Lett.*, vol. 121, p. 116801, 2018.

[172] C. Yue, Y. Xu, Z. Song, H. Weng, Y.-M. Lu, C. Fang, and X. Dai, "Symmetry-enforced chiral hinge states and surface quantum anomalous Hall effect in the magnetic axion insulator $Bi_{2-x}Sm_xSe_3$," *Nat. Phys.*, p. 1, 2019.

[173] M. J. Park, Y. Kim, G. Y. Cho, and S. Lee, "Higher-order topological insulator in twisted bilayer graphene," *Phys. Rev. Lett.*, vol. 123, p. 216803, 2019.

[174] F. Schindler, Z. Wang, M. G. Vergniory, A. M. Cook, A. Murani, S. Sengupta, A. Y. Kasumov, R. Deblock, S. Jeon, I. Drozdov, *et al.*, "Higher-order topology in bismuth," *Nat. Phys*, vol. 14, no. 9, pp. 918–924, 2018.

[175] M. Serra-Garcia, V. Peri, R. Süsstrunk, O. R. Bilal, T. Larsen, L. G. Villanueva, and S. D. Huber, "Observation of a phononic quadrupole topological insulator," *Nature*, vol. 555, no. 7696, pp. 342–345, 2018.

[176] S. Imhof, C. Berger, F. Bayer, J. Brehm, L. W. Molenkamp, T. Kiessling, F. Schindler, C. H. Lee, M. Greiter, T. Neupert, *et al.*, "Topolectrical-circuit realization of topological corner modes," *Nat. Phys*, vol. 14, no. 9, pp. 925–929, 2018.

[177] C. W. Peterson, W. A. Benalcazar, T. L. Hughes, and G. Bahl, "A quantized microwave quadrupole insulator with topologically protected corner states," *Nature*, vol. 555, no. 7696, pp. 346–350, 2018.

[178] I. Žutić, J. Fabian, and S. Das Sarma, "Spintronics: Fundamentals and applications," *Rev. Mod. Phys.*, vol. 76, no. 2, pp. 323–410, 2004.

[179] A. Brataas, A. D. Kent, and H. Ohno, "Current-induced torques in magnetic materials," *Nat. Mater.*, vol. 11, no. 5, pp. 372–381, 2012.

[180] D. Pesin and A. H. MacDonald, "Spintronics and pseudospintronics in graphene and topological insulators," *Nat. Mater.*, vol. 11, no. 5, pp. 409–416, 2012.

[181] O. Gomonay, V. Baltz, A. Brataas, and Y. Tserkovnyak, "Antiferromagnetic spin textures and dynamics," *Nat. Phys.*, vol. 14, no. 3, pp. 213–216, 2018.

[182] T. Jungwirth, J. Sinova, A. Manchon, X. Marti, J. Wunderlich, and C. Felser, "The multiple directions of antiferromagnetic spintronics," *Nat. Phys.*, vol. 14, no. 3, pp. 200–203, 2018.

[183] S. Bhatti, R. Sbiaa, A. Hirohata, H. Ohno, S. Fukami, and S. N. Piramanayagam, "Spintronics based random access memory: a review," *Mater. Today*, vol. 20, no. 9, pp. 530–548, 2017.

[184] T. Endoh and H. Honjo, "A recent progress of spintronics devices for integrated circuit applications," *J. Low Power Electron. Appl.*, vol. 8, no. 4, pp. 1–17, 2018.

[185] H. Dery, P. Dalal, Cywiński, and L. J. Sham, "Spin-based logic in semiconductors for reconfigurable large-scale circuits," *Nature*, vol. 447, no. 7144, pp. 573–576, 2007.

[186] W. J. Xu, B. Zhang, Z. Wang, S. S. Chu, W. Li, Z. B. Wu, R. H. Yu, and X. X. Zhang, "Scaling law of anomalous Hall effect in Fe/Cu bilayers," *Eur. Phys. J. B*, vol. 65, no. 2, pp. 233–237, 2008.

[187] A. Khitun, M. Bao, Y. Wu, J.-Y. Kim, A. Hong, A. Jacob, K. Galatsis, and K. L. Wang, "Spin wave logic circuit on silicon platform," in *Fifth International Conference on Information Technology: New Generations (itng 2008)*, pp. 1107–1110, IEEE, 2008.

[188] B. Behin-Aein, D. Datta, S. Salahuddin, and S. Datta, "Proposal for an all-spin logic device with built-in memory," *Nat. Nanotechnol.*, vol. 5, no. 4, pp. 266–270, 2010.

[189] P. Wadley, B. Howells, J. Železný, C. Andrews, V. Hills, R. P. Campion, V. Novák, K. Olejník, F. Maccherozzi, S. S. Dhesi, S. Y. Martin, T. Wagner, J. Wunderlich, F. Freimuth, Y. Mokrousov, J. Kuneš, J. S. Chauhan, M. J. Grzybowski, A. W. Rushforth, K. Edmond, B. L. Gallagher, and T. Jungwirth, "Spintronics: Electrical switching of an antiferromagnet," *Science*, vol. 351, no. 6273, pp. 587–590, 2016.

[190] W. Han, R. K. Kawakami, M. Gmitra, and J. Fabian, "Graphene spintronics," *Nat. Nanotechnol.*, vol. 9, no. 10, pp. 794–807, 2014.

[191] P. Wadley, V. Novák, R. Campion, C. Rinaldi, X. Martí, H. Reichlová, J. Železný, J. Gazquez, M. Roldan, M. Varela, D. Khalyavin, S. Langridge, D. Kriegner, F. Máca, J. Mašek, R. Bertacco, V. Holý, A. Rushforth, K. Edmonds, B. Gallagher, C. Foxon, J. Wunderlich, and T. Jungwirth, "Tetragonal phase of epitaxial room-temperature antiferromagnet CuMnAs," *Nat. Commun.*, vol. 4, no. 1, p. 2322, 2013.

[192] V. Hills, P. Wadley, R. P. Campion, V. Novak, R. Beardsley, K. W. Edmonds, B. L. Gallagher, B. Ouladdiaf, and T. Jungwirth, "Paramagnetic to antiferromagnetic transition in epitaxial tetragonal CuMnAs (invited)," *J. Appl. Phys.*, vol. 117, no. 17, pp. 2014–2016, 2015.

[193] P. Němec, M. Fiebig, T. Kampfrath, and A. V. Kimel, "Antiferromagnetic opto-spintronics," *Nat. Phys.*, vol. 14, no. 3, pp. 229–241, 2018.

[194] A. V. Kimel, A. Kirilyuk, A. Tsvetkov, R. V. Pisarev, and T. Rasing, "Laser-induced ultrafast spin reorientation in the antiferromagnet TmFeO3," *Nature*, vol. 429, no. 6994, pp. 850–853, 2004.

[195] R. Cheng, J. Xiao, Q. Niu, and A. Brataas, "Spin Pumping and Spin-Transfer Torques in Antiferromagnets," *Phys. Rev. Lett.*, vol. 113, no. 5, p. 057601, 2014.

[196] L. Šmejkal, J. Železný, J. Sinova, and T. Jungwirth, "Electric Control of Dirac Quasiparticles by Spin-Orbit Torque in an Antiferromagnet," *Phys. Rev. Lett.*, vol. 118, no. 10, p. 106402, 2017.

[197] L. Šmejkal, Y. Mokrousov, B. Yan, and A. H. MacDonald, "Topological antiferromagnetic spintronics," *Nat. Phys.*, vol. 14, no. 3, pp. 242–251, 2018.

[198] ImageJ - Image Processing and Analysis in Java - https://imagej.nih.gov/ij/.

[199] J. Fleurial, L. Gailliard, R. Triboulet, H. Scherrer, and S. Scherrer, "Thermal properties of high quality single crystals of bismuth telluride—part i: Experimental characterization," *J. Phys. Chem. Solids*, vol. 49, no. 10, pp. 1237–1247, 1988.

[200] M. Michiardi, I. Aguilera, M. Bianchi, V. E. de Carvalho, L. O. Ladeira, N. G. Teixeira, E. A. Soares, C. Friedrich, S. Blügel, and P. Hofmann, "Bulk band structure of Bi_2Te_3," *Phys. Rev. B*, vol. 90, no. 7, p. 075105, 2014.

[201] V. B. Nascimento, V. E. De Carvalho, R. Paniago, E. A. Soares, L. O. Ladeira, and H. D. Pfannes, "XPS and EELS study of the bismuth selenide," *J. Electron Spectros. Relat. Phenomena*, vol. 104, no. 1-3, pp. 99–107, 1999.

[202] www.issp.ac.ru/lpcbc/DANDP/Bi-Ch.

[203] Y. C. Kiang and R. W. Lang, "Measuring focused gaussian beam spot sizes: a practical method.," *Appl. Opt.*, vol. 22, no. 9, pp. 1296–1297, 1983.

[204] M. Fox, "Optical properties of solids," 2001.

[205] Z. Yue, B. Cai, L. Wang, X. Wang, and M. Gu, "Intrinsically core-shell plasmonic dielectric nanostructures with ultrahigh refractive index," *Sci. Adv.*, vol. 2, p. e1501536, 2016.

[206] S. Parkin, G. Knöner, T. A. Nieminen, N. R. Heckenberg, and H. Rubinsztein-Dunlop, "Measurement of the total optical angular momentum transfer in optical tweezers," *Opt. Express*, vol. 14, no. 15, pp. 6963–6970, 2006.

[207] M. E. J. Friese, J. Enger, H. Rubinsztein-Dunlop, and N. R. Heckenberg, "Optical angular-momentum transfer to trapped absorbing particles," *Phys. Rev. A*, vol. 54, no. 2, p. 1593, 1996.

[208] H. He, M. E. J. Friese, N. R. Heckenberg, and H. Rubinsztein-Dunlop, "Direct observation of transfer of angular momentum to absorptive particles from a laser beam with a phase singularity," *Phys. Rev. Lett.*, vol. 75, no. 5, p. 826, 1995.

[209] V. Garcés-Chávez, K. Volke-Sepulveda, S. Chávez-Cerda, W. Sibbett, and K. Dholakia, "Transfer of orbital angular momentum to an optically trapped low-index particle," *Phys. Rev. A*, vol. 66, p. 063402, 2002.

[210] R. Pillarisetty, "Academic and industry research progress in germanium nanodevices," *Nature*, vol. 479, no. 7373, pp. 324,328, 2011.

[211] F. Pezzoli, F. Bottegoni, D. Trivedi, F. Ciccacci, A. Giorgioni, P. Li, S. Cecchi, E. Grilli, Y. Song, M. Guzzi, H. Dery, and G. Isella, "Optical spin injection and spin lifetime in Ge heterostructures," *Phys. Rev. Lett.*, vol. 108, p. 156603, 2012.

[212] S. Dushenko, M. Koike, Y. Ando, T. Shinjo, M. Myronov, and M. Shiraishi, "Experimental demonstration of room-temperature spin transport in n-type germanium epilayers," *Phys. Rev. Lett.*, vol. 114, p. 196602, 2015.

[213] F. Bottegoni, C. Zucchetti, S. D. Conte, J. Frigerio, E. Carpene, C. Vergnaud, M. Jamet, G. Isella, F. Ciccacci, G. Cerullo, and M. Finazzi, "Spin-Hall voltage over a large length scale in bulk germanium," *Phys. Rev. Lett.*, vol. 118, p. 167402, 2017.

[214] S. M. Sze and K. K. Ng, *Physics of semiconductor devices*. Wiley-Interscience, 2nd ed., 1981.

[215] R. Pillarisetty, "Academic and industry research progress in germanium nanodevices," *Nature*, vol. 479, no. 7373, pp. 324–328, 2011.

[216] S. C. Burdette and B. F. Thornton, "The germination of germanium," *Nat. Chem.*, vol. 10, no. 2, p. 244, 2018.

[217] "Filmetrics refractive index database." `https://www.filmetrics.com/refractive-index-database/Ge/Germanium`. Accessed: 2018-07-23.

[218] A. Lehmuskero, P. Johansson, H. Rubinsztein-Dunlop, L. Tong, and M. Kall, "Laser trapping of colloidal metal nanoparticles," *ACS Nano*, vol. 9, no. 4, pp. 3453–3469, 2015.

[219] L. A. C. A. Defaveri, W. A. M. Morgado, and S. M. D. Queirós, "Power output for a nonlinear brownian machine," *Phys. Rev. E*, vol. 96, p. 052115, 2017.

[220] L. A. C. A. Defaveri, S. M. D. Queirós, and W. A. M. Morgado, "Dependece of efficiency on the nonlinear nature of a nanomachine," *Phys. Rev. E*, vol. 98, p. 062106, 2018.

[221] I. A. Martinez, É. Roldán, L. Dinis, and R. A. Rica, "Colloidal heat engines: a review," *Soft matter*, vol. 13, no. 1, pp. 22–36, 2017.

[222] I. A. Martínez, E. Roldán, L. Dinis, D. Petrov, J. M. R. Parrondo, and R. A. Rica, "Brownian carnot engine," *Nat. Phys.*, vol. 12, pp. 67–70, 2016.

[223] P. A. Quinto-Su, "A microscopic steam engine implemented in an optical tweezer," *Nat. Commun.*, vol. 5, p. 5889, 2014.

[224] V. Blickle and C. Bechinger, "Realization of a micrometre-sized stochastic heat engine," *Nat. Phys*, vol. 8, no. 2, p. 143, 2012.

[225] J. R. Arias-González and M. Nieto-Vesperinas, "Optical forces on small particles: attractive and repulsive nature and plasmon-resonance conditions," *J. Opt. Soc. Am. A*, vol. 20, no. 7, pp. 1201–1209, 2003.

[226] F. Zhang, C. L. Kane, and E. J. Mele, "Surface states of topological insulators," *Phys. Rev. B*, vol. 86, no. 8, p. 081303, 2012.

[227] A. M. Essin, J. E. Moore, and D. Vanderbilt, "Magnetoelectric polarizability and axion electrodynamics in crystalline insulators," *Phys. Rev. Lett.*, vol. 102, no. 14, p. 146805, 2009.

[228] P. A. M. Dirac, "Quantised singularities in the electromagnetic field," *Proc. Royal Soc. Lond. Series A, Cont. Papers Math. Phys. Char.*, vol. 133, no. 821, pp. 60–72, 1931.

[229] C. Castelnovo, R. Moessner, and S. L. Sondhi, "Magnetic monopoles in spin ice," *Nature*, vol. 451, no. 7174, pp. 42–45, 2008.

[230] L. Mól, R. Silva, R. Silva, A. Pereira, W. Moura-Melo, and B. Costa, "Magnetic monopole and string excitations in two-dimensional spin ice," *J. Appl. Phys.*, vol. 106, no. 6, p. 063913, 2009.

[231] L. Mól, W. Moura-Melo, and A. Pereira, "Conditions for free magnetic monopoles in nanoscale square arrays of dipolar spin ice," *Phys. Rev. B*, vol. 82, no. 5, p. 054434, 2010.

[232] A. Béché, R. Van Boxem, G. Van Tendeloo, and J. Verbeeck, "Magnetic monopole field exposed by electrons," *Nat. Phys*, vol. 10, no. 1, pp. 26–29, 2014.

[233] E. König, P. Ostrovsky, I. Protopopov, I. Gornyi, I. Burmistrov, and A. Mirlin, "Half-integer quantum Hall effect of disordered Dirac fermions at a topological insulator surface," *Phys. Rev. B*, vol. 90, no. 16, p. 165435, 2014.

[234] J. Zhang, C.-Z. Chang, P. Tang, Z. Zhang, X. Feng, K. Li, L.-l. Wang, X. Chen, C. Liu, W. Duan, *et al.*, "Topology-driven magnetic quantum phase transition in topological insulators," *Science*, vol. 339, no. 6127, pp. 1582–1586, 2013.

[235] I. S. Gradshteyn and I. M. Ryzhik, *Table of integrals, series, and products*. Elsevier, 2007.

[236] S. Coh and D. Vanderbilt, PythTB - Python Tight Binding (2013) - http://www.physics.rutgers.edu/pythtb/about.html.

[237] M. Taherinejad, K. F. Garrity, and D. Vanderbilt, "Wannier center sheets in topological insulators," *Phys. Rev. B*, vol. 89, no. 11, p. 115102, 2014.

[238] L.-D. Yuan, Z. Wang, J.-W. Luo, E. I. Rashba, and A. Zunger, "Giant momentum-dependent spin splitting in centrosymmetric low-z antiferromagnets," *Phys. Rev. B*, vol. 102, no. 1, p. 014422, 2020.

[239] F. Schindler, A. M. Cook, M. G. Vergniory, Z. Wang, S. S. Parkin, B. A. Bernevig, and T. Neupert, "Higher-order topological insulators," *Sci. Adv.*, vol. 4, no. 6, p. eaat0346, 2018.

[240] W. Su, J. Schrieffer, and A. J. Heeger, "Solitons in polyacetylene," *Phys. Rev. Lett.*, vol. 42, no. 25, p. 1698, 1979.

[241] J. Zak, "Berry's phase for energy bands in solids," *Phys. Rev. Lett.*, vol. 62, no. 23, p. 2747, 1989.

[242] N. Goldman, J. C. Budich, and P. Zoller, "Topological quantum matter with ultracold gases in optical lattices," *Nat. Phys.*, vol. 12, no. 7, pp. 639–645, 2016.

[243] M. Aidelsburger, M. Atala, M. Lohse, J. T. Barreiro, B. Paredes, and I. Bloch, "Realization of the hofstadter hamiltonian with ultracold atoms in optical lattices," *Phys. Rev. Lett.*, vol. 111, no. 18, p. 185301, 2013.

[244] L.-M. Duan, E. Demler, and M. D. Lukin, "Controlling spin exchange interactions of ultracold atoms in optical lattices," *Phys. Rev. Lett.*, vol. 91, no. 9, p. 090402, 2003.

[245] P. Tang, Q. Zhou, G. Xu, and S.-C. Zhang, "Dirac fermions in an antiferromagnetic semimetal," *Nat. Phys.*, vol. 12, no. 12, pp. 1100–1104, 2016.